Silica Nanoparticles as Adjuvants for Novel Vaccines: A Combined Immunological, Simulation and Physical Characterisation Study

David James Connell

PhD Thesis, 2016

University of Strathclyde

Department of Chemical and Process Engineering

Declaration of Authenticity and Author's Rights

This thesis is the result of the author's original research. It has been composed by the author and has not been previously submitted for examination which has led to the award of a degree.

Signed:

Date:

Acknowledgements

I would like to thank my academic supervisors Dr Paul Mulheran and Dr Valerie Ferro. Their advice, guidance and wealth of knowledge was invaluable throughout my PhD. I would have been unable to complete my studies were it not for their helpful supervision and encouragement. I would also like to thank Dr Barbara Jachimska who made my stay in Poland not only worthwhile, but extremely enjoyable through her hospitality. This project would not have been completed were it not for the efforts of Dr Ayman Gebril. He guided me faultlessly through all immunological work and answered any questions I had, no matter how stupid they were, and I would like to thank him for that.

Thank you to the technical and administration staff throughout the chemical engineering department and SIPBS who helped make life easier throughout my PhD. Their approachability and helpfulness allowed me to confidently carry out my studies. I would also like to thank ARCHIE-WeSt High Performace Computer for facilitating all computational work that I carried out.

I would like to thank all of the friends I have made throughout my PhD. In particular Paul, Craig, Chris, Rab, Andrew, Joe, Fraser, Alessia, Hrvojka, Maryam, Stewart, Colin, Ese, Mark, Evan, Dorin, Martin and Vitor. They (and the rest of the department) have made my PhD fun and an enjoyable place to come to work every day. I would especially like to thank Javier and Scott, their friendship has helped me greatly through these past years. I would also like to thank my friends outside of university who have had to listen to me talk about my PhD for 4 years, particularly Grant, Ben, Mick, Lewis, Ally and Marc. I would also like to thank my family, particularly my Mum whose support and encouragement throughout my life has shaped the person I am today and I would not be in the position I am without her.

Finally I would like to thank Alyson, her love and support has helped me immeasurably through these past 4 years and I wouldn’t have been able to cope without her.

Table of Contents

List of Figures

List of Graphs

List of Tables

List of Abbreviations

AKH – Adipokinetic Hormone

BSA – Bovine Serum Albumin

BVDV – Bovine Viral Diarrhoea Virus

CHARMM – Chemistry at HARvard Macromolecular Mechanics

DC – Dendritic Cell

DLS – Dynamic Light Scattering

DMSO – Dimethyl sulfoxide

DNA – Deoxyribonucleic Acid

EDC - 1-Ethyl-3-(3-dimethylaminopropyl) carbodiimide

ELISA – Enzyme Linked Immunosorbent Assay

EtOH – Ethanol

FBS – Foetal Bovine Serum

FCA – Freund's Complete Adjuvant

FDA – US Food and Drug Administration

FSH – Follicle-Stimulating Hormone

GH – Growth Hormone

GnRH – Gonadotrophin Releasing Hormone

HEWL – Hen Egg White Lysozyme

HIV – Human Immunodeficiency Virus

HRP – Horseradish Peroxidase

IgG – Immunoglobulin G

i.n - intranasal

IRIV – Immunopotentiating Reconstituted Influenza Virosomes

KLH – Keyhole Limpet Haemocyanin

LDV – Laser Doppler Velocimetry

LH – Luteinising Hormone

LTP – Lipid Transfer Protein

Mθ - Macrophages

MD – Molecular Dynamics

MPL – Monophosphoryl Lipid A

MP-SPR – Multi Parametric Surface Plasmon Resonance

NAMD – Nanoscale Molecular Dynamics

OVA – Ovalbumin

PDI – Polydispersity Index

QCM – Quartz Crystal Microbalance

QCM-D – Quartz Crystal Microbalance with dissipation

Quil A – Quillaia

RMSD – Root Mean Squared Deviation

RPMI – Roswell Park Memorial Institute

Sc - subcutaneous

SD – Standard Deviation

SEM – Scanning Electron Microscopy

SMD – Steered Molecular Dynamics

SPR – Surface Plasmon Resonance

TEOS – Tetraethyl orthosilicate

TMB - 3,3',5,5'-tetramethylbenzidine

TSH – Thyroid Stimulating Hormone

UV – Ultraviolet

VMD – Visual Molecular Dynamics

VPL – Virus-like Particles

Publications and Conference Presentations

Publications

Mulheran, PA; Connell, DJ; Kubiak-Ossowska, K., "Steering protein adsorption at charged surfaces: Electric fields and ionic screening"., *RSC Advances,* 2016, **6,** 73709.

Conference Poster Presentations

Connell, DJ; Ferro, VA; Mulheran, PA - July 2013 CCP5 Summer School University of Manchester, UK

I attended a 10 day Summer school on computational methods of simulating chemical systems. During this Summer school I presented a poster entitled '*Development of a Potential Immunocontraceptive Nanomaterial Using Molecular Dynamics Simulations'*

Connell, DJ; Ferro, VA; Mulheran, PA - August 2013 Northern Postgraduate Chemical Engineering Conference, Department of Chemical Engineering, Newcastle University, UK

Poster presented: '*Development of a Potential Immunocontraceptive Nanomaterial Using Molecular Dynamics Simulations'* – achieved 2nd placed prize.

Connell, DJ; Ferro, VA; Mulheran, PA - March 2014 CECAM Workshop: Simulation Of Biomolecular Interactions With Inorganic And Organic Surfaces As A Challenge For Future Nanotechnologies, LAAS-CNRS, Toulouse, France

Poster presented: '*Development of a Potential Immunocontraceptive Nanomaterial Using Molecular Dynamics Simulations'*

Connell, DJ; Jachimska, B; Ferro, VA; Mulheran, PA - March 2015 Polish Annual Conference on Catalysis, Jerzy Haber Institute of Catalysis and Surface Chemistry, Krakow, Poland

Poster presented: '*Physicochemical Characterisation and Analysis of Peptide Adsorption Onto Inorganic Surfaces'*

Connell, DJ; Jachimska, B; Ferro, VA; Mulheran, PA - June 2015 Surface Science Day, University of Central Lancashire, UK

Poster presented: '*Physicochemical Characterisation and Analysis of Peptide Adsorption Onto Inorganic Surfaces for Use in Immunotherapies'*

Abstract

Vaccines derived from non-pathogenic antigens often have greater safety profiles over live vaccines, whilst still eliciting a specific immune response. However, the decreased immunogenicity of these vaccines means that numerous doses have to be administered or an adjuvant has to be used. In this study gonadotrophin releasing hormone (GnRH), a fertility regulating self-peptide, was used as a model antigen applied to Stober silica nanoparticles (used as an adjuvant) in a vaccine formulation. It is proposed that an inorganic silica nanoparticle can act as a foreign carrier particle for adsorbed peptides, thus stimulating an immune response against these peptides *in vivo*.

This work utilised molecular dynamics simulations of silica substrates and their interaction with peptides for optimal presentation of the peptide to the immune system for antibody production. The interactions at this step allowed the optimum design of the nanoparticle with surface peptides that were free to interact with the surrounding environment, thus having the potential to invoke a biological response.

Quartz crystal microbalance and surface plasmon resonance measurements were also used in order to investigate the adsorption of the peptides onto a silica surface. Through running these experiments at various pH levels and ionic strengths the optimum conditions for peptide coverage of silica nanoparticles could be determined, enabling enhanced design of the silica nanoparticle-peptide system and thus providing invaluable data to inform immunisation studies.

Following an immunological study in male BALB/c mice it was found that the use of silica as an adjuvant along with bovine serum albumin (BSA) as a carrier

protein increased the immunogenicity of GnRH-I peptides in comparison to just BSA alone. It was observed that peptides adsorbed solely onto silica nanoparticles did not elicit a strong antibody response. However, this formulation caused a significant decline in testosterone production, suggesting that silica coated with native GnRH-I peptides could be useful in receptor blocking.

Chapter 1 - Introduction

The aim of this thesis is to investigate the formulation of novel vaccines using silica nanoparticles as an adjuvant for gonadotrophin releasing hormone (GnRH) – a fertility regulating peptide in mammals. One of the major drivers of this project is the use of molecular dynamics simulations to understand how these vaccine systems are assembled, in order to interpret physical characterisation experiments, and more importantly to drive and inform immunological studies. In this chapter, the field of vaccines is introduced; the physiological role of GnRH and its use in vaccine formulations; the importance of adjuvants in the design of vaccines against 'self-peptides'; silica nanoparticles as drug delivery systems; and molecular dynamics simulations as an instrumental design tool for these vaccine systems. The chapter is concluded with a summary of the key points that provide the motivation for the work presented in the remainder of the thesis, and a description of the subsequent chapters.

1.1 Vaccines

The development of vaccinations has been instrumental in disease prevention since Edward Jenner noted that milkmaids rarely suffered from smallpox and they had usually already contracted cowpox (which had much milder effects on humans than smallpox). As such, in 1796 Jenner took pus from a milkmaid Sarah Nelmes' cowpox blister (Figure 1) and exposed eight year old James Phipps' broken skin to it (Jenner, 1798). Six weeks later, Jenner inoculated the child with smallpox and observed that the boy did not develop smallpox symptoms, thus a crude method for vaccine development was established (Baxby, 1999; Plotkin, 2005). However, the idea of using small amounts of infected tissue (or scabs) to protect against infectious diseases has been present for centuries. There are documented reports in 11th century Chinese records detailing immunisation practices against smallpox using nasal

inhalation of infected scabs (Plotkin, 2005). This practice of variolation spread from China to the Middle East and by the 18th century it had arrived in Britain via the Ottoman Empire after Lady Mary Montagu noted the practice in Istanbul.

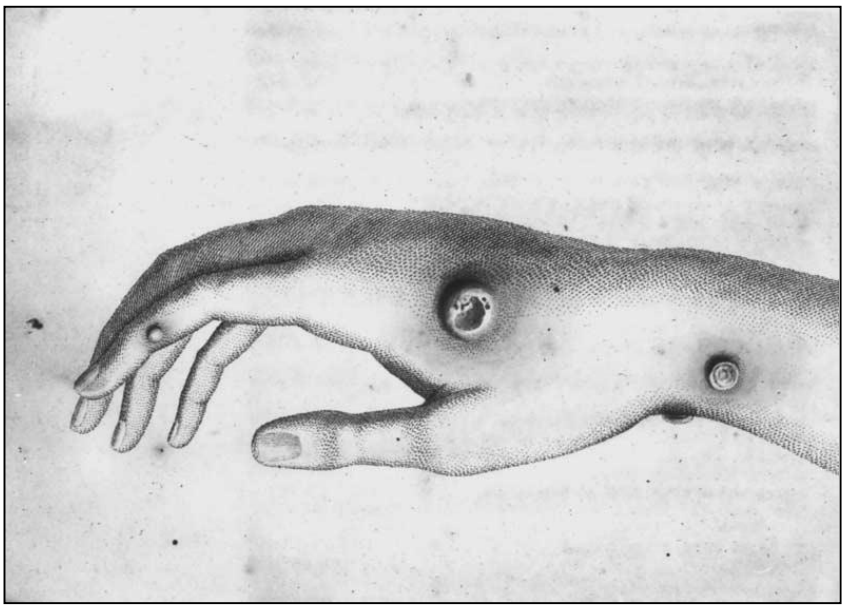

Figure 1: Cowpox lesions from which pus was taken by Edward Jenner to immunise a child against smallpox (image taken from Baxby, 1999).

In 1881, Louis Pasteur created the bedrock for the development of vaccinations as they are currently known. Pasteur found that vaccination with pathogens actively modified using temperature, oxidation or chemical alterations could induce immunity to fresh pathogens with no symptoms as a side-effect (unlike the lesser infections associated with variolation) (Plotkin, 2005). Pasteur used this hypothesis to develop working vaccines for anthrax and rabies, thus cementing vaccinations as a key platform to fight infectious diseases. Consequently, in the last 100 years the use of attenuated virus vaccines has all but eradicated serious diseases such as polio, measles and rubella in the Western world (Toole, 2016).

1.1.1 Live Attenuated Vaccines

A live attenuated vaccine consists of a pathogen that triggers an immune response, but is unable to replicate efficiently in the host and therefore is unable to cause disease. Therefore the patient will be infected and develop long-term immunity to the infectious pathogen, but will not display harmful symptoms. This is usually achieved via biological or chemical modifications, but allows the pathogen to retain the same epitopes that can be recognised by the immune system (The National Institute of Allergy and Infectious Diseases, 2013).

One way in which to attenuate a virus for vaccine development is by growing the virus in cells where they are unable to reproduce effectively, thus causing them to evolve to adapt to the new environment. As a result, the virus becomes weaker in its natural host. This reduces the pathogen's effectiveness as a disease causing agent, but its antigenic components will still be present and recognised as foreign (Ellis, 2001; World Health Organization, 2016). There are various vaccines which have utilised this method in their development, including vaccines for measles and polio. Measles vaccines have been attenuated by passaging the virus through human kidney cell cultures and then chicken embryo cell cultures before being utilised in immunisation studies (Krugman *et al.*, 1962; World Health Organization, 2016) Live attenuated vaccines are advantageous when immunising against a pathogen as it is the closest treatment to a live infection. Consequently, these vaccines are effective at eliciting a strong immune response with only a couple of doses necessary for long-term immunity. However, it is possible that the pathogen in live attenuated vaccines can mutate back into a harmful form. These vaccines can also not be dispensed to those with weakened immune systems, such as individuals undergoing chemotherapy

or who are human immunodeficiency virus (HIV) positive. Another drawback to live attenuated vaccines is that they need to be refrigerated in order to retain their potency, as such these vaccines are not suitable for use in many parts of the world (mainly developing countries) for logistical reasons (The National Institute of Allergy and Infectious Diseases, 2013).

Another method to attenuate a virus for safe use in a vaccine is by passaging the virus *in vitro* at varying temperatures to select mutant viral strains. The resultant mutant pathogens are only able to replicate and grow at lower or higher temperatures than would be possible *in vivo*. This method has been used to synthesise novel live attenuated influenza vaccines. These vaccines have been shown to have a greater immunogenicity than inactivated vaccines, thus providing greater protection from influenza infection (Zhou *et al.*, 2012; Maassab, 1967).

Modifying viral genes so much that reversion to the original configuration is extremely unlikely, thus favouring the *in vivo* stability of the attenuated virus, is known as recombinant virus vaccinology (Ellis, 2001). A similar method can be used to attenuate bacteria for use in a vaccine. However, to ensure vaccine safety, more than one gene associated with bacterial colonisation, survival or virulence must be deleted. This has been achieved via genetic engineering of cholera for oral vaccine development (Chen *et al.*, 2016; Tacket *et al.*, 1992).

The use of recombinant viral technology has also allowed genetically modified viruses to be used as delivery systems for ‘foreign’ pathogenic material. As a result, the desired pathogen can be presented to the immune system *in vivo* as an infectious attenuated virus. This allows the immune system to react to the delivered

pathogen as ‘live’ material and thus encourages increased specific and non-specific immunity to the desired antigen (Ellis, 2001). However, if the subject has pre-existing immunity to the viral vector then the treatment would be ineffective in creating immunity to the delivered pathogenic material. This effect could possibly be overcome by using an alternative route of vaccination of increasing vaccination dosage (Nayak *et al.*, 2009; Pandey *et al.*, 2014).

1.1.2 Inactivated Vaccines

It is also possible to produce inactivated vaccines. These vaccines generally have poorer immunogenicity than live vaccines as the pathogen is unable to replicate in the host cell, therefore it will not continuously stimulate immune cells to provide lasting protection against the associated viral antigens. As such, multiple vaccination doses are often required to provide effective immunity.

For inactivated virus vaccines, whole live virus particles are collected from cell cultures and are usually chemically inactivated (e.g. treatment with formalin [40% solution of formaldehyde], which fixes cells by cross-linking amino groups in proteins with other proteins and DNA). *In vivo*, these inactivated vaccines work because the immune system recognises surface protein conformations (which are also presented in the live virus) and therefore a specific T-cell response can be elicited (T-cells are a type of lymphocyte [subtype of immune cell] produced in the thymus that are key in cell-mediated immunity, which does not involve specific antibodies). However, as the virus is not live it cannot replicate upon infection, and thus humoral immunity (immunity involving specific antibodies and cytokines) is more likely to be induced; further doses are therefore necessary to produce a long-term specific immunological response (Ellis, 2001; Janeway, 2001).

Inactivated vaccines are used to immunise against tetanus. The harmful toxin that is produced by the bacterium *Clostridium tetani* can be purified from a bacterial culture and then inactivated via chemical treatment (e.g. with formalin). The resulting 'toxoid' can then be used as an inactivated vaccine (Ellis, 2001). Inactivated vaccines are often more stable than live vaccines and do not need to be refrigerated when stored and thus are more accessible globally. These vaccines can also be safer than live vaccines as the microbes used are dead and are unable to mutate to a harmful form (The National Institute of Allergy and Infectious Diseases, 2013).

1.1.3 DNA Vaccines

DNA (deoxyribonucleic acid) vaccines can be used to induce a long-term specific immune response. This type of vaccine involves immunising a subject with genetically engineered DNA to produce an antigen. The pathogen gene which is associated with the antigen for which immunity is desired is cloned and inserted into a bacterial plasmid expression vector system (pDNA). The gene is then amplified in the new bacteria cell culture and the purified pDNA can be used for vaccine formulations.

DNA vaccines generally target antigen presenting cells (APCs) or outer body layer cells like muscle cells or keratinocytes in the skin (Huygen, 2005). DNA vaccines target keratinocytes via delivery by gene gun, which involves forcing dried pDNA on gold nanoparticles into target cells using high pressure (McCluskie *et al.*, 1999). Once in the cell, the pDNA is processed, which allows the induction of specific CD8+ T cell immunity (T cells which express CD8 glycoprotein on their surfaces. These cells destroy tumour cells and those cells infected with a virus).

However, the process of forcing antigens into cells can also cause cell death. The dead cells are taken up by APCs, which can lead to the antigen being presented to CD4+ T cells. Consequently, more than one type of immune response can be induced by gene gunning of DNA vaccines (Bergmann-Leitner *et al.*, 2004).

Currently DNA vaccines are mainly used in animals (antibody induction in mice against hepatitis B virus, influenza and HIV amongst others), but the efficacy of such vaccines has still to be thoroughly tested in human subjects with poor immunogenicity of DNA vaccines found thus far in human trials (Kutzler *et al.*, 2015; Rosa *et al.*, 2015). There is one DNA vaccine that is available for humans (licensed in Australia) named IMOJEV™ that is used for frequent travellers to protect against Japanese encephalitis (Halstead *et al.*, 2011). DNA vaccines are useful as there is a low risk of pathogenic infection (particularly compared to live vaccines), they are easy to administer and are cost effective as they require no peptide purification. However, there is the possibility that antibodies to DNA can be produced, which brings into question the safety of this method. There is also a chance that the genes controlling cell growth can be affected adversely (Robinson *et al.*, 2000). Furthermore these antigens can quickly degrade *in vivo*, thus may require an adjuvant (a material that can enhance the *in vivo* immune response to an antigen) for greater stability.

1.1.4 Non-Pathogenic Vaccines

Non-pathogenic derived vaccines are also promising candidates for safe and effective immunisations. These vectors can be used to deliver DNA into cells as part of gene therapy and mimic the natural route of infection and as a result may induce a similar immune response. One such non-pathogenic vector is the parasite *Leishmania tarentolae*. In live attenuated vaccines, the attenuated virus/organism may revert back to a harmful state. However, *L. tarentolae* is unable to replicate in the target cells and is eliminated from the body after a few days, thus has an improved safety profile over other live vaccines. In immunodeficient mice, this non-pathogenic vector has displayed the ability to induce a specific CD8+ T-cell response against HIV (Bolhassani *et al.,* 2012). *L. tarentolae* has also been used effectively in eliciting humoral and cellular responses in mice against HPV16 E7 (human papillomavirus), which is known to increase the risk of cancer development in those infected with it (Hosseinzadeh *et al.,* 2013).

Non-pathogenic derived vaccines can also be used to treat substance addiction. Research on nicotine addiction shows that immunisation using nicotine-haptens (small molecule which can induce production of antibodies) and flagellin, as a carrier protein (acting as an adjuvant), can elicit an effective specific antibody response against nicotine. The use of this adjuvant allows the hapten to be presented effectively to the antigen presenting cells, allowing increased epitope presentation, thus increased antibody response. As a result of immunisation against nicotine, the delivery of nicotine to the central nervous system is more gradual, which has been proven to aid cessation of smoking. The side effects associated with targeting

acetylcholine receptors (as in other nicotine therapies) are also avoided with this method (Jacob *et al.*, 2016).

Non-pathogenic vaccines can also be used to provide a means of birth control (contraception). The human population of the world is now greater than 7 billion and is still increasing. As such, the need for cheap, easy to use contraceptives is also increasing. However, there is a significant proportion of people whose contraceptive needs are not being fulfilled and the number of unplanned pregnancies continues to rise (Garside *et al.*, 2012). One possible way to induce infertility would be to vaccinate against a fertility regulating peptide, such as GnRH (Roch *et al.*, 2011). As GnRH is a 'self' hormone it needs to be conjugated to an adjuvant or carrier protein in order to elicit an immune response. This has previously been undertaken using carrier proteins such as ovalbumin (OVA) and BSA and also with adjuvants such as Freund's (see section 1.3.2) (Herbert *et al.*, 2005).

1.2 GnRH

1.2.1 The biological role of GnRH

GnRHs are a highly researched and well-established vertebrate hormone family. Mammalian GnRH-I was first isolated and sequenced in 1971 by Matsuo *et al.* (1971) and has been found to be of central importance in regulating fertility in vertebrates. GnRH-I is produced in the hypothalamus and is released from nerve endings in pulses every 30-120 minutes. This stimulates the release of follicle-stimulating hormone (FSH) and luteinising hormone (LH), effectively regulating fertility (Roch *et al.*, 2011). LH appears to be dependent on receptor activation by GnRH for secretion, whereas FSH relies more on biosynthesis in the anterior pituitary gland for secretion. It has been shown that in females the GnRH pulse

frequency is highest during ovulation and decreases during the luteal phase of the reproductive cycle (Millar, 2005).

As GnRH effectively initiates the release of reproductive hormones, hypogonadal (individuals with reduced functionality of sexual organs) males and females can have their fertility induced via treatment with low dose pulses of GnRH-I. Similar treatment can also be used to treat delayed puberty in adolescents. However, treatment using high doses of GnRH-I can cause desensitisation of the gonadotrope (cells in this anterior pituitary gland which secrete fertility regulating hormones), therefore a decline in LH and FSH secretion, thus a marked decrease in fertility and sexual organ function (Millar, 2005). The effect of GnRH on hormone secretion is explored in greater detail later in this work. The effect of GnRH treatment on the gonadotrope can be exploited in medicine for a wide range of conditions and treatments. For example, immunisation against GnRH and its analogues can have a major effect on fertility in mammals (both sexes) (Figure 2). This occurs through neutralising antibodies being induced by immunisation that bind to circulating GnRH molecules, thus preventing them from interacting with their target cells to prevent GnRH-induced FSH and LH secretion (Ferro *et al.,* 2004). This then interrupts the hormonal cascade as shown in Figure 2, allowing this effect to be exploited for contraceptive and immunotherapies. GnRH and its analogues can also be effective in treatments for conditions such as endometriosis and prostate cancer (Pham *et al.,* 2016; Barbieri, 1992).

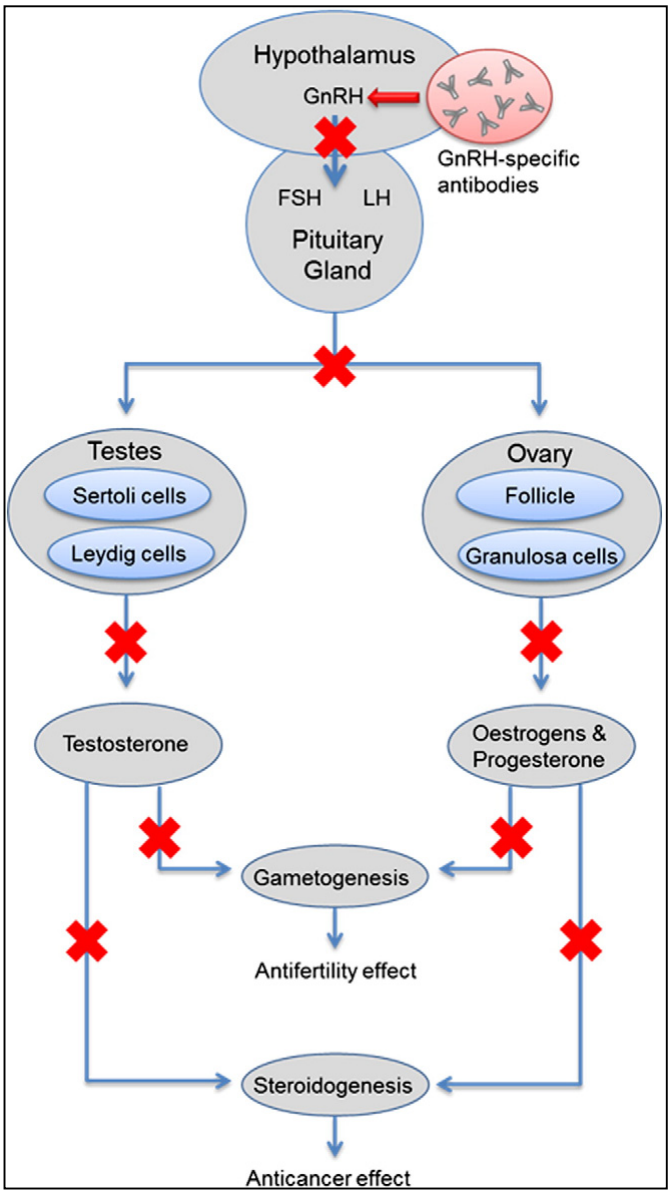

Figure 2: Schematic diagram depicting how interrupting the GnRH hormonal cascade can be exploited to provide a contraceptive effect or potential cancer treatment (image taken from Gebril *et al.*, 2014).

The target of GnRH is the anterior pituitary gland, which produces FSH and LH as well as other classical hormones such as growth hormone (GH) and thyroid stimulating hormone (TSH). However, there is evidence that GnRH stimulates other secretions from the pituitary (that are not LH or FSH) and it can also be found in the cerebro-spinal fluid, which suggests that GnRH may also serve some non-

reproductive functions e.g. influencing neurotransmitter cells in the central nervous system (Skinner *et al.*, 1995).

There are other GnRH molecules present in different species, including invertebrates. However, invertebrates lack an anterior pituitary gland, suggesting that GnRH peptides may perform functions other than the secretion of reproductive hormones in invertebrates (Roch *et al.*, 2011).

1.2.2 GnRH Sequence and structure

GnRH is a short decapeptide, which is common to many mammals. In invertebrates and other species GnRH analogues exist which have different peptide sequences, but retain critical amino acids. As such, functionality of different GnRH peptides may be retained enough so that there is some cross-compatibility between peptides and their target receptors. Currently four main types of GnRH peptide structures are known (I, II, III and IV) (Table 1). The pyro-Glutamic acid group is an amino acid in which the glutamine has formed a lactam ring. Most vertebrates produce both GnRH-I and GnRH-II, whereas fish generally also express GnRH-III and lamprey may also express GnRH-IV (Roch *et al.*, 2011; Sherwood *et al.*, 2005).

Table 1: Sequence profiles of GnRH peptides

Peptide	Structure	Produced	Function
GnRH-I	pyroQHWSYGLRPG-NH_2	Neurons in the pre-optic region	Stimulates secretion of reproductive hormones
GnRH-II	pyroQHWSHGWYPG-NH_2	Midbrain	Neuromodulatory function
GnRH-III	pyroQHWSHDWLPG-NH_2	Telencephalon	Neuromodulatory function
GnRH-IV	pyroQHWSHDWKPG-NH_2		

Many mammals express both GnRH-I and GnRH-II peptides. However, due to evolution and subsequent diversification, the genes responsible for GnRH-II expression have been lost in some mammals. This suggests that the function of GnRH-II may be redundant in modern mammalian reproductive systems. Conversely, in some species (such as the zebrafish) GnRH-III is the main reproductive regulator (Roch *et al.*, 2011). However, GnRH-II has been shown to have the ability to affect sexual behaviour in females based on short-term energy intake, thus demonstrating that the full repertoire of GnRH actions are not fully understood as yet (Temple *et al.*, 2003; Kauffman, 2004).

A study by Stewart *et al.* (2009) into GnRH-II and receptor systems in mammals found that of 22 mammalian species investigated, only 4 have a

functioning GnRH-II system. Amongst the species investigated, humans are placed in the category with an activated GnRH-II system.

Within the 4 main GnRH structures there have been 23 different forms of GnRH peptide found in vertebrates. However, in insects there exists a GnRH receptor superfamily that pairs with peptides that are entirely independent from GnRH (but do share some residues in some cases). There is also a type of GnRH receptor found in octopus that helps regulate reproductive processes. This widespread occurrence of GnRH, GnRH receptors and similar systems suggests that the GnRH family has been influencing physiological processes since before vertebrates even existed and that GnRH must have its roots much earlier in evolutionary history (Roch *et al.,* 2011).

Although there are many varied peptide sequences of GnRH, all GnRH have:

- An N-terminal pyro-glutamate
- Amidated C-terminal
- Most follow the pattern pyroQHWS - - - - PG-NH_2, where the blank residues can be subject to substitution.

From this, it can be observed that the pGlu-His-Trp-Ser and Pro-Gly-NH_2 groups have been conserved through the evolution of GnRH, thus suggesting that these terminal groups are of great importance for receptor activation and compatibility. As such, the presentation of these terminal groups to the surrounding environment is key in the interpretation of results later in this thesis. In GnRH sequences, position 8 is the most variable position, followed by the 6^{th}, 5^{th} and 7^{th} positions. However, mammalian GnRH type I receptors require a charged arginine residue in the 8^{th}

position, hence this residue must play a significant role in ligand selectivity (Millar, 2005). This structural feature will also play an important role in the analysis of results in this thesis.

1.2.3 GnRH Receptors

All mammals have a GnRH type I receptor and some retain the type II receptor. The GnRH-I receptor was first isolated in mice and it has been shown that disruption of the GnRH-I receptor in mice causes direct reproductive defects. There are similar receptors in mammals, such as the oxytocin receptor, but this binds different hormones based on structure – GnRH is a hairpin loop in structure, whereas oxytocin is presented in a ring-like structure. In insects, there are also similar receptors, such as the adipokinetic hormone (AKH) receptor which pairs with a 10 amino acid long peptide sequence (the same length as GnRH), thus suggesting that GnRH receptors belong in a superfamily of similar structures (Roch *et al.*, 2011).

GnRH receptors all have G-protein coupled receptors and conserve certain regions of amino acids. These receptors have a N-terminus followed by 7 α-helical transmembrane domains which are connected through 3 extracellular loops and 3 intracellular loops (Figure 3). The extracellular domains are generally involved in ligand binding, whereas the transmembrane domains exhibit a conformational change to the tertiary structure upon receptor activation (Naor, 2009; Millar, 2005).

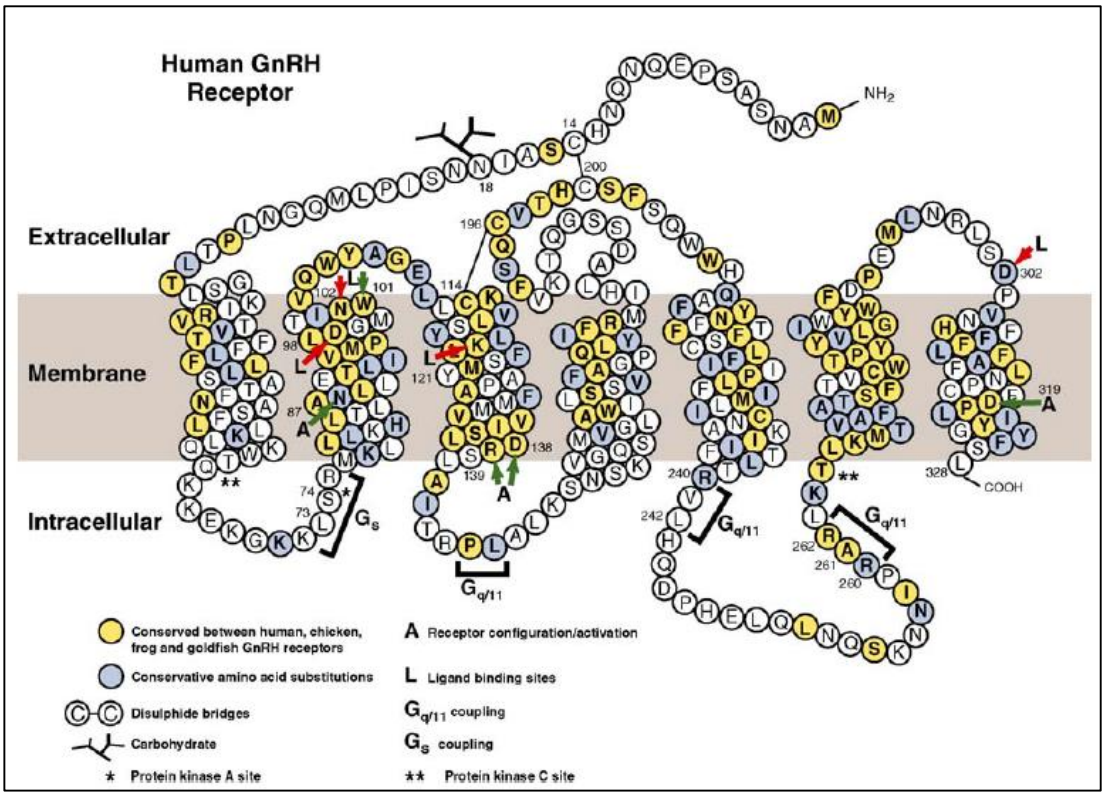

Figure 3: Schematic diagram of the human GnRH receptor with amino acids described by single letter codes (Yellow = shared GnRH receptor residues; Blue = Possible substituted residue). Binding sites, activating sites, disulphide bridges and G-protein coupling are labelled. Extracellular, intracellular and plasma membrane areas are also indicated (image taken from Millar, 2005).

Activation of the receptor leads to the release of FSH and LH from the pituitary gland. This happens through signalling from the $G_{q/11}$ G-protein, which causes phospholipase C release resulting in an accumulation of inositol triphosphate (IP_3). Consequently there is a calcium release and protein kinase C activation which stimulates the release of gonadotrophins from the pituitary. Upon receptor activation there is a conformational change which begins with the initial GnRH binding step. This allows the receptor to adopt a transitional phase which leads to the formation of a ternary complex which has a greater affinity for GnRH ligands and becomes more stable with increased ligand binding (Millar, 2005).

Structurally, the main difference between the mammalian type I GnRH receptor and type II receptor is the inclusion of a cytoplasmic tail on the type II

receptor. It has been shown through *in vitro* studies that the type I GnRH mammalian receptor binds preferentially to mammalian GnRH-I, whereas the type II receptor exhibits no strong preference for any GnRH-II peptide over another. Additionally, GnRH-II is also the preferred ligand for non-mammalian receptors (Millar, 2005).

Upon binding to the receptor, mammalian GnRH-I adopts a conformation similar to a hairpin loop where the GnRH termini are closely opposed (Figure 4). This is a result of a β-II turn involving residues 5 to 8 of the peptide (Tyr-Gly-Leu-Arg). The driving force behind this conformational change in the peptide structure is intramolecular reactions caused by the positively charged arginine residue. The initial step of this turning process is induced by intermolecular reactions of the arginine residue with Asp^{302} (aspartic acid) on the receptor. It has been shown that the substitution of the charged arginine residue with another results in a linear tertiary structure, which renders the peptide biologically inactive in mammals. Therefore, the inclusion of a charged arginine residue must be of utmost importance when binding with the mammalian type I receptor (Millar, 2005).

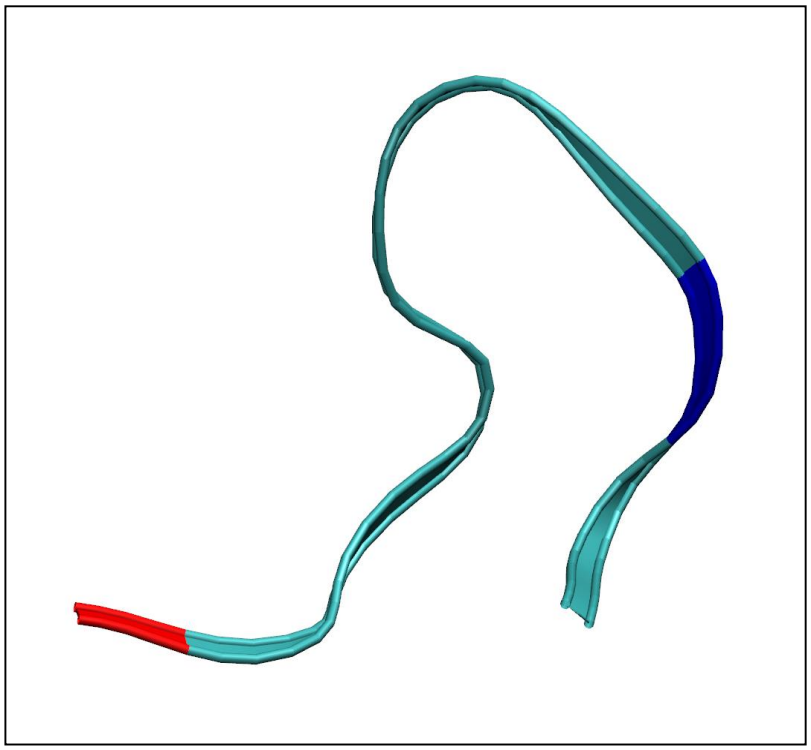

Figure 4: Secondary structure of mammalian GnRH-I which displays the hairpin loop in the GnRH-I peptide conformation. Charged residues have been highlighted (red = negatively charged; blue = positively charged). The N terminus is at the far left with the C terminus at the opposite end of the peptide.

The terminal amino acid residues of the GnRH peptide are integral to receptor activation, the substitution of these residues creates antagonists which may take part in competitive binding with agonist GnRH peptides. This concept will be explored later in this thesis through molecular dynamics simulations. Additionally the substitution of the internal glycine residue (Gly^6) in the GnRH peptide sequence with the D-amino acid increases the activity of GnRH ten-fold in mammals.

As GnRH is a peptide which is produced *in vivo* (i.e. a 'self' peptide), immunisation using just GnRH peptide would not induce an effective immune response as the peptides used would not be recognised as foreign by the immune system. GnRH can also be classed as a weak antigen, due to its low molecular

weight. Consequently, GnRH has to be attached to a large carrier molecule in order to provoke the immune system into a reaction (Herbert *et al.*, 2005).

1.3 Adjuvants

1.3.1 The Role of Adjuvants in Vaccinology

Peptides have many useful functions in medicinal therapies as they are highly selective, have high potency and generally have low cytotoxicity. However, most peptides are small molecules with a short *in vivo* half-life (typically 2-30 minutes) due to rapid excretion and degradation by metabolic processes. As such, the prolonging of the half-life of peptides would greatly increase the effectiveness of the therapy in question. One way in which to achieve a longer peptide half-life is to conjugate the peptide to a carrier molecule like BSA or an adjuvant that cannot be metabolised as quickly (Penchala *et al.*, 2015). However, adjuvants are generally used to enhance the immunogenicity of peptides *in vivo*.

Vaccines made from peptides (subunit vaccines) generally have favourable safety profiles in comparison to live vaccines, but they also tend to have poor immunogenicity as they can be processed and degrade quickly *in vivo* (Mody *et al.*, 2013). The ability of the biological component to elicit an effective specific (and humoral) immune response could be improved with the use of efficient adjuvants, thus providing a platform for peptide vaccines which can elicit a long lasting and effective immune response.

However, the addition of adjuvants to vaccines can cause the antibody response to increase by stimulating a specific cell-mediated immune response more effectively. The presence of the adjuvant enhances the response from dendritic cells

(DCs), thus generating this specific immune response. DC maturation is induced by inflammatory cytokines (secretion which promotes inflammation as an immune response), which is crucial for an immune response; the potency of adjuvants for use in vaccines can be measured by their ability to enhance DC maturation. This can also be advantageous as fewer vaccine doses would be necessary for effective immunisation (Foged, 2011).

Immunity to an antigen can be either innate or acquired. The first response of the immune system is usually the non-specific innate immune response such as physical barriers like skin or mucosal layers or even immune cells like macrophages (mθ), which attack foreign bodies within the bloodstream. Acquired immunity pertains to an antigen specific response, where B or T cells respond to and thus prevent re-infection. The B cell response is humoral immunity and consists of components like antibodies released that target specific antigens in the blood and other macromolecules that target foreign bodies. The T cell response encompasses cellular immunity. The T lymphocyte cells can be classed as either CD4+ T-helper cells or CD8+ cytotoxic T cells. Receptors on T-cells regulate cell activity by creating signals when an antigen (to which there is immunity) comes into contact with the receptor and then these CD4+ and/or CD8+ cells can be generated (Figure 5). The CD8+ cells bind onto the target cell via the antigen associated with the immunity and then destroy the cell. The CD4+ cells can either induce a cell-mediated specific response (Th1 helper cell) or induce a humoral response (Th2 helper cell). The efficiency of the cellular response depends upon the antigen presentation to the T-cell receptors. As such, a major challenge when formulating an adjuvant and carrier molecule is presenting the antigen in the optimal position (Mody *et al.*, 2013).

This is of utmost importance to the work in this thesis and is used to drive molecular dynamics studies of peptide adsorption and presentation to the surrounding environment.

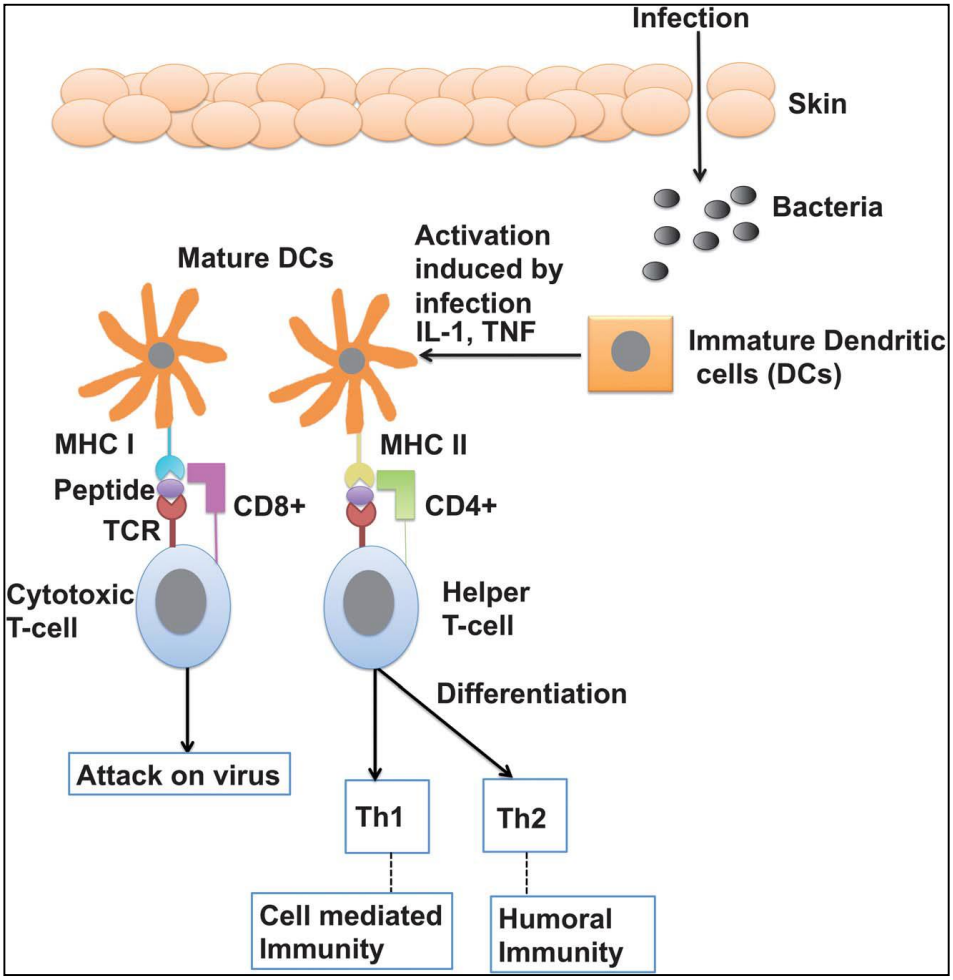

Figure 5: Diagram depicting how humoral and antigen specific responses are generated (image taken from Mody *et al*, 2013).

1.3.2 Adjuvant Types

There are two main types of adjuvants currently known:

- Antigen carrier molecules that enhance antigen uptake by immune cells. These adjuvants induce an innate immune response by stimulating APCs and DCs, thus triggering a localised inflammatory response (Coffman *et al.*, 2010)
- Molecules which enhance the immunogenicity of antigens by promoting antigen uptake and presentation to APCs, resulting in antigen-specific immune responses. (Savelkoul *et al.*, 2015)

At the moment there are very few adjuvants approved for use in humans by the FDA (US Food and Drug Administration) (Mbow *et al*., 2010) due to the perceived side effects and toxicity associated with many formulations. Adjuvants that are currently approved for use in human trials include: Alum salts; Monophosphoryl Lipid A (MPL®); immunopotentiating reconstituted influenza virosomes (IRIV); virus-like particles (VPLs); cholera toxin and MF59® (oil in water vaccine adjuvant).

Polymeric and liposomal adjuvants can be useful for drug release systems and also for antigen release whilst increasing immunogenicity in new vaccines, however they tend to cause tissue lesions at the vaccination site when administered subcutaneously (Gebril *et al.*, 2014). Highly purified Quillaia, or Quil A (bark extract of the soapbark tree – *Quillaja saponaria*) is one of the most common adjuvants used in clinical mice trials. This adjuvant is particularly good for subunit vaccines as they stimulate cytotoxic T-lymphocytes against specific antigens via a Th1 response. Quil A has not been approved for use in human trials as there are often adverse local

reactions at the site of injection and also associated toxicity when used as an adjuvant. Another adjuvant which is often used in clinical animal trials is Freund's complete adjuvant (FCA). FCA is composed of inactivated pathogens (usually bacteria) suspended in an oil emulsion and is usually used to heighten the immune response as it induces both cellular and humoral immune responses – which are desirable qualities for any adjuvant. However, FCA often displays highly toxic effects and can cause severe reactions in subjects, hence it has not been licensed for use in human trials (Freund *et al.*, 1937).

One adjuvant that is currently approved by the FDA for use in humans and has been widely used in existing vaccines (e.g. rabies, hepatitis A and B, diphtheria) is Alum (aluminium salts). The use of Alum as an adjuvant can help induce a strong antibody response as associated antigens are able to remain at the site of injection in larger quantities, thus allowing DCs more time for antigen uptake (Mody *et al.*, 2013). Alum has also been used in combination with MPL A (a lipid based adjuvant) to improve the specificity of vaccines for inducing cell-mediated immunity, as vaccines containing only Alum as an adjuvant only excel in inducing a humoral response. This combination is now licensed for use in human vaccines, however the use of MPL A alone as an adjuvant gives a low specific response (Skrastina *et al.*, 2014). The use of Alum alone as an adjuvant also has other drawbacks. Alum is known to often cause local reactions at the site of injection, resulting in pain and inflammation for the patient. This is due to Alum not being quickly dispersed once injected. Additionally the adsorption of certain proteins to Alum can also destabilise the protein tertiary structure, meaning that Alum is not suitable as an adjuvant for all antigens (Skrastina *et al*, 2014). As such, there is evidently a need for stable

adjuvants with low toxic profiles that can induce a strong specific immune response to a wide variety of antigens with minimal side effects. Silica has been investigated for use in the pharmaceutical industry and has proven to exhibit favourable biocompatibility and can elicit potent antibody responses in immunological studies (Tsirikis *et al.*, 2015)

1.4 Silica Nanoparticles

One possible candidate for an adjuvant for use in vaccine formulations is nanoparticulate silica. Monodisperse silica nanoparticles are relatively simple to synthesise, have good chemical stability, tuneable properties (e.g. size, porosity), low cytotoxicity and good biocompatibility (Du *et al*, 2010; Nozawa *et al*, 2005). Silica is already used in many types of industrial applications including pharmaceuticals, ceramics, catalysis and in coatings. Due to its biocompatibility and tuneable characteristics, the use of various types of silica is constantly increasing in biomedical science, particularly in drug delivery systems (Wang *et al*, 2012).

The properties of silica nanoparticles fluctuate depending on parameters such as the size of the particles, concentration, surface charge and any functional groups that may be attached. There are also various approaches that one can take when using silica nanoparticles as a delivery system as groups can be immobilised on the silica surface and surface interactions can provide optimal conditions for protein adsorption. Furthermore antigens can be encapsulated in silica nanoparticles and due to the insolubility of silica there would be a slow release of antigens *in vivo* (Figure 6) (Mody *et al.*, 2013; Skrastina *et al.*, 2014). There is evidence that silica can be used to improve immune responses. It has been found that amorphous silica has the ability to reduce the potency of circulating mθ and therefore can also increase the

specific antibody response. This is because macrophages compete directly with DCs, which are better equipped to recognise specific antigens and thus effect a lasting immune response (Gennari *et al.*, 1987). As such silica has also been studied for use as an adjuvant in vaccine formulations (Skrastina *et al.*, 2014).

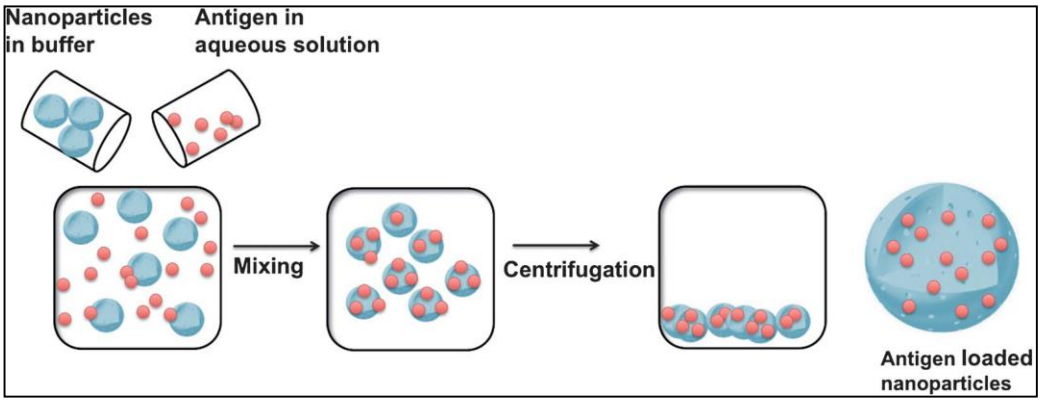

Figure 6: Diagram depicting a simple method of loading silica nanoparticles with an antigen (image taken from Mody *et al.*, 2013).

SBA-15 is a mesoporous silica nanomaterial with hexagonal pores that has good thermal stability and biocompatibility, and therefore is a good candidate for bioapplications. Mercuri *et al.* (2005) studied the use of SBA-15 as an adjuvant for venom proteins of the snake *Micrurus ibiboboca* in subcutaneously administered vaccinations on BALB/c mice. In this study the animals treated with SBA-15 as an adjuvant showed an increased specific immune response, but with no protein release, therefore confirming the role of silica as an adjuvant. SBA-15 also provided a greater specific immune response than Alum, probably due to the effect of silica on the mθ, which would enable the B cells and DCs increased opportunity to provide effective immunity against the antigen.

The potential of silica for use as an adjuvant was strengthened by the US Food and Drug Administration (FDA) authorising silica for use in human trials (Friedman, 2011). However, the biocompatibility of silica depends upon the morphology, concentration, surface functionalisation and nanoparticle size. The size of silica nanoparticles is an important tuneable feature as it can greatly influence protein adsorption and antigen loading. However, smaller nanoparticles (less than 200nm) show toxic effects *in vivo* (Han *et al*, 2011), particles less than 100nm in size can also avoid adsorption by the reticuloendothelial system (mθ and phagocytic cells) and accumulate in cells (Kim *et al.,* 2015; Wu *et al.,* 2011). Smaller nanoparticles have a higher surface area-to-volume ratio and consequently have a higher weight ratio of surface silanol groups, which generate reactive oxygen species that can promote cytotoxic effects. The toxicity of silica nanoparticles depends on the route of administration as well as the route of excretion. Nanoparticles with diameters less than 10nm are renally filtered, whereas larger nanoparticles are generally excreted through the waste system. Nanoparticles larger than 200nm with the same surface functionalisation as smaller nanoparticles exhibit less cytotoxic effects and different *in vivo* properties. The structure and pore architecture of silica nanoparticles also greatly affects the biocompatibility of the adjuvant. The porosity affects signalling pathways involved in the immune response. Mesoporous silica nanoparticles have been shown to have inhibiting effects on mitochondrial and cellular respiration processes, which can cause oxidative stress and therefore cytotoxic effects (Blumen *et al.*, 2007; Mody *et al.,* 2013; Skrastina *et al.*, 2014; Vallhov *et al.*, 2007).

Mesoporous silica nanoparticles have a limited pore size which can restrict the adsorption of large proteins and biomolecules. Non-porous nanoparticles such as Stöber silica are spherical and monodisperse particles which are synthesised by the hydrolysis of tetraethylorthosilicate (TEOS) (Stöber *et al.*, 1968; Nozawa *et al.*, 2005). These spherical nanoparticles are less toxic than porous silica down to a diameter of 100nm with a reduced inflammatory response. Non-porous nanoparticles in the size range of 35-70nm have been shown to cause pregnancy complications in immunised mice. However, coating the silanol surface of the nanoparticle (which is intrinsically simpler with non-porous spherical particles) with polyethylene glycol (PEG) can eliminate haemolytic and cytotoxic effects, whilst also preventing non-specific immune recognition (Lin *et al.*, 2010). The biocompatibility and *in vivo* circulation time of non-porous silica nanoparticles can also be improved through surface modification and functionalisation.

The addition of biomolecules or proteins can improve the biocompatibility of silica nanoparticles. Silica has previously been used to deliver BSA (Lim *et al.*, 2012). BSA is an albumin protein produced in cows that is often used as a lab standard and can be used in drug delivery as a carrier molecule (Sleep, 2014). Mody *et al.* (2013) have used a combination of mesoporous silica, OVA and an antigen associated with bovine viral diarrhoea virus (BVDV). It was found that the inclusion of silica greatly improved the antigen loading capacity and that the properties of the silica nanoparticles (zeta potential and functionalisation) dictate the ability of protein adsorption/desorption. Silica nanoparticles can be used in the adsorption and desorption of a wide range of biomolecules due to their tuneable properties. The surface adsorption properties of these silica nanoparticles can be tuned via altering

the pH, which would alter the zeta potential at the surface. The surface properties could also be changed under the action of enzymes, heat, UV light effects on surface functional groups or with time (Mody *et al.,* 2013).

Hollow mesoporous silica nanoparticles exhibit favourable characteristics for antigen/protein loading. However, loading is often restricted by pore size, but adsorption of proteins onto the nanoparticle surface can circumvent this restriction. Small spherical nanoparticles (like Stöber or mesoporous silica nanoparticles) with a high surface area adsorb BSA well, but this efficiency can be doubled if the silica nanoparticles have a functionalised surface with amino groups. However, increasing the size of these spherical nanoparticles can reduce the rate of desorption of BSA due to the protein 'depot' effect, which prevents large proteins from being released as easily from the nanoparticle. Consequently, this allows for longer periods of interaction between the antigen (which could be attached to the BSA molecule) and the immune system, thus enhancing the adjuvanting effect of the silica (Wang *et al.,* 2012).

For example, the silica-OVA-BVDV antigen immunisation system described by Mody *et al.* induced both a Th1 and Th2 immune response. Silica (SBA-15) has been shown to elicit higher antibody levels than Alum and also showed better induction of immune memory response after multiple immunisations. The adsorption of BSA (as a carrier molecule) to silica adjuvants further increases the amount of antibodies produced. Mice vaccinated with a BSA-silica complex produced a significant amount of BSA-specific immunoglobulin G (IgG) (a Y shaped antibody with 2 antigen binding sites) antibodies.

Although BSA is released more effectively from silica with a negatively charged surface, the surface of silica can also be functionalised in order to make it positive. This can help prevent adsorbed peptide degradation. Positively charged silica can also be used in gene therapies as nucleic acids are negatively charged, so can only effectively adsorb onto a positively charged surface. In this project the relationship between charged silica surfaces and proteins is heavily investigated.

BSA generally adsorbs to silica either through electrostatic interactions or hydrophobic effects, with quick release of the protein suggesting weak adsorption strength. One of the main challenges when formulating a new vaccine with an adjuvant/carrier protein system is finding the optimal combination and conditions that will present the antigen to immune cells effectively. The immune response is highly dependent on how the antigen is presented to the surrounding environment and how stable its interaction with the adjuvant is (Hartono *et al.*, 2012).

1.5 Molecular Dynamics Studies

As the manner in how the antigen is presented to immune cells is of utmost importance when trying to invoke an immune response, the protein adsorption mechanisms must be studied and exploited to encourage optimal presentation. One method in which to achieve this is through molecular dynamics simulations focussing on peptide adsorption on a silica surface.

Molecular dynamics simulations allow for insightful analysis at the atomic level of protein-silica adsorption mechanisms/systems. Simulations can be tuned in order to study the effect of physiological conditions (ionicity, pH and physiological temperature) on protein behaviour over nanosecond timescales or how these

conditions can be altered to provide the optimal environment to promote effective protein adsorption. Consequently, atomistic simulations are a useful tool that can direct and inform 'wet' laboratory research studies.

Jardon-Valadez *et al.* (2009) used a combination of receptor binding studies and molecular dynamics simulations to analyse the importance of Lys191 and the Cys13-Cys200 disulphide bridge on the protein conformation and dynamic behaviour of the human GnRH receptor. As previously discussed, GnRH and its receptor are prime targets for conditions such as prostate cancer and endometriosis amongst others (Barbieri, 1992). It was found through functionality laboratory studies that Lys191 may have an important role in extracellular plasma membrane expression and thus intracellular signalling as its presence appears to have a destabilising effect on the Cys14-Cys200 disulphide bridge (Figure 3)(Lys191 is present in primate GnRH receptors, but not in mice or rats) (Jardon-Valadez *et al.,* 2009). These findings were explained using molecular dynamics simulations as it was shown that the presence of Lys191 in the receptor acts on the disulphide bridge and promotes tension between Cys14 and Cys200, thus slowing down the formation of this bond. Upon substituting Lys191 with another residue (or deletion), it was found that Cys14 and Cys200 interact more readily with each other, suggesting favourable conditions for the formation of the disulphide bridge. As a result, the combination of laboratory methods and computational models were successfully used to show how Lys191 affects the protein conformation and tertiary structure of human and other GnRH receptors (Jardon-Valadez *et al.,* 2009). GnRH has been used in this study as it is a promising target for immunisation and is also small enough so that peptide-surface

interactions can be thoroughly analysed and understood, thus providing immunological studies with information on the dynamic behaviour of GnRH.

Euston (2010) has studied molecular dynamics simulations of protein adsorption at fluid interfaces in order to compare all atom models with that of a coarse grained model (a model, often used in the simulation of proteins, in which groups of atoms are represented by individual atoms, thus allowing for longer simulation times using less computational power). In the food and beverage industry proteins are used to stabilise foams and emulsions by forming a thick layer which prevents rapid breakdown of the foam structure. The ability of the adsorbed protein to act as a stabilising agent depends upon the conformation in which the protein adsorbs to the fluid interface. In oil-water interfaces the adsorbed protein conformation can be influenced by the intrinsic amino acid structure of the protein and the nature of the interface.

Computational modelling can be utilised to ascertain the optimal conditions for protein adsorption to the oil-water interface. Root mean squared deviation (RMSD) of the atomic coordinates of barley lipid transfer protein (LTP) was used to monitor the behaviour of the tertiary structure at the interface. An all-atom model was run alongside a coarse-grained model in order to investigate whether these methods produce comparable results, as a coarse-grained approach would allow for longer simulation timescales with less computer processing power needed. It was found that coarse-grained modelling does allow for longer simulation timescales to be utilised for protein adsorption simulations, thus the post-equilibration behaviour of the tertiary structure can be analysed reliably. However, there can also be different

behaviour exhibited in coarse-grained models than in all-atom models as finer details leading to conformational entropy changes may be missed (Euston, 2010).

Molecular dynamics simulations have also previously been used in conjunction with other quantitative methods to study protein adsorption on silica surfaces. Kubiak-Ossowska *et al.* successfully showed that hen egg white lysozyme (HEWL) adsorbs to a silica surface at pH 7 through mainly electrostatic interactions and how adsorption to the surface affects the protein conformation. This allowed an informed analysis of the experimental multi-parametric surface plasmon resonance results (MP-SPR). The combination of these results provided enough information to deduce that the protein was able to form a closely packed monolayer structure on the silica surface (Figure 7) at higher pH levels (pH 7-10) and that the hydrophobic residues of the protein are exposed to the surrounding solvent when adsorbed as the surface hydrophobicity increases with greater surface coverage (Kubiak Ossowska *et al.*, 2015).

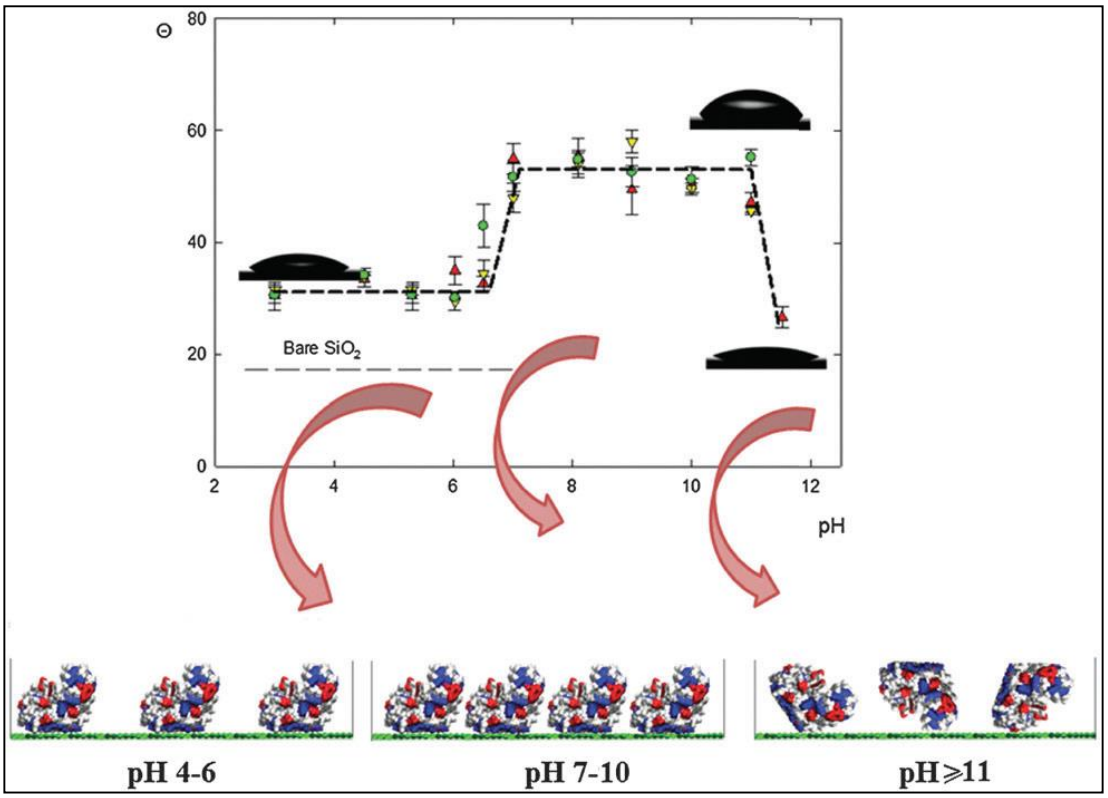

Figure 7: The images at the bottom of the figure indicate the adsorbed protein orientation on the silica surface at varying pH levels. The contact angle measurement for bare and HEWL-adsorbed silica surface within a pH range of 3 to 12 is also shown in the graph. The water droplet shape on the surface is superimposed on the graph. The concentrations of protein is also given with coloured points: Green = 1000ppm; Yellow = 10ppm; Red = 5ppm (image taken from Kubiak-Ossowska *et al.*, 2015).

This explains the observed trends in the water contact angle with HEWL/silica surfaces at various pH. All-atom molecular dynamics simulations allowed this conclusion to be reached as the protein adsorption mechanism and driving force behind the interactions could be analysed over a nanosecond timescale.

1.6 Aims and Objectives of Thesis

This thesis aims to investigate the use of GnRH and its analogues as a model system for vaccine formulations. This includes the role of the hairpin loop secondary structure; the peptide termini and the charged amino acid residues in the vaccine formulation and the associated immunological response. The role of silica nanoparticles as an adjuvant is also investigated. Molecular dynamics simulations have been used in this study to understand the presentation of the GnRH peptide to the physiological environment and how this correlates with an immunological response.

The chapters are structured as follows:

- Chapter 2 provides the theory behind the methodology used in this thesis.
- Chapter 3 used molecular dynamics simulations to show the effectiveness and dynamical behaviour of GnRH peptide adsorption to a silica substrate. The effect of ionic concentration on peptide adsorption and desorption is also investigated.
- Chapter 4 illustrates how effectively GnRH peptides adsorb to silica surface using quartz crystal microbalance (QCM) and surface plasmon resonance (SPR) as physical characterisation techniques. A mixture of these techniques and molecular dynamics simulations are also used to investigate how GnRH peptides conjugated to BSA are presented to the surrounding environment.
- Chapter 5 presents an immunological study of the GnRH vaccine systems investigated in this work. The effect of silica as an adjuvant is explored by measuring specific antibody levels to GnRH-I. The effect of

immunisation with these treatments against GnRH on hormonal pathways is also examined by measuring the effect of testosterone production of treated mice.

- Chapter 6 aims to draw conclusions from the results and discussion presented and highlights areas where future work could be carried out.

Chapter 2 - Methodology

2.1 Simulations

2.1.1 Molecular Dynamics

Liquids were once simulated using gelatine or metal ball bearings, however these physical methods had obvious limitations. To provide a more thorough approach, liquids are now simulated using mathematical models and analysed via computer simulations. Molecular dynamics takes into account the Newton's equations of motion for liquids (Allen *et al.,* 1987). Computer simulations can provide accurate results for statistical mechanics of liquids, which can only be approximated by other methods. These simulations can then be used to provide predictions and insight for wet experimentation (Allen *et al.*, 1987).

The interactions between atoms in a liquid or molecule are caused by the electron clouds around the individual nuclei, but in computer simulations they are approximated by simple empirical forms such as: Van der Waals forces, electrostatics, momentum, kinetic energy, point in space (coordinates) and type of bonding (Allen *et al.,* 1987). Molecular dynamics simulations are run and observed over a finite time, so as to accurately calculate the motion of a molecule in a feasible calculation time. Longer simulations may not be feasible as the Newtonian equations of motion of each atom in the simulation box are calculated on a step by step basis (Allen *et al.,* 1987). Due to vibrational frequencies in molecules, these steps are in femtosecond timescales (10^{-15}seconds), so 10^{6} steps only yields one nanosecond of trajectory. This may take an unreasonable amount of time, even on modern supercomputers. The molecular dynamics approach also calculates the basic thermodynamic properties of a simulation as averages so as not to highlight and extrapolate anomalies (Allen *et al.*, 1987).

The molecular dynamics approach to computer simulations of molecules in a liquid uses statistical methods to calculate molecular fluctuations and must calculate values for each stage of a reversible thermodynamic potential. Any slight difference in the calculated trajectory, caused by fluctuations or arithmetical differences can cause a divergence in the computer generated simulation from the true classical trajectory (Allen *et al.*, 1987).

2.1.2 Water Model

In computer simulations there are various water models that can be used. In all of the simulations that were performed the TIP3P water model was used. The TIP3P model uses water molecules with three sites of interaction - one for each atom. Each atom is also assigned a point charge, with the angle of the molecule being 104.5° (Jorgensen *et al.*, 1983). The TIP3P model used in these simulations also used the Lennard-Jones parameters on each of the atoms of the water molecule.

The TIP3P model is widely used in molecular dynamics simulations as it is a relatively simple model that lends itself to large systems as it can be computed more easily than more complex water models. For example, using TIP4P water model would require a significantly longer computation time as each water molecule has an extra ‘dummy’ atom which carries the negative charge (Jorgensen *et al.*, 1983).

2.1.3 Force Field

In molecular dynamics simulations the force field is a collection of interatomic potentials (energy functions) which define the potential energy of a system. In all-atom systems, parameters are calculated for every atom including hydrogens, rather than a coarse-grained model, which may define certain molecular groups (e.g. methyl groups) as interaction centres.

The potential energy of a system can be subdivided into covalently bonded terms and non-bonded interactions (e.g. Van der Waals (VDW)). This can be simplified with the following equation:

$$E_{Total} = E_{Bonded} + E_{Non\text{-}bonded}$$

Where

$$E_{Bonded} = E_{Bond} + E_{Angle} + E_{Dihedral}$$

And

$$E_{Non\text{-}bonded} = E_{Electrostatic} + E_{VDW}$$

Some force fields also have allowances for hydrogen bond terms.

Non-bonded terms use the most computing power. Van der Waals are usually calculated using Lennard-Jones potentials and the electrostatic effects with Coulomb's Law.

In this work the CHARMM27 force field was used, which is optimised for simulations containing biomolecules and proteins.

2.2 Lab Studies

2.2.1 Silica Nanoparticle Synthesis

Stöber synthesis allows the production of monodisperse, spherical silica nanoparticles and can be tuned to produce a varying size range of nanoparticles (Stöber *et al*., 1968). This was carried out via hydrolysis followed by condensation of tetraethyl orthosilicate (TEOS) in a mixture of water and ethanol with ammonia as a catalyst. The reaction was as follows:

$$Si(OR)_4 + H_2O \rightarrow (OR)_3Si(OH) + ROH$$

$$(OR)_3Si\ (OH) + H_2O \rightarrow SiO_2 + 3ROH$$

- where the R group is an alkyl chain (in this case an ethyl group) (Nozawa *et al*., 2005).

Ammonia was used as a catalyst in this reaction which allowed the formation of spherical particles. Stöber *et al.* (1968) found that the largest silica spheres were formed when the system was saturated with ammonia and the absence of ammonia produced irregularly shaped particles.

However, Nozawa *et al.* (2005) believed that addition rate of reactants is the deciding factor on the morphology and size of silica nanoparticles as the nucleation period is effectively controlled with the changing of reaction speed (Nozawa *et al.*, 2005). They reported that faster addition of TEOS/EtOH reactant gave smaller particle sizes. They theorised that early in the reaction, growth of the particles is controlled by monomer incorporation at the particle surface, but later in the reaction growth is dictated by diffusion at larger radii (Nozawa *et al.*, 2005).

2.2.2 Dynamic Light Scattering

Generally speaking larger particles scatter light well (e.g. dust scattering a sunbeam). This scattering can be exploited for particle characterisation and sizing, which can be performed relatively easily with the only preparation necessary often only dilution. Dynamic light scattering (DLS) is a laser scattering technique that can be used to investigate diffusion of particles in a solution. When in solution the movement of the irradiated (by laser beam) particles results in scattered waves that are picked up by the detector. As there are many particles in motion there is constructive and destructive interference in these waves which causes the light intensity picked up to fluctuate. These fluctuations are time-dependent and are also affected by the Brownian motion of the particles scattering the incident laser. DLS measurements find the diffusion coefficient of the solution, which is the rate of molecular motion present in the sample solution. The diffusion coefficient (D) is given in the Stokes-Einstein equation as:

$$D = \frac{kT}{f}$$

Where T is the temperature and f is the frictional coefficient (the forces that affect a particle's motion). The frictional coefficient for a solution of spherical particles can be given by the Stoke's relation:

$$f = 6\pi a\eta$$

where η is the viscosity of the solvent and a is the particle radius (Atkins, 2006).

2.2.3 Zeta Potential

Zeta potential can be used to measure the overall surface charge of particles in bulk solution. The electric charge on the surface of particles causes the clustering of oppositely charged ions to form around the particle, thus forming an ionic atmosphere in the bulk media. The radius of the sphere that is able to capture these ions (and associated solvent) is known as the radius of shear. This determines the mobility of the particles. The zeta potential can be defined as the electric potential of the radius of shear relative to the overall bulk electric potential (also known as the electrokinetic potential) (Atkins, 2006).

Zeta potential determines the overall kinetic stability of colloidal dispersions. In colloids with small particles, a large zeta potential value indicates that the particles are likely to retain their monodispersity as there is enough electrostatic repulsion between close, similarly charged particles to prevent aggregation. Whereas in colloidal dispersions with a low zeta potential value (or close to the isoelectric point), aggregation is more likely as other attractive forces (e.g. Van der Waals) can overcome the charge repulsion to form clusters. The potential energy of these interactions can be summarised with the following equation:

$$V_{repulsion} = \frac{Aa^2\zeta^2}{R} e^{-s/r_D}$$

Where A is a constant, a is the particle radius, ζ is the zeta potential, R is the distance between particle centres, r_D is the thickness of the electric double layer and s is the distance between the surfaces of two particles (Atkins, 2006).

2.2.4 Surface Plasmon Resonance

Surface plasmon resonance (SPR) is a useful measuring tool for adsorption of a material on a surface. SPR can be used to find the contact angle of adsorbed material on a surface and thus the effective surface coverage, whereas other techniques, such as QCM, also take into account solvent and ions when measuring the mass adsorbed. Consequently, SPR can provide a more accurate analysis of effective surface coverage by a particular material.

SPR monitors the intensity of angular positions of adsorbed material on a surface over a fixed period of time. The adsorbed mass on the surface can be calculated using the following equation:

$$\Gamma_{SPR} = \frac{\Delta\Theta_{SPR} k d_{GnRH}}{\frac{dn}{dc}}$$

where $\Delta\Theta_{SPR}$ is the change in SPR angle; k is a constant obtained via calibration; d_{GnRH} is the thickness of the adsorbed layer (d_{BSA} is used when the adsorption of the peptide-BSA complex is measured); $\frac{dn}{dc}$ is the refractive index gradient of the adsorbed protein layer (Kubiak-Ossowska *et al.*, 2015).

2.2.5 Quartz Crystal Microbalance

Quartz crystal microbalance (QCM) is a useful method to measure protein adsorption. The QCM sensor is a thin disc of piezoelectric quartz crystal with electrodes on opposite sides. Upon application of an RF voltage to the electrodes the disc oscillates at its fundamental resonant frequency. Adsorption of material onto this oscillating disc causes a decrease in this frequency which is proportional to the mass adsorbed (Δm). The Sauerbrey equation gives the relationship for flat, uniform and rigid adsorbed films, where the change in resonance frequency (Δf) is directly proportional to the adsorbed mass:

$$\Delta m = -C\frac{\Delta f}{n}$$

where C is the constant of the crystal (17.7ng/cm^{2}Hz) and n is the overtone number. Hence, it can be seen that a decrease in oscillatory frequency of the disc correlates with the mass of adsorption.

The energy dissipation (D_{dis}) can also be deduced by measuring the decay of the crystal oscillations. This is linked to the energetic properties of the sensor by the equation:

$$D_{dis} = \frac{E_{dis}}{2\pi E_{stor}}$$

where E_{dis} is the energy lost during one oscillation; E_{stor} is the energy stored in the oscillating circuit.

The change in dissipation can be used to give a quantitative measure of the strength of adsorption or formation of layers on the sensor. For layers that are

strongly adsorbed there will be little or no change in the dissipation over time, whereas a layer that is not as strongly adsorbed will show a marked change in dissipation (Jachimska *et al.*, 2012).

2.2.6 Immunological and Cytotoxic Studies

Extensive immunological studies of the proposed vaccine formulations were undertaken and a cytotoxicity study of the silica nanoparticles was performed. A detailed explanation of these studies can be found in Section 5.2.

Chapter 3 – Molecular Dynamics Simulations of Peptide Adsorption

3.1 Aims

Silica nanoparticles are promising adjuvant candidates for novel vaccine formulations as they exhibit tuneable properties, are relatively simple to synthesise and show good biocompatibility (Mody *et al.*, 2013). GnRH and its analogues have also shown themselves to be useful antigens for various treatments (Barbieri, 1992). This chapter uses molecular dynamics simulations and steered molecular dynamics to investigate the adsorption properties of GnRH-I and its analogues on silica substrates.

This chapter aims to:

- Show how effectively GnRH-1, GnRH-II, GnRH-III and cys-GnRH-I bind to a silica surface and if they bind in such a way that the peptide keeps its hairpin loop conformation, whilst also being presented to its surrounding environment in such a way that it could freely interact with immune cells *in vivo*.
- Determine the strength of peptide adsorption on a silica substrate and thus be able to estimate whether the peptides under investigation would spontaneously desorb from silica nanoparticles.
- Investigate the effect of ion concentration on the binding properties of GnRH peptides on silica substrates.

3.2 Materials and Methods

3.2.1 Molecular Dynamics

All computational simulations were calculated using NAMD 2.6 software (Phillips *et al.*, 2005) and with analysis performed using VMD (Humphrey *et al.*, 1996). The CHARMM27 forcefield specifications were used in each simulation. The native GnRH structure used was 1YY1.pdb (Spyroulias *et al.*, 2006) and the cys-GnRH-I peptide was a modified version of 1YY1.pdb where the N-terminal glutamic acid residue was changed to a cysteine residue.

Adsorption simulations were prepared with one peptide close to the silica surface. The system was neutralised with NaCl to either 0.05M or with at least 88 Na and Cl ions in order to create a screening layer of ions. This occurs as the ions move to the positively and negatively charged surfaces and quench the dipole moment of the system, mimicking Debye screening of a charged surface. The system was solvated in a water box that extended at least 15Å away from any protein atom. Surface adsorption simulations were run for 50 nanoseconds and at 310K and contained ~80,000 atoms (with other simulations containing up to ~180,000 atoms). Each simulation included an equilibration and minimisation period before starting. A timestep of 1.0fs was used alongside periodic boundary conditions in all directions with a neutral pH. As periodic boundary conditions create simulation cell copies in all directions, a continuous surface for which peptides can adsorb onto is created. A short time step was used in order to ensure that the force acting on each atom doesn't significantly change during each time step. The Berendsen thermostat was used in order to control the simulation temperature by re-scaling the velocities of simulated atoms. A NVT ensemble was used for all simulations which is influenced by the

following variables: number of particles (N), volume of the system (V) and temperature (T). The electrostatics were calculated using a particle mesh Ewald summation with a cut-off of 12Å. The TIP3P water model, which is commonly used in large biomolecular simulations, was used in all simulations performed. RATTLE was used as the constraints algorithm for all simulations. Constraints solvers are used for the bonds in protein/peptide simulations as proteins tend to contain rigid structures (such as aromatic rings and certain amino acids). Consequently a constraint solver such as RATTLE or SHAKE can be applied to a system with rigid structures to increase the overall efficiency by reducing the complexity of a simulated molecule (Forester *et al.,* 1997).

The simulation allowed 100 ps at the beginning for minimisation of the water molecules around the protein and surface at 310K (body temperature). The entire system then went through a minimisation sequence for 30 ps to ensure that any unphysical overlaps due to method of construction were removed. The entire system was then heated to 310K for 2.7 ns to investigate the GnRH adsorption process at body temperature. The molecular dynamic simulations were then carried out for 50 ns at 310K and subsequently analysed.

The protein structures under analysis varied; GnRH peptides have 10 residues and only differ on 4 residues within the chain (Millar, 2005).

GnRH-I

The structure of GnRH-I analysed was taken from the Protein Data Bank (Spyroulias *et al*., 2006) and is as follows: glutamic acid – histidine – tryptophan – serine – tyrosine – glycine – leucine – arginine – proline – glycine (EHWSYGLRPG). This peptide chain is neutral overall, but does contain charged residues – glutamic acid

carries a negative charge and arginine is positively charged. The N-terminal (at the beginning) is also positively charged and the C-terminal carries a negative charge.

Cys-GnRH-I

The structure analysed is as follows: cysteine – histidine – tryptophan – serine – tyrosine – glycine – leucine – arginine – proline – glycine (CHWSYGLRPG). This peptide chain is positive overall as the only charged amino acid side chain is arginine, which is positively charged. The N-terminal (at the beginning) is also positively charged and the C-terminal carries a negative charge.

GnRH-II

The structure of GnRH-II analysed is as follows: glutamic acid – histidine – tryptophan – serine – tyrosine – glycine – tryptophan – tyrosine – proline – glycine (EHWSYGWYPG). This peptide chain is negative overall as the only charged amino acid side chain it contains is glutamic acid, which is negatively charged. The N-terminal (at the beginning) is also positively charged and the C-terminal carries a negative charge.

GnRH-III

The structure of GnRH-III analysed is as follows: glutamic acid – histidine – tryptophan – serine – histidine – aspartic acid – tryptophan – lysine – proline – glycine (EHWSHDWLPG). This peptide chain is neutral overall, but does contain charged residues – glutamic acid is negatively charged and lysine is positively charged. The N-terminal (at the beginning) is also positively charged and the C-terminal carries a negative charge.

3.2.2 Steered Molecular Dynamics

Steered Molecular Dynamics (SMD) simulations were run in order to investigate protein desorption. SMD uses an external force to speed up protein diffusion mechanisms (Kubiak-Ossowska & Mulheran, 2012). This provides information on the strength of adsorption as the energy barriers which need to be overcome for desorption to take place can be found. As such, an external force in the +z direction (i.e. normal to the silica surface) was applied with a constant-pulling velocity on the adsorbed protein on the silica surface. All other variables were not modified.

It was found that the best choice of pulling velocity was: 0.005 Å/ps. This was achieved by comparing the duration of pulling each atom against the input of energy to the water as the peptide moves. In this method a fictitious atom is joined to the target atom by a spring constant, K, and is pulled. The force of the spring is recorded over time, as is the position of the pulled target atom.A specified atom on the protein backbone was pulled at a constant velocity and the energy required to exact a conformational change was calculated by measuring the force in the spring between transitions.

The energy barrier for each event in the conformational change was calculated from the energy released using the equation:

$$dE = (F_0 + \frac{dF}{2})(\frac{dF}{K})$$

where dE is the energy barrier, F_0 is the force at the end of the event, dF is the force required for the event and K is the spring constant (K = 278pN/Å).

Calculated values were converted into eV by the relation:

$$1pN\text{Å} = 6.24150913x10^{-4}eV$$

In turn, this could be related to the Arrhenius rate of the mechanism, which varies with activation energy. Kubiak-Ossowska & Mulheran (2012) illustrated the relationship between activation energies for molecular processes and their associated Arrhenius rates (Table 2). The values derived from force-distance curves from the SMD trajectories could then be used to anticipate the energy barriers for individual desorption processes and therefore how strongly bound each peptide is to the silica surface.

Table 2: Table of activation energies and their associated Arrhenius rates at physiological temperature

Activation Energy (eV)	**Arrhenius Rate**
1.6	10^{13}s (million years)
1.4	10^{10}s (thousand years)
1.2	10^{7}s (years)
1.0	10^{3}s (hours)
0.8	10^{0}s (seconds)
0.6	10^{-3}s (milliseconds)
0.4	10^{-6}s (microseconds)
0.2	10^{-9}s (nanoseconds)

Further information about protein desorption, readsorption and diffusion mechanisms was acquired by releasing the pulled atom and allowing a molecular dynamics simulation to run as normal.

Activation energies are given to one decimal place due to the amount of thermal fluctuations in the data.

3.2.3 Silica Surface

The silica surface used (taken from Kubiak-Ossowska *et al.* (2012); Patwardhan *et al.* (2011)) was fixed during all stages of MD simulations (Figure 8). It was an array (86Å X 80Å X 13Å) of silicon (+1.11e) and oxygen (-0.66e) atoms with all atoms 1.6Å apart. Overall there was a surface charge density of -0.217e/Å^2, which is similar to the surface charge of mica at neutral pH.

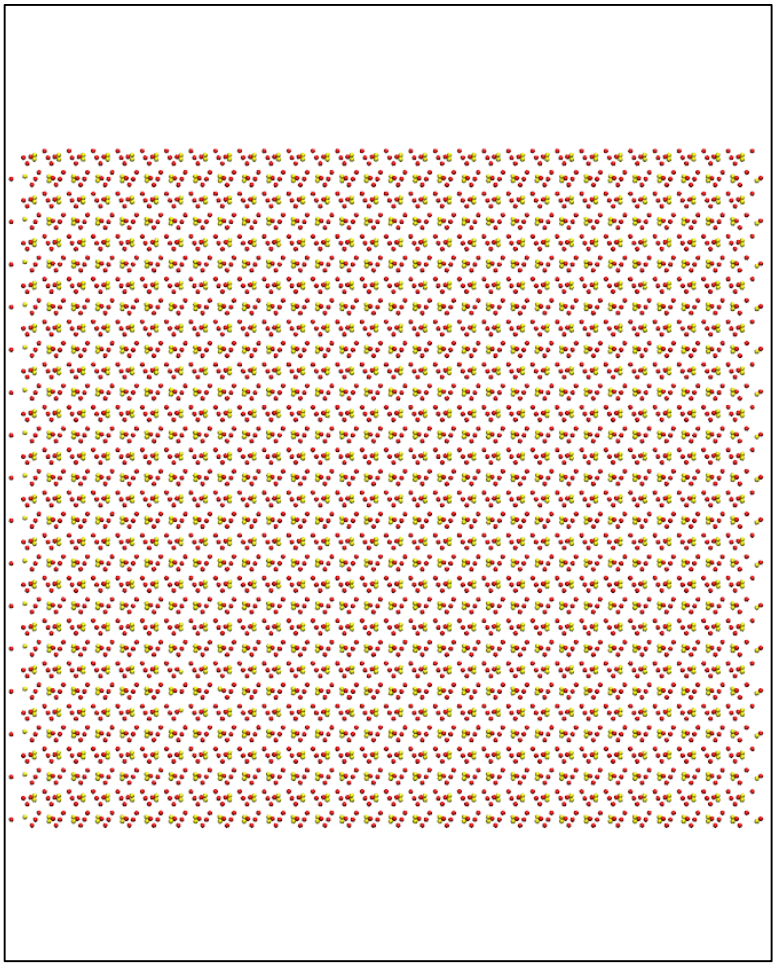

Figure 8: Top down view of silica surface used in simulations. For clarity Silicon atoms = yellow; Oxygen atoms = red.

The surface used quantitatively correlates with experimental data (surface energy, vibration spectra and density). The overall charge of the silica slab is neutral, but is ordered in such a way that more siloxide groups are expressed at the solvent interface, thus creating an intrinsic (negative) dipole moment at the surface. Due to the 3D periodic boundary conditions an electric field is induced through the simulation box, which allows the simulation to mimic a negatively charged silica surface (Figure 9) (Kubiak-Ossowska *et al.*, 2013).

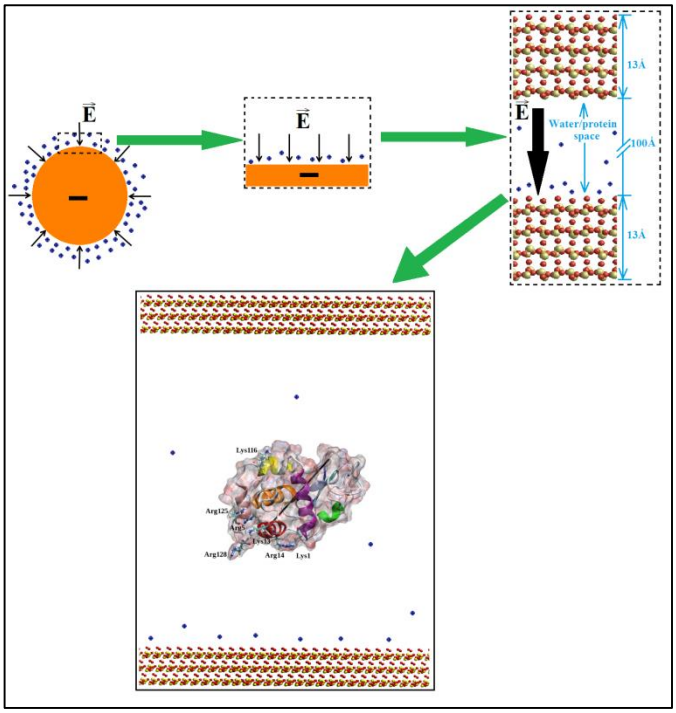

Figure 9: Illustration of the surface concept. On the top left, the electric field of a negatively charged nanoparticle being screened by counter ions in solution. A portion of the nanoparticle is modelled (top middle) as a flat surface. As periodic boundary conditions are employed an electric field is produced perpendicular to the surface (top right) (image taken from Mulheran et al., 2016).

3.3 Results

3.3.1 GnRH-I and Silica Surface

In lower ionic strength it was observed that the native GnRH-I peptide initially interacts with the silica surface through interactions with the positively charged arginine residue, which adsorbs after 9.58ns (Figure 10). The silica surface has a negative charge due to exposed silanol groups. The peptide remained in an upright position presented in the solution and was stabilised via the leucine residue adsorbing to the surface and acting as an anchor (Figure 11). The peptide effectively remained in this conformation until it collapsed on the surface after 49.72ns. Although GnRH-I is shown to successfully form a seemingly strong attraction with the silica surface and stays relatively stable (see Figure 12) for 50 nanoseconds, the peptide is collapsed on the surface.

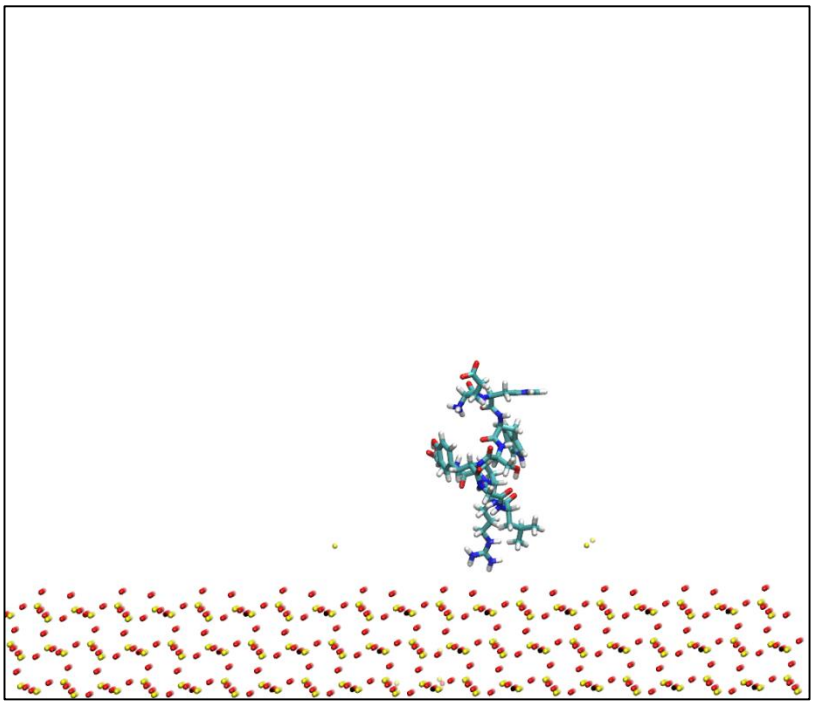

Figure 10: GnRH-I interacting with silica surface via arginine residue. Atoms are coloured as follows: Oxygen – Red, Silicon – Yellow, Hydrogen – White, Nitrogen – Blue, Carbon – Turquoise. The water solvent is not shown for clarity.

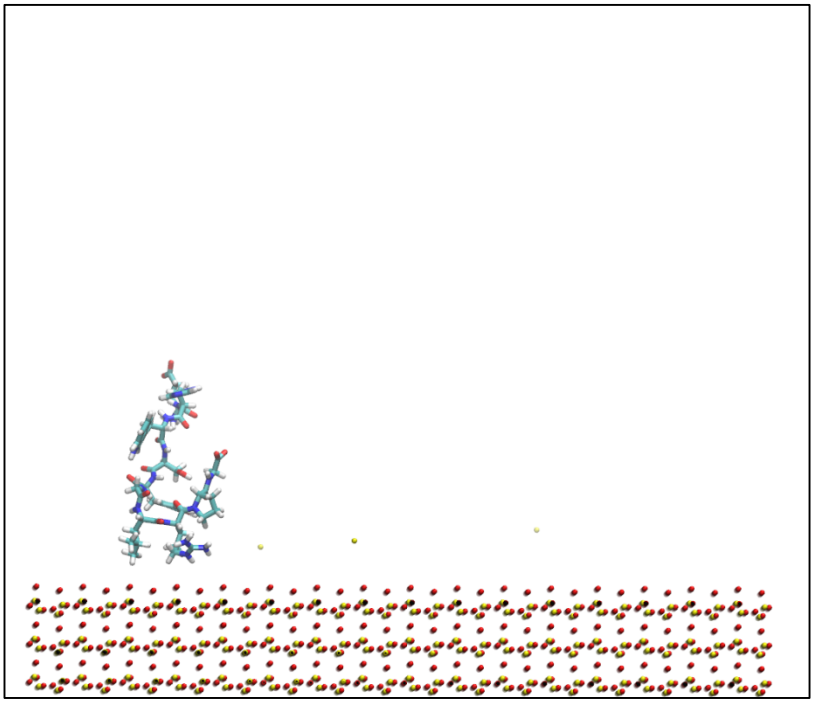

Figure 11: Leucine acting as an anchor during GnRH-I adsorption. Colour scheme as in Figure 10. Water solvent is not shown for clarity.

The simulation was extended to 75 ns, but there was no significant change in the position of the peptide. This is encouraging as it suggests that there is scope for manipulating the interaction between GnRH-I and the silica surface. This could perhaps be done through increasing the salt concentration of the simulation box to a similar level to that which is found *in vivo*.

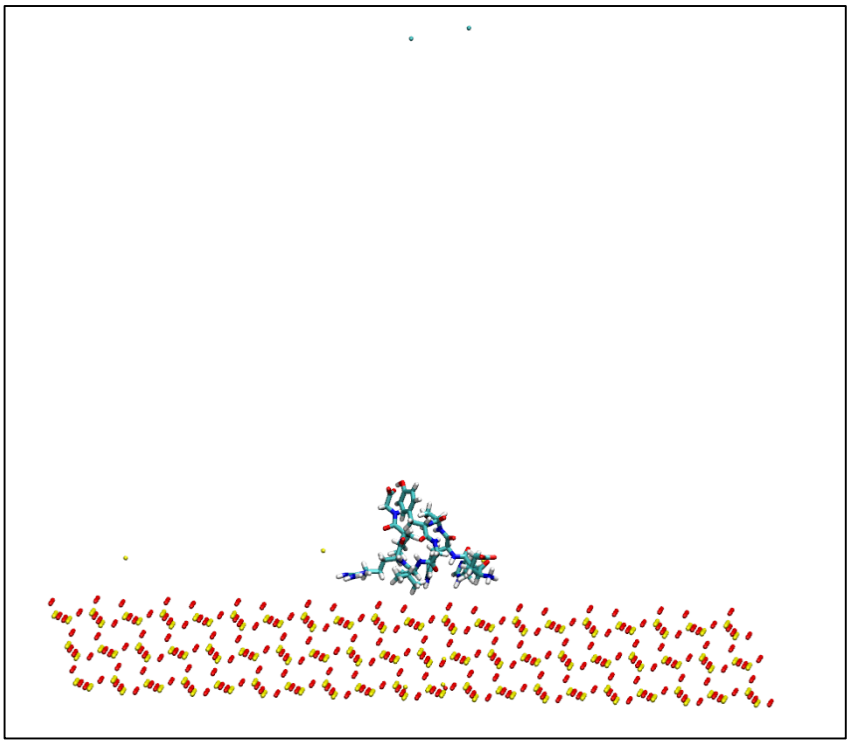

Figure 12: GnRH-I collapsed on silica substrate at a low ionic strength. Colour scheme as in figure 10. Water solvent is not shown for clarity.

Adsorption simulations in a higher ionic strength showed that the native GnRH-I peptide adsorbed via interactions between the surface and the arginine residue after 3.4ns. In this time the Na^+ and Cl^- ions move in the induced electric field, with positively charged ions at the negatively charged bottom surface and negatively charged ions at the opposite surface (top). However, the peptide did not

completely collapse on the surface until 41.4ns into the trajectory (Figure 13). Between the initial adsorption and peptide collapse the peptide is relatively stable on the silica surface in a partially collapsed state. At this stage the N-terminus anchors the peptide to the surface along with the neutral serine residue, this allowed the arginine residue to briefly leave the surface in order for the peptide to retain its hairpin-loop confirmation upon complete collapse to the surface. This might be important for preserving the bio-activity of the peptide once bound to the silica surface.

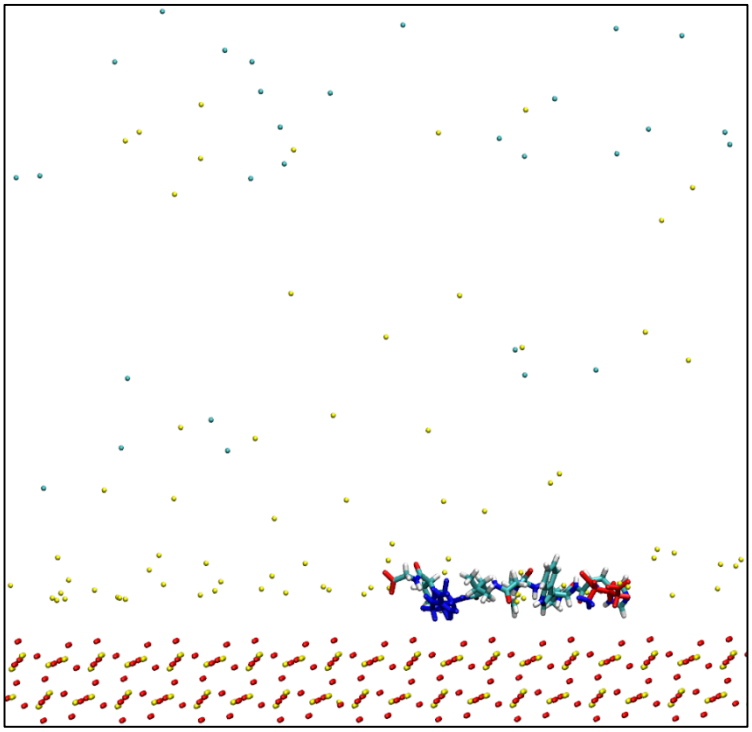

Figure 13: GnRH-I collapsed on the surface in high ionic strength with charged residues highlighted (blue = positive; red = negative). The ions are highlighted as follows: Na^+ = yellow; Cl^- = cyan. Colour scheme as in figure 10. Water solvent is not shown for clarity.

3.3.2 GnRH-II and Silica Surface

In the trajectory of GnRH-II, the peptide initially moved towards the negative side of the silica surface, which is the physically realistic surface. This movement seems to be driven by the interaction between the glutamic acid residue and the surface. However, the peptide only remained in this area for approximately 2.25 ns.

The peptide then moves back through the water to the very top of the simulation box at 9.5 ns. As these simulations comprised of periodic boundary conditions in all directions, the peptide appears to interact quite strongly with the more positive side of the silica surface. This positive surface with silicon exposed is unrealistic and is an artefact of the model construction. This movement appeared to be driven by the interaction between the tyrosine and proline residues with the silica surface (Figure 14). Once bound to the silica surface at the top of the simulation box, the GnRH-II peptide appeared to be relatively stable and was also seen to stay in an upright position.

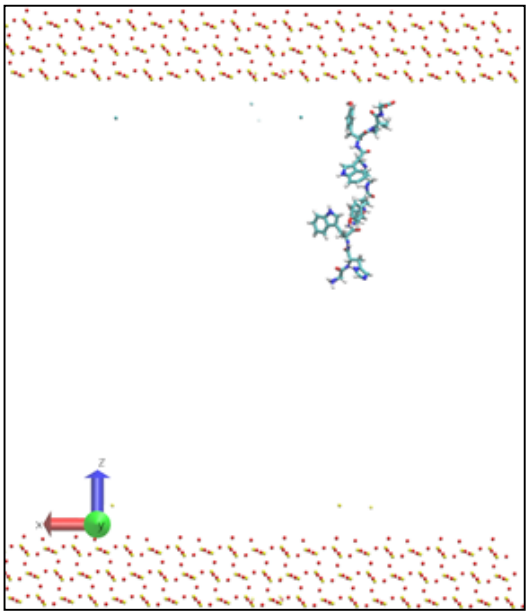

Figure 14 - GnRH-II interacting with silica surface in low ionic strength. Colour scheme as in Figure 10. Water solvent is not shown for clarity.

3.3.3 GnRH-III and Silica Surface

The interaction of GnRH-III with the silica surface took a little longer to initialise in comparison to GnRH-I and GnRH-II. However, it does move towards and adsorb to the negative silica surface after approximately 14.5 ns. This appears to be driven by the interaction between the histidine residue and the silica surface (Figure 15). Once the GnRH-III molecule had attached itself to the surface, the peptide appeared to be relatively stable on the surface and remained in a 'standing' position.

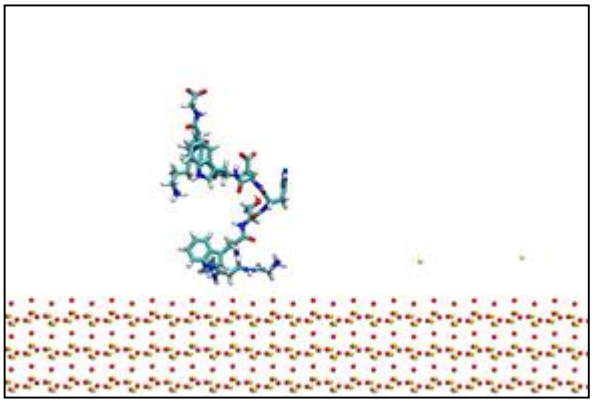

Figure 15 - GnRH-III interacting with silica surface in low ionic strength. Colour scheme as in Figure 10. Water solvent is not shown for clarity.

3.3.4 Cys-GnRH-I and Silica Surface

In solvent with a low ionic concentration the cys-GnRH-I modified peptide was observed initially interacting with the silica surface mainly through the positively charged N-terminal (cysteine residue). In this peptide the negatively charged glutamic acid residue at position 1 has been replaced with a neutral cysteine residue, thus leaving the positive N-terminus charge unbalanced. The N-terminus effectively adsorbs to the surface after 2.2ns of the trajectory and the peptide then adopts a 'standing' position on the surface (Figure 16). The positively charged arginine residue then adsorbs to the surface after 12.98ns after which the peptide collapses onto the silica surface.

In a setting with higher ionic strength the adsorption of the modified cys-GnRH-I peptide behaved in much the same way as in lower salt concentration. The peptide adsorption to the silica surface was once again driven by the positively charged N-terminus. This occurred at 9.87ns, which was longer than without an ionic screening layer above the surface. The arginine residue then adsorbed to the silica substrate shortly afterwards at 11.36ns, which precipitated the permanent collapse of the peptide on the surface. Examples of the collapsed conformation can be seen in Figure 22 in the SMD section (section 3.4.2.1).

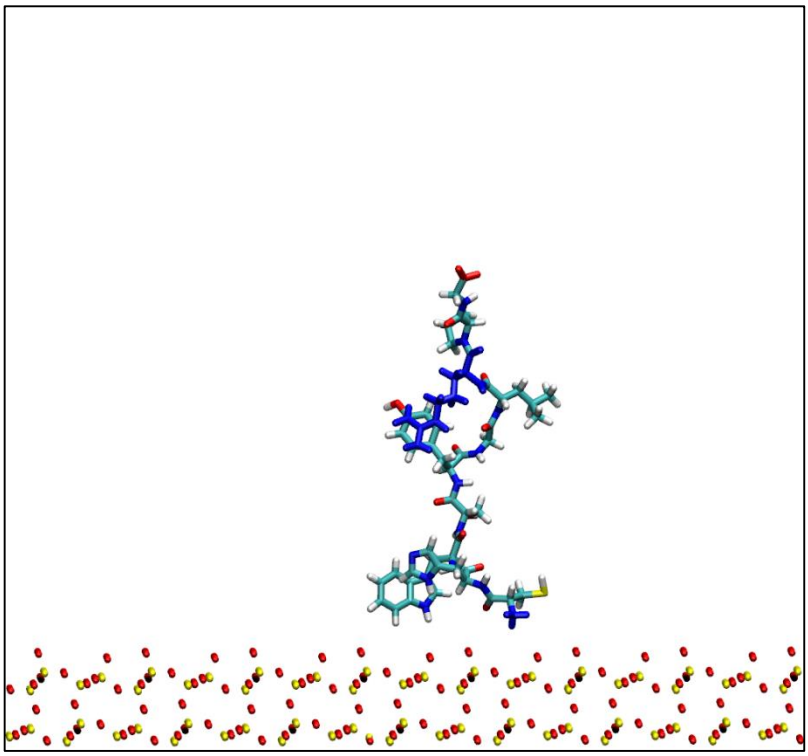

Figure 16: Adsorbing cys-GnRH-I 'standing' on silica surface in low ionic strength with charged residues highlighted for clarity (positive = blue). Colour scheme as in Figure 10. Water solvent is not shown for clarity.

3.4 Steered Molecular Dynamics Results

3.4.1 Native GnRH-I

3.4.1.1 Pulling Arginine Residue

0.05M Ionic Strength (incomplete screening of the charged silica surface)

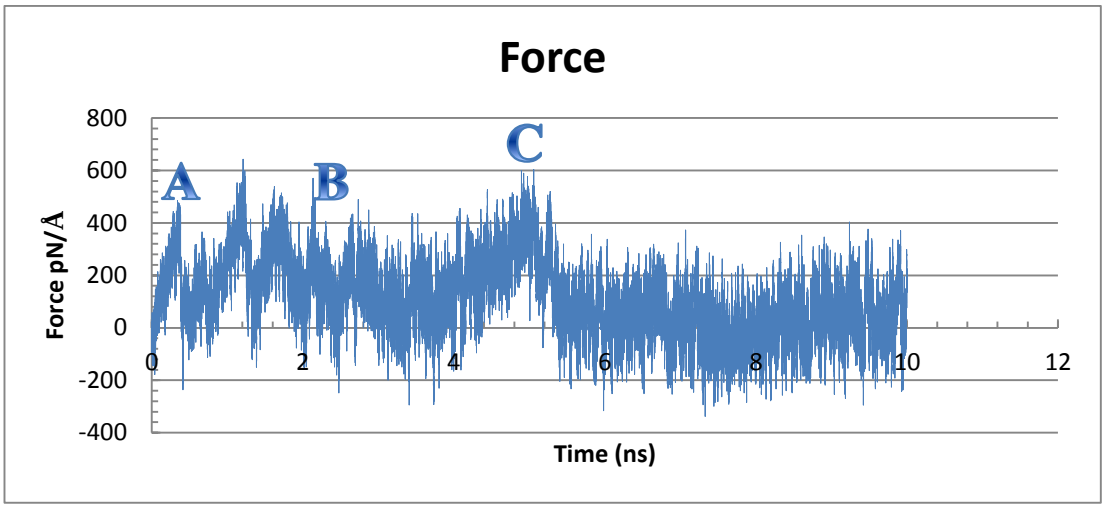

Graph 1: Force against time graph for the SMD trajectory pulling the arginine residue of adsorbed GnRH-I in 0.05M ionic strength

After adsorption (confirmation taken from final coordinates of previously run MD simulations – see section 3.3.1) the arginine residue was pulled by a carbon atom (atom number 124) in the +z direction at a rate of 0.005Å/ps for 10ns in order to investigate the desorption profile and binding energies of native GnRH-I on a silica substrate. Each jump in force correlates with an event in the desorption process, which is labelled accordingly to the corresponding event in Figure 17. The energy of these events was calculated using the equation described in section 3.2.2 and thus the strength of adsorption of each peptide was compared. Figure 17 illustrates the main events in this simulation.

<u>Events</u>

A – Arginine pulled from the surface at 1.38ns → 0.292eV → 0.3eV

B – The rest of the peptide begins to peel off the surface at 2.28ns → 0.16eV → 0.2eV

C – The peptide fully desorbs after 5.52ns → 0.275eV → 0.3eV

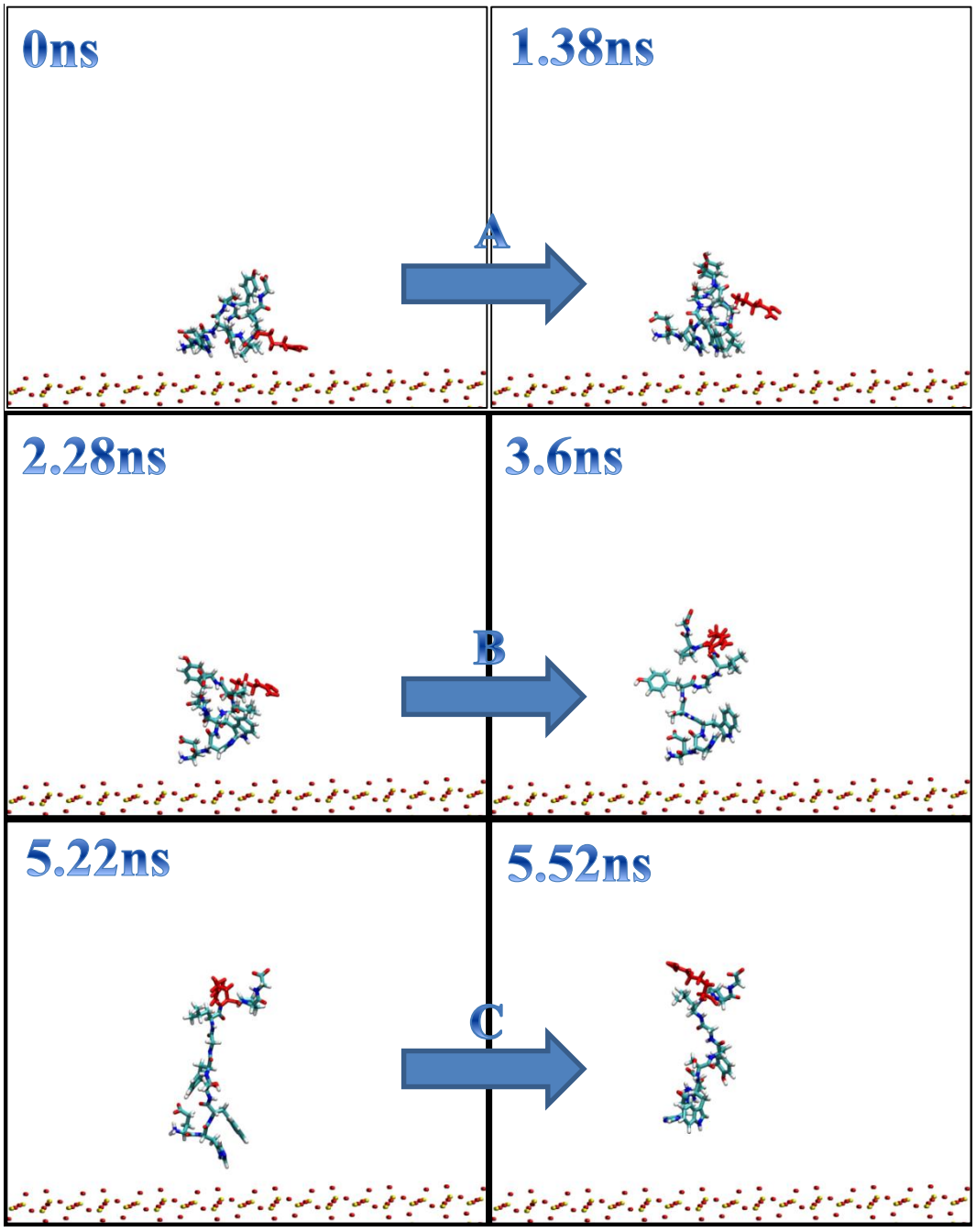

Figure 17: SMD simulation event images for pulling the arginine residue (red) of native GnRH-I in low ionic strength. Water solvent not shown for clarity.

Complete Ionic Screening

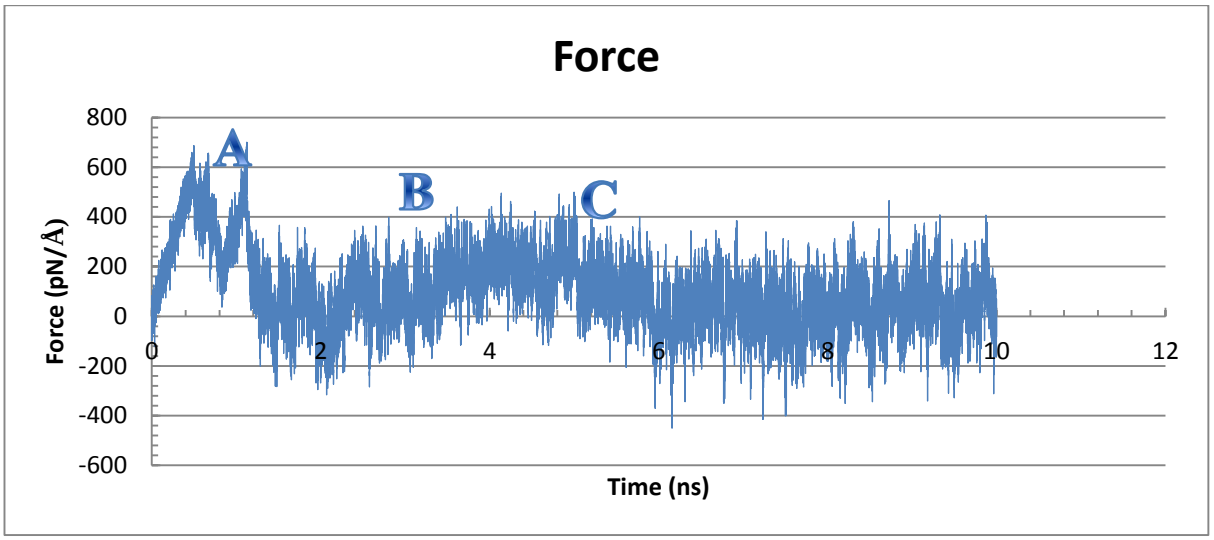

Graph 2: Force against time graph for the SMD trajectory pulling the arginine residue of adsorbed GnRH-I in high ionic strength

After adsorption the arginine residue was pulled by the gamma carbon atom (atom number 124) in the +z direction at a rate of 0.005Å/ps for 10ns as per the previous SMD simulation. However, this SMD simulation was performed at a high ionic concentration to investigate the effect of ionicity of the adsorption strength. Figure 18 illustrates the main events in this simulation.

Events

A – Arginine residue pulled from the surface at 0.64ns → 0.37eV → 0.4eV

B – Rest of the peptide peels off to 'stand' on the surface at 1.96ns → 0.391eV → 0.4eV

C – Desorbs fully after 6.3ns → 0.17eV →0.2eV

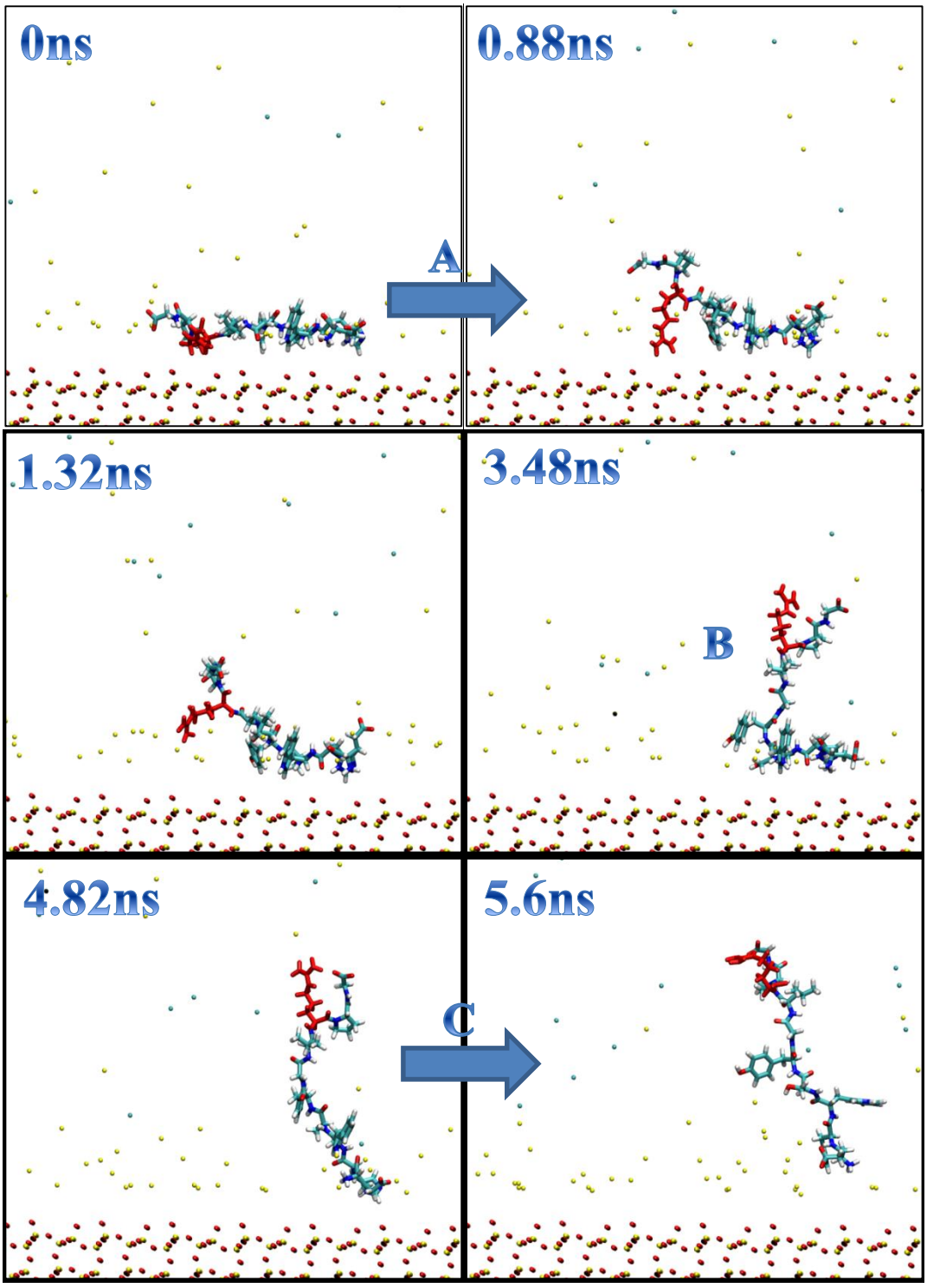

Figure 18: SMD simulation event images for pulling the arginine residue (red) of native GnRH-I in high ionic strength.

3.4.1.2 Pulling N-terminus (Glutamic acid)

Ionic Strength - 0.05M (incomplete screening of the charged silica surface)

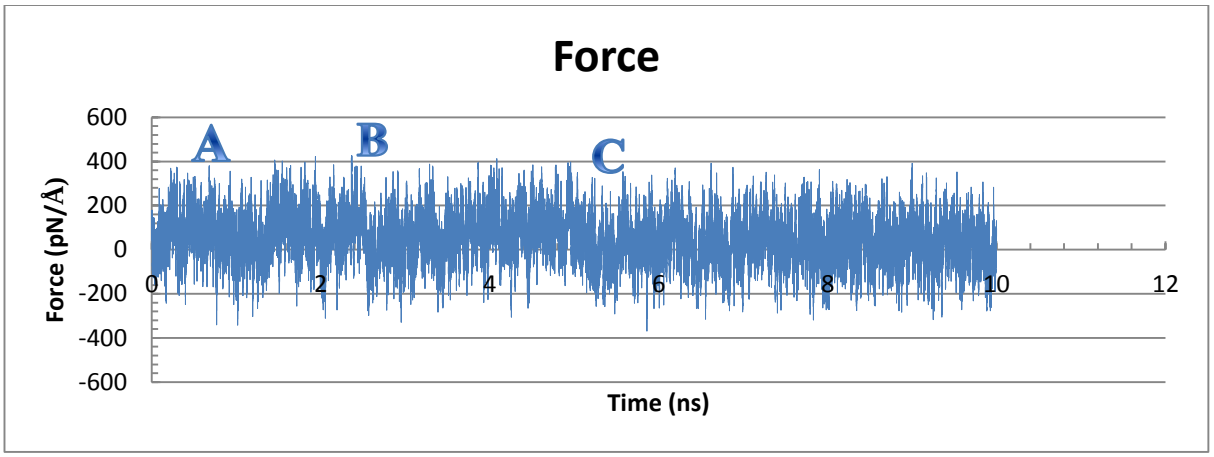

Graph 3: Force against time graph for the SMD trajectory pulling the N-terminus of adsorbed GnRH-I in 0.05M ionic strength

After adsorption the glutamic acid N-terminal residue was pulled by the terminal nitrogen atom (atom number 1) in the +z direction at a rate of 0.005Å/ps for 10ns as per previous SMD simulations. There appears to be a lot of 'noise' in this result, which is due to thermal fluctuations in the simulation, possibly due to the collapsed folded state of the peptide. This measurement was performed at a low ionic strength. Figure 19 illustrates the main events of this simulation.

Events

A – Glutamic acid desorption at 1.18ns → 0.1eV

B – Peptide begins to peel off surface to 'stand' at 2.48ns → 0.065eV → 0.1eV

C – Desorption at 6.14ns → 0.059eV → 0.1eV

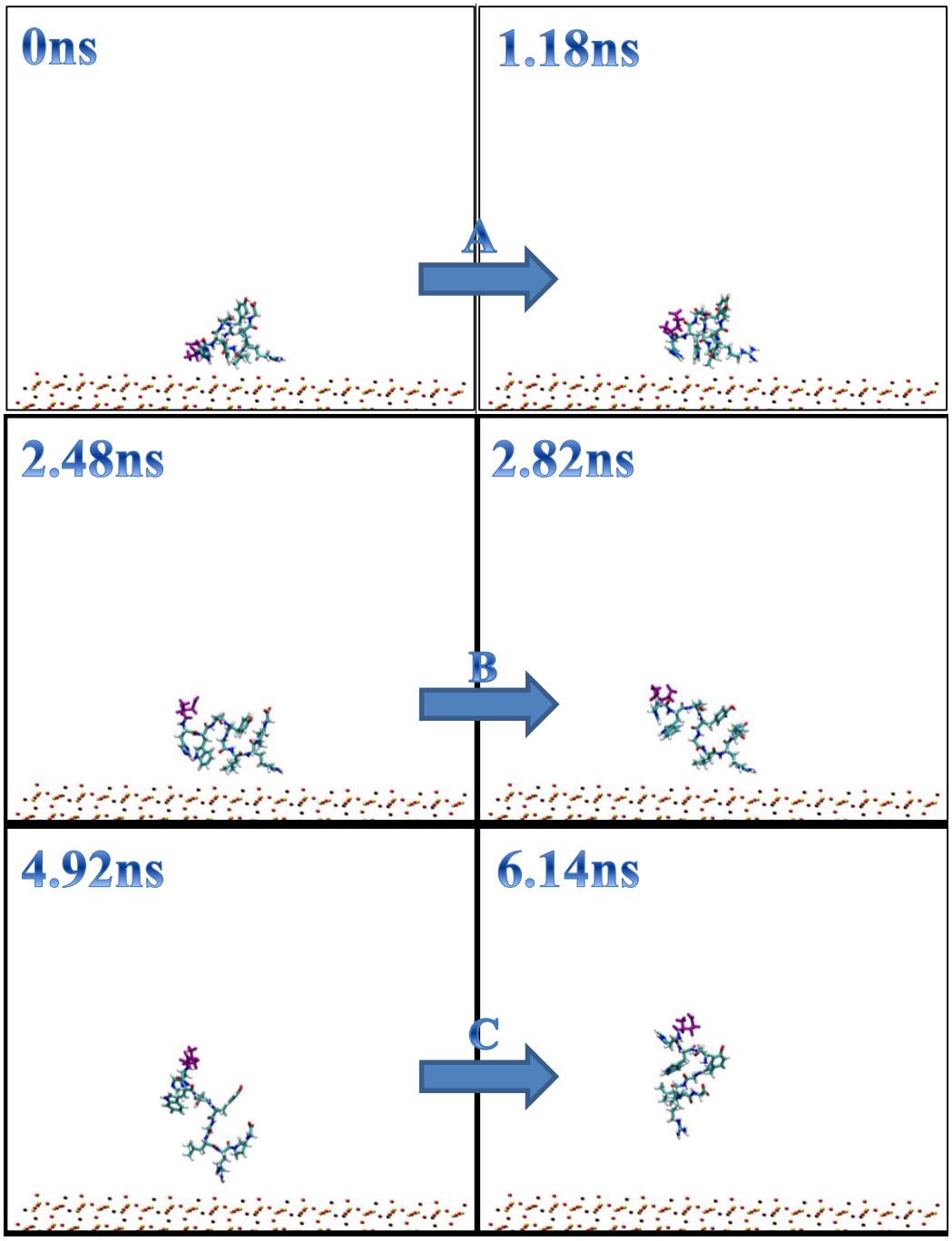

Figure 19: SMD simulation event images for pulling the N-terminal residue (purple) of native GnRH-I in low ionic strength.

Complete screening

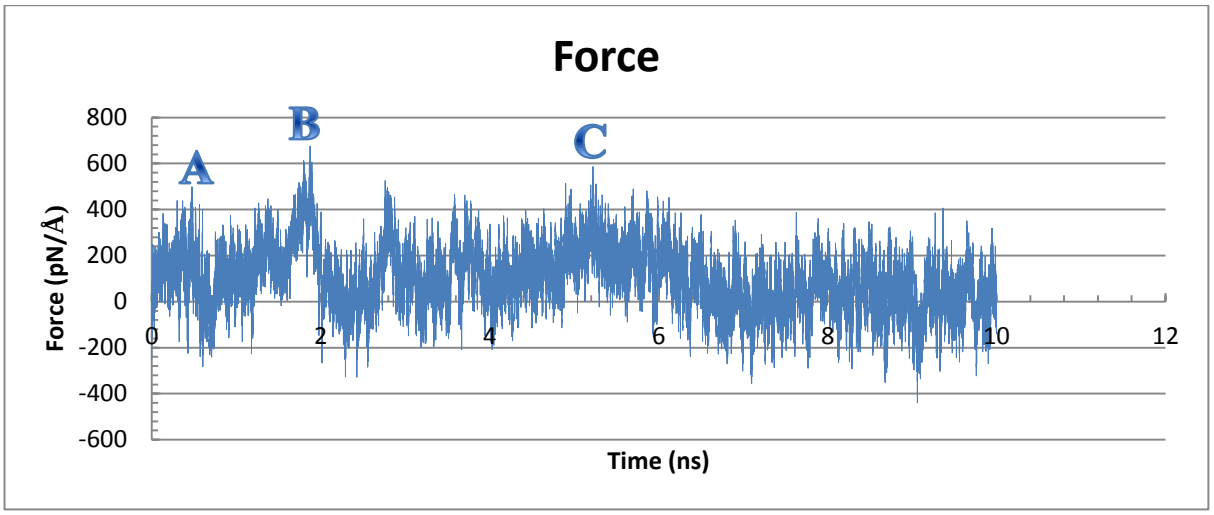

Graph 4: Force against time graph for the SMD trajectory pulling the N-terminus of adsorbed native GnRH-I in high ionic strength

After adsorption the glutamic acid N-terminal residue was pulled by the terminal nitrogen atom (atom number 1) in the +z direction at a rate of 0.005Å/ps for 10ns as per previous SMD simulations. This measurement was performed at a high ionic concentration. Distinct features were observed in Graph 4 for the events in this measurement. Figure 20 illustrates the main events in this simulation.

Events

A – Glutamic acid desorption at 0.88ns → 0.145eV → 0.1eV

B – Peptide begins to peel off to 'stand' on surface at 1.32ns → 0.29eV → 0.3eV

C – Desorption at 5.6ns→ 0.18eV → 0.2eV

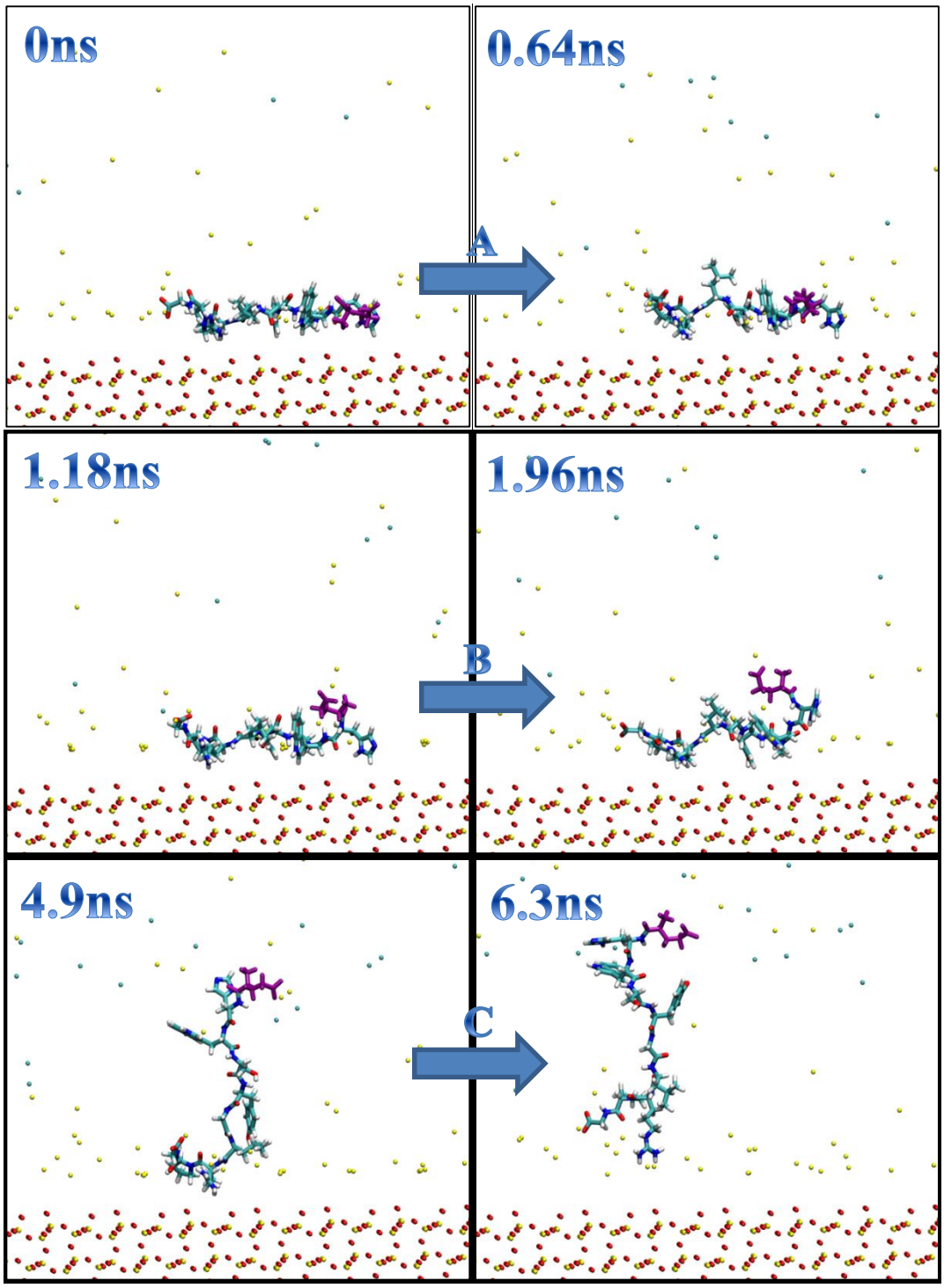

Figure 20 : SMD simulation event images for pulling the N-terminal residue (purple) of native GnRH-I in high ionic strength

3.4.2 Cys-GnRH-I

3.4.2.1 Pulling Arginine Residue

0.05M Ionic Strength (Incomplete screening of the charged silica surface)

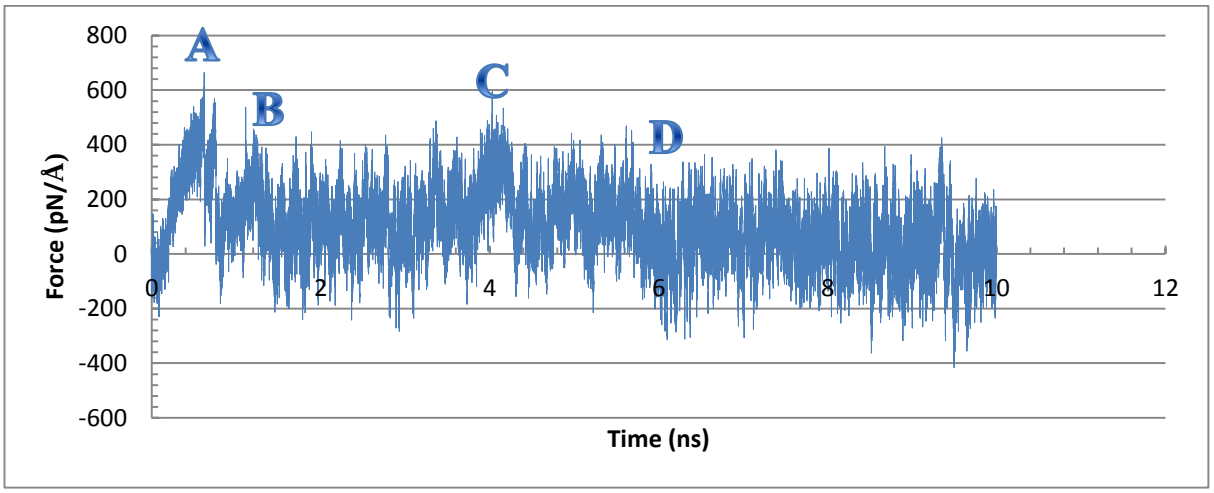

Graph 5: Force against time graph for the SMD trajectory pulling the arginine residue of adsorbed cys-GnRH-I in 0.05M ionic strength

After adsorption the arginine residue was pulled by the delta carbon atom (atom number 123) in the +z direction at a rate of 0.005Å/ps for 10ns in order to investigate the desorption profile and binding energies of cys-GnRH-I on a silica substrate. Each simulation was analysed as per previous simulations. Good features are present on Graph 5. However, event D is more difficult to identify and quantify. Fluctuations of the order 0.1 – 0.2eV are expected on a molecular dynamics timescale (see Table 2 in section 3.2.2). Figure 21 illustrates the main events in this simulation.

<u>Events</u>

A – Arginine desorption at 0.92ns → 0.3eV

B – Peptide begins to desorb at 1.58ns → 0.18eV → 0.2eV

C – Peptide desorbs enough to 'stand' on surface at 3.92ns → 0.22eV → 0.2eV

D – Desorption after 6.36ns → 0.115eV → 0.1eV

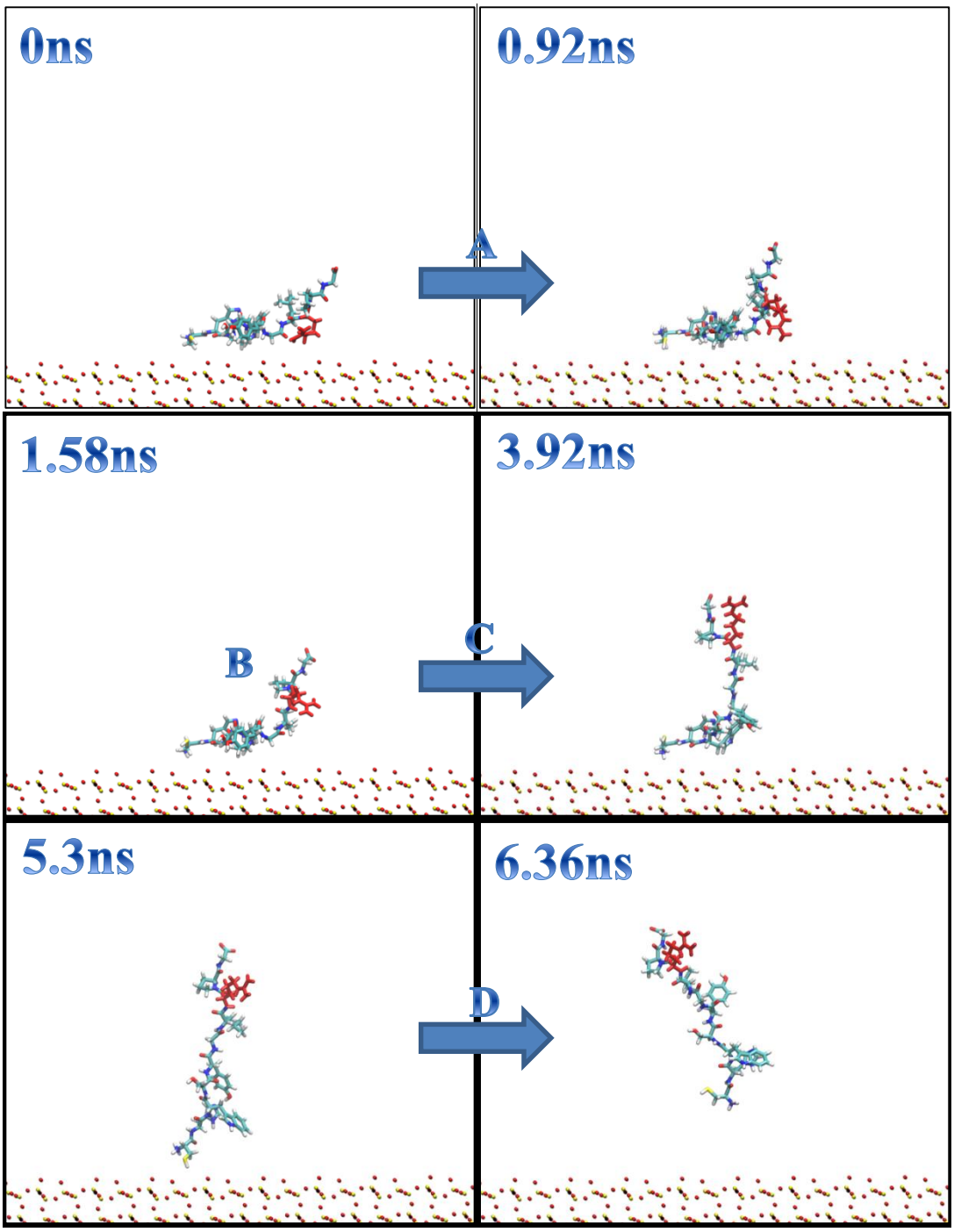

Figure 21: SMD simulation event images for pulling the arginine residue (red) of cys-GnRH-I in low ionic strength

Complete Ionic Screening

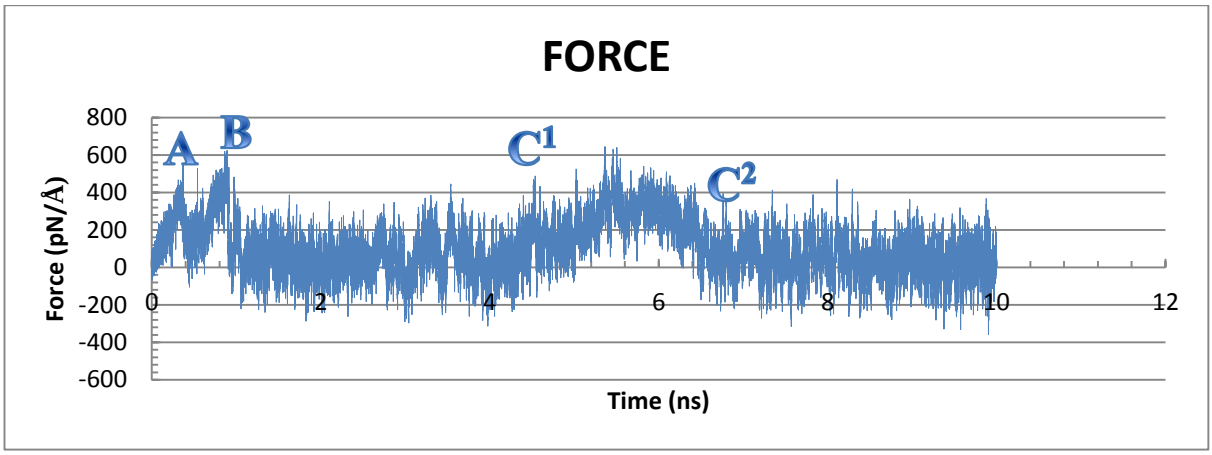

Graph 6: Force against Time graph for the SMD trajectory pulling the arginine residue of adsorbed cys-GnRH-I in high ionic strength.

After adsorption the arginine residue was pulled by the delta carbon atom (atom number 123) in the +z direction at a rate of 0.005Å/ps for 10ns as per previous SMD measurements. This measurement was performed at a high ionic strength. C^1 and C^2 are rather difficult to identify again, but are important events as they comprise of the final desorption steps of the peptide from the silica substrate. Figure 22 illustrates the main events in this simulation.

Events

A – Arginine desorption at 0.64ns → 0.25eV → 0.3eV

B – Peptide begins to 'stand' on surface at 1.22ns → 0.34eV → 0.3eV

C^1 + C^2 – Desorption from 5.16 to 6.4ns → 0.27eV → 0.3eV

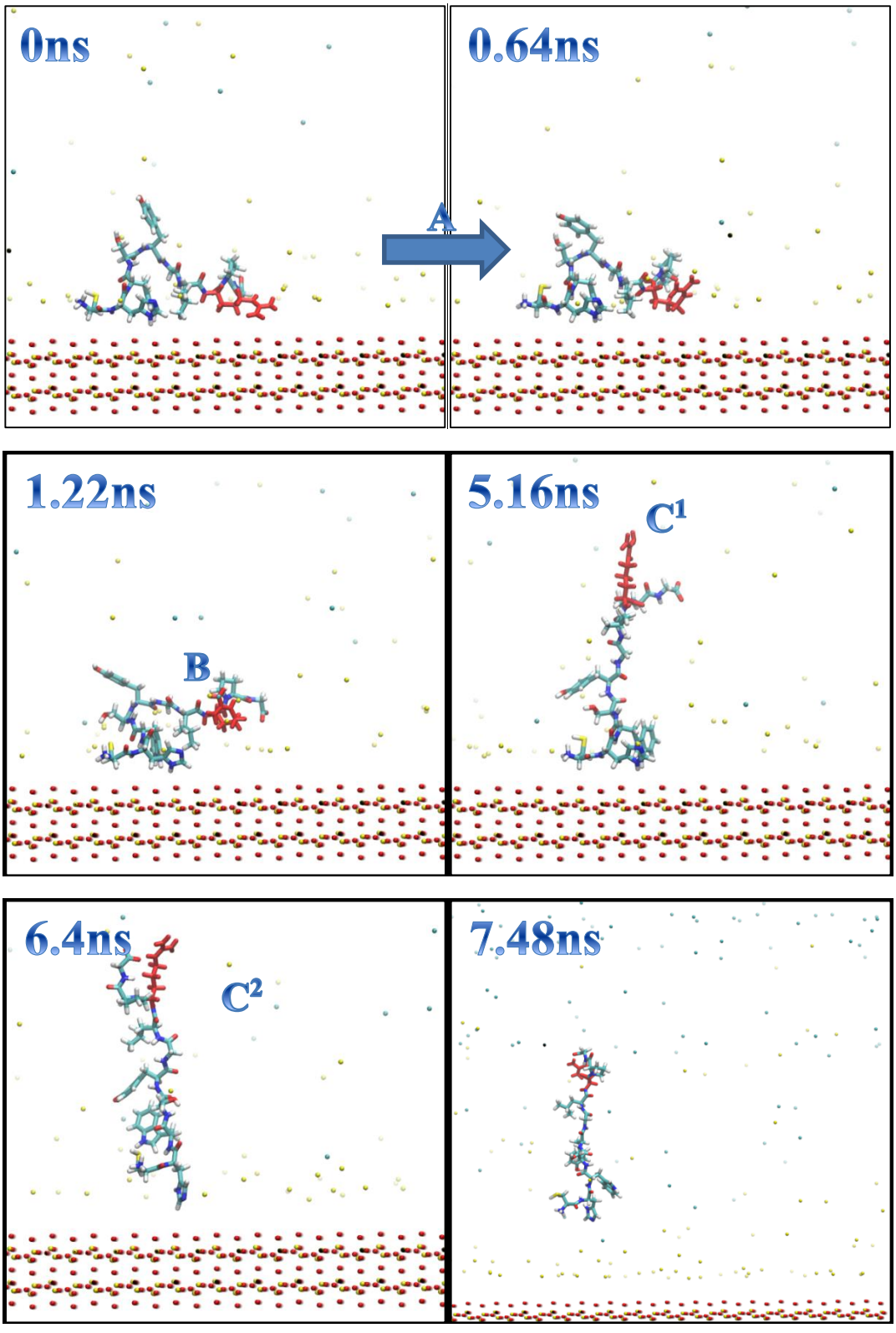

Figure 22: SMD simulation event images for pulling the arginine residue (red) of cys-GnRH-I in high ionic strength

3.4.2.2 Pulling N-terminus (Cysteine)

0.05M Ionic Strength (incomplete screening of the charged silica surface)

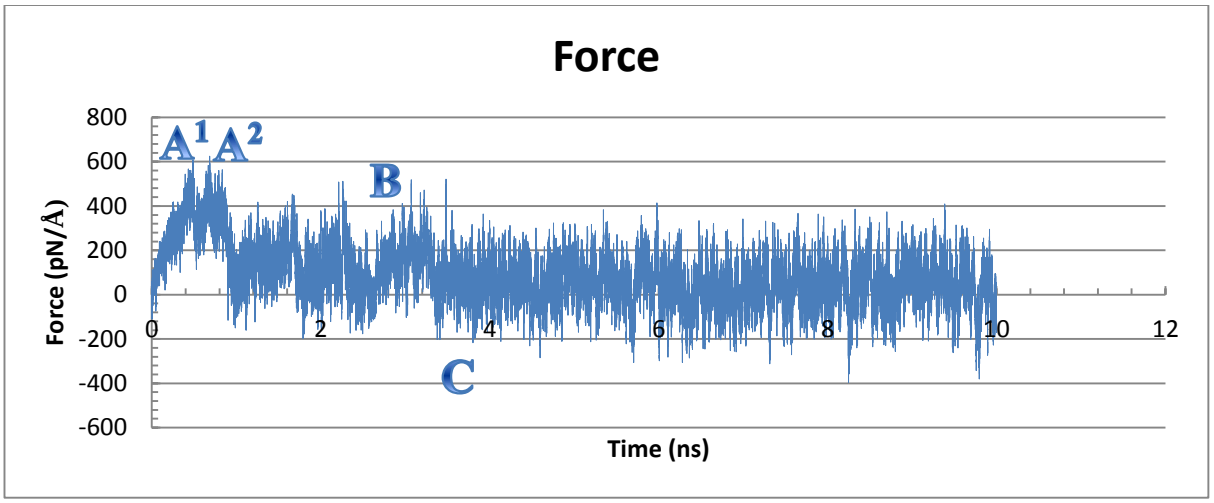

Graph 7: Force against time graph for the SMD trajectory pulling the N-terminal residue of adsorbed cys-GnRH-I in 0.05M ionic strength

After adsorption the glutamic acid N-terminal residue was pulled by the carbon atom (atom number 12) in the +z direction at a rate of 0.005Å/ps for 10ns as per previous SMD simulations. Event A has been distinguished as two events as it comprises of two activation energy peaks in Graph 7, probably due to two residues pulling off from the surface at the beginning of the desorption. Figure 23 illustrates the main events in this simulation.

Events

A^1 – Cysteine residue begins to desorb at 0.88ns → 0.24eV → 0.2eV

A^2 – Cysteine desorbs at 1.04ns → 0.33eV → 0.3eV

B – The peptide desorbs to a 'standing' conformation at 2.9ns → 0.1eV

C – Desorption at 3.5ns → 0.1eV

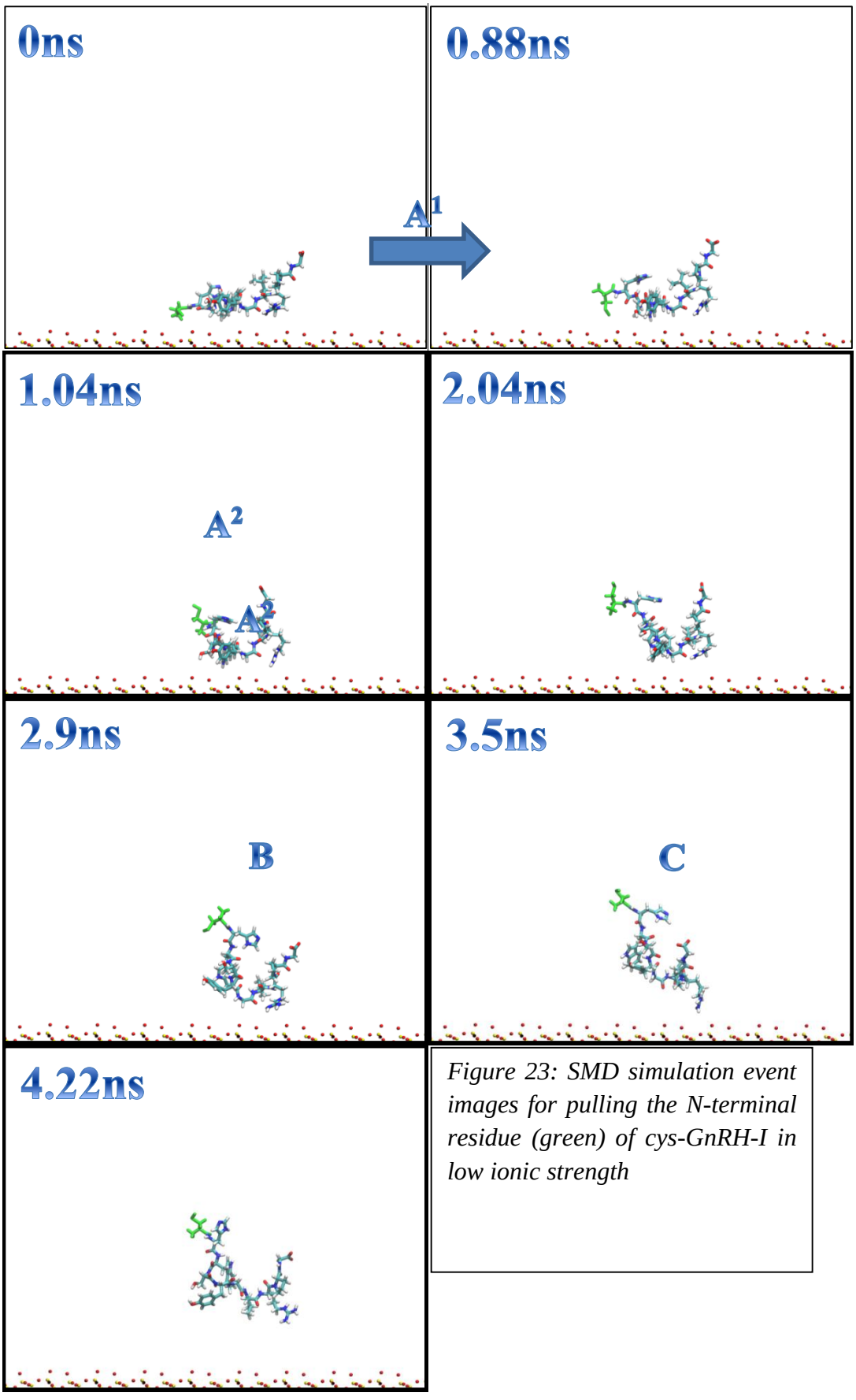

Figure 23: SMD simulation event images for pulling the N-terminal residue (green) of cys-GnRH-I in low ionic strength

Complete Ionic Screening

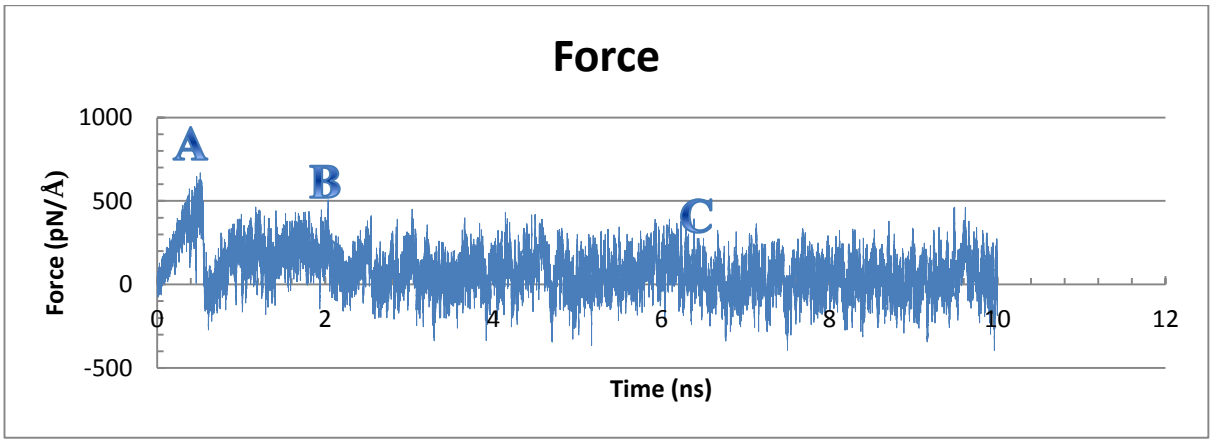

Graph 8: Force against time graph for the SMD trajectory pulling the N-terminal residue of adsorbed cys-GnRH-I in high ionic strength

After adsorption the glutamic acid N-terminal residue was pulled by the alpha carbon atom (atom number 5) in the +z direction at a rate of 0.005Å/ps for 10ns as per previous SMD measurements. This measurement was performed at a high ionic concentration. Figure 24 illustrates the main events in this simulation.

Events

A – Cysteine begins to desorb at 0.64ns→ 0.365eV → 0.4eV

B – Peptide begins to 'stand' on the surface at 2.0ns → 0.115eV →0.1eV

C – Desorption at 6.36ns →0.088eV → 0.1eV

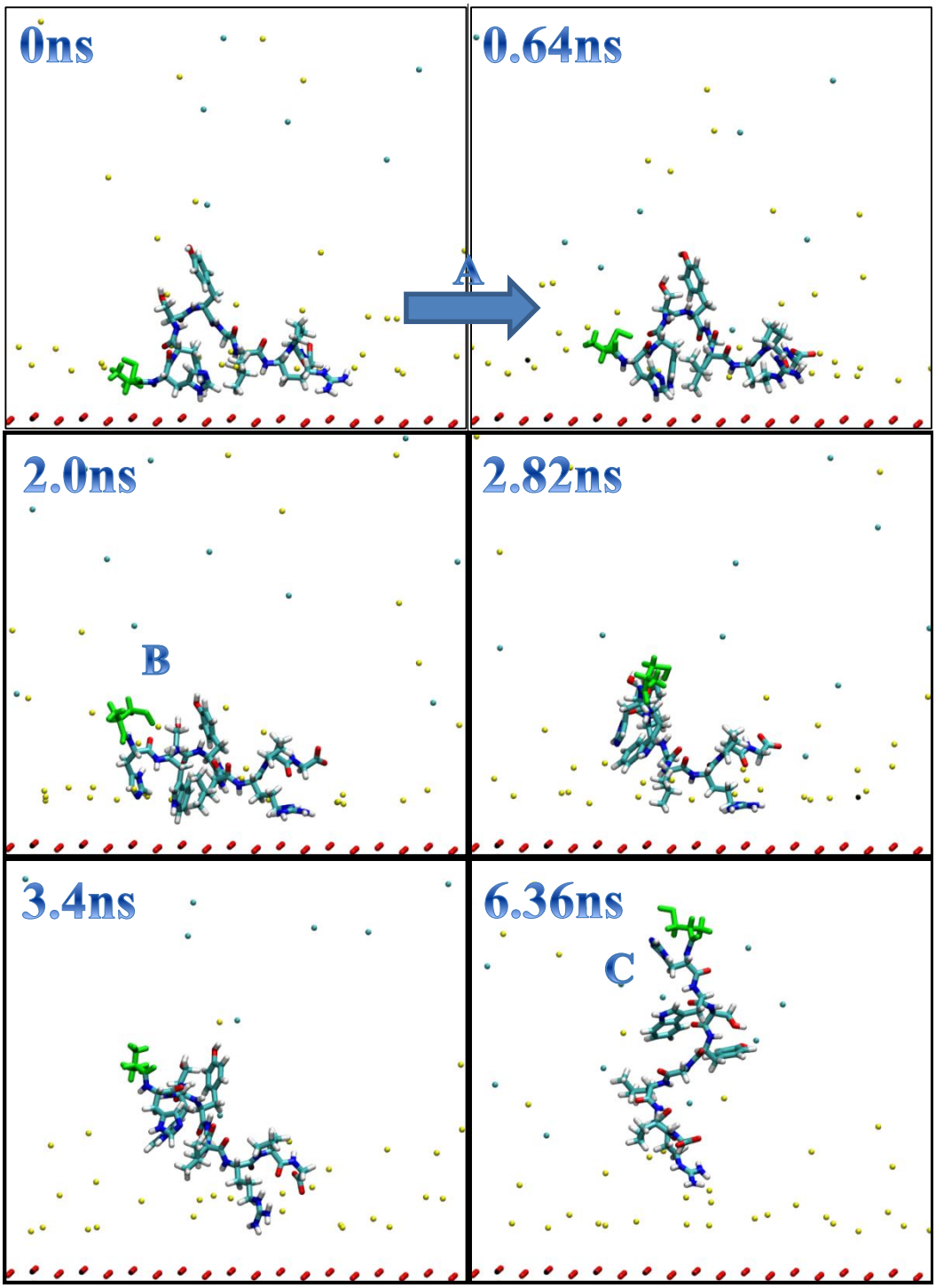

Figure 24: SMD simulation event images for pulling the N-terminal residue (green) of cys-GnRH-I in high ionic strength.

3.4.3 Summary of SMD Results

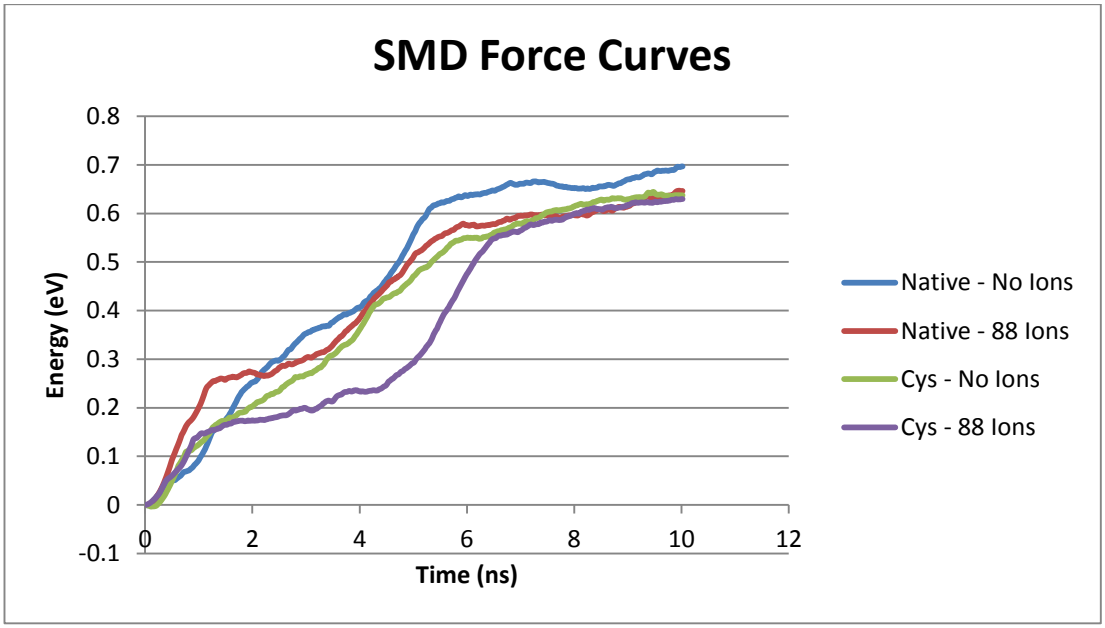

Graph 9: Summary of SMD force curves when pulling the arginine residue.

Graph 9 shows the summary of the force curves for each SMD trajectory when pulling the arginine residue. In each simulation an initial energy barrier (approximately at 1 ns) can be observed that corresponds to the pulled residue being pulled from the surface. Each jump afterwards corresponds to an event in the desorption mechanism (final desorption barrier is overcome between 4 and 6 ns for all curves), which is detailed previously.

3.5 Discussion

In both low and high salt native GnRH-I peptide adsorption studies, the secondary structure of the peptide changes very little. However, when a high ionic concentration is present there is a little unravelling of some of the peptide, but there is a hairpin loop secondary structure present throughout. This may be due to short range ionic interactions between ions and the peptide. However, hydrophobic interactions dictate the peptide structure, not ionic strength. This conclusion can be reached as the peptide does not permanently bind to ions in the bulk solution.

The presence of arginine appears to drive adsorption in both of these systems (arginine adsorbs after 3.4ns in high ionic strength; 9.58ns in low ionic strength), with the entire peptide collapsing on the surface eventually in high ionic strength conditions after 41.4ns (allowing the dipole moment [defined in VMD as generally moving from the C-terminus to N-terminus] to constantly point towards the surface) and staying relatively stable on the surface. Whereas in low ionic strength the leucine residue acts as an anchor (consequently the dipole moment always points in the direction of the surface) from 15.48ns onwards and the peptide does not collapse totally. However, this is not as positionally stable on the surface. Thus it can be remarked that ionic strength does have an effect on the dynamic behaviour of the native peptide as there is a screening effect between the surface and the bulk solvent, which slows down complete adsorption. However, the peptide still adsorbs in a high ionic strength environment, therefore hydrophobicity must play a part in adsorption. A high ionic strength slows down the dynamics, but the end adsorbed state is eventually the same. This ionic screening at the surface is more realistic and

representative of real experimental systems, which have counter ions that are attracted to the surface and screen its charge.

Similarly in both low and high salt cys-GnRH-I peptide adsorption studies, the secondary structure of the peptide is not greatly affected and a hairpin loop is always present throughout. The adsorption of the cys-peptide differed from the native GnRH-I as the positively charged N-terminus (cysteine residue) appears to drive the adsorption (adsorbing at 2.2ns in low ionic strength; 9.87ns in high ionic strength) rather than the positively charged arginine residue. After the initial terminus adsorption, the arginine residue is attracted to the surface (12.98ns in low ionic strength; 11.36ns in high ionic strength) after which the peptide effectively collapses on the surface becoming relatively stable in both cases with the dipole moment pointed towards the surface.

In comparison to the native GnRH-I peptide this peptide adsorbs more readily (i.e. on a faster timescale). The greatest difference is apparent when there is a high ionic strength. The screening layer of ions slows down the complete adsorption of the native peptide considerably (41.4ns), whereas there is not a huge difference with the cys-peptide. This suggests that electrostatic interactions play a major part in peptide adsorption on silica surfaces as the cys-peptide is positively charged and thus can more readily pass through the screening ion and water layer to interact directly with the oxygen atoms on the surface. The native peptide is neutrally charged overall and therefore cannot as easily penetrate the ionic screening layer. However, the native peptide still adsorbs in high ionic strength, which suggests that hydrophobic interactions contribute to peptide adsorption.

Overall, these simulations results suggest that the cys-GnRH-I peptide would have more favourable adsorption to silica, especially in a biological environment than its native counterpart. This is not only because it appears to adsorb more readily, but also because the cys-GnRH-I peptide needs less amino acid 'anchors' on the silica surface, therefore should be more able to interact with the surrounding environment.

As for the GnRH analogues adsorbing to the silica surface, GnRH-II does spontaneously adsorb to the substrate. This is encouraging as it suggests that the GnRH-II peptide, once bound to a nanoparticle surface, would be presented in such a manner to the surrounding environment that it could be a candidate for evoking an immunological response. However, as shown in Figure 14 the peptide adsorbs to the underside of the surface at the top of the simulation box (due to the periodic boundary conditions in place). This side of the silica surface has a predominantly δ-positive charge, whereas silica nanoparticles carry a negative charge. As such, GnRH-II is unlikely to adsorb effectively to silica nanoparticles in experimental studies, but it could be used as a model antigen in other studies that use positively charged nanoparticles.

The other GnRH analogue analysed was GnRH-III. This peptide did adsorb to the silica surface, but took longer to do so than the other GnRH analogues studied. This is probably due to the lack of positively charged arginine in the peptide. There is a positively charged lysine residue present, but this did not appear to drive the interaction between the peptide and the negative surface as efficiently as arginine does on the GnRH-I analogues. As such, the peptide-surface interactions may prove to be too weak for efficient adsorption to occur.

The strength of adsorption of native-GnRH-I and cys-GnRH-I peptides on silica surfaces was investigated using steered molecular dynamics. At the beginning of the SMD study, various pulling rates were investigated. However, 0.005Å/ps was chosen as a larger pulling velocity caused the peptide to desorb from the surface too quickly and to lose its hairpin loop conformation in the process. Thus the pulling rate of 0.005Å/ps was chosen as it made it possible to probe desorption mechanisms on a nanosecond timescale.

For each peptide the N-terminal residue was pulled and the arginine residue was separately pulled (in different simulation trajectories) as these residues were shown to be important in terms of peptide adsorption to the silica surface. In SMD simulations of the native peptide it was found that in solvent with a high ionic strength that 0.37eV was necessary in order for the pulled arginine residue to desorb, whereas only 0.292eV was needed in a low ionic strength environment. The same was also true when pulling the N-terminal glutamic acid residue as 0.145eV were necessary for terminal desorption compared to 0.10eV in a low ionic strength, although the difference is not as pronounced as in the arginine case, most likely because opposing charges were not being pulled apart during the desorption as glutamic acid carries a negative charge.

In the SMD trajectory of the cys-peptide desorption, the arginine desorption energy barrier for differing ionic strengths is closer than that of the native peptide and is actually a little bit less in high ionic strength (0.25eV in high ionic strength and 0.30eV in low ionic strength). These values are very similar, which suggests that the ionicity does not play a large part in the cys-peptide desorption, which could be down to the fact that the peptide is anchored with a neutral residue in the N-terminus,

rather than a negatively charged residue which is present in the native peptide. However, when pulling the N-terminal cysteine residue of the cys-peptide, more energy is once again required in order for desorption to take place at a higher ionic strength of solvent (0.365eV at high salt concentration to 0.24eV at lower concentration).

In all of the SMD simulations, more time is necessary in order to desorb the pulled residue in trajectories with lower ionic strengths. This could be due to the screening effect of the ions, which would be present in the higher ionic strength trajectories. As a result the peptide-surface electrostatic interactions would be stronger in an environment with a lower ionic strength. Furthermore, the energy barrier is higher for full peptide surface desorption at higher ionic strengths as more energy is required to break the ionic screening layer and associated water layer when pulling the peptide. This full screening high ionic strength is physically realistic and the low (incomplete screening) is there for comparison.

All of the events which happened during peptide desorption occurred on a nanosecond timescale, which correlates to the associated Arrhenius rates (Table 2). All desorption trajectories show that the 0.2eV activation barrier is overcome in 10ns simulations. However, the 0.4eV barrier, which correlates to microsecond timescales, cannot be breached spontaneously.

These activation barriers discussed only relate to singular events in the desorption of peptides, when in reality the desorption is somewhat more complicated. Cumulatively, the estimated activation energies of peptide desorption can be found in Table 3. These energies are all above 0.4eV, which explains why spontaneous

desorption is not observed in nanosecond scale simulations. From these cumulative desorption energy barriers it can also be noted that the cys-peptide is bound more strongly than the native peptide, particularly in environments with low ionic strength. This was to be expected, both from the previous adsorption simulations and due to the fact that the cys-peptide is positively charged overall, whereas the native is neutral and therefore will not interact with a negatively charged quite as strongly. However, in a highly ionic environment the effect of the charge on the surface is less pronounced.

Thus the conclusion is that in realistic screening conditions, the singly adsorbed peptides have approximately equal adsorption energies ~0.75 ± 0.15eV. This energy barrier is low enough to correlate with the Arrhenius rate for desorption at nanosecond timescales (Table 2). This suggests that nanoparticles could release these on a 1s timescale, rendering them suitable for drug delivery systems rather than as genuine adjuvants. However, we discuss this further in the following chapters, examining further whether singly adsorbed peptides provide a suitable model.

Table 3: Table of estimated cumulative event energies

Peptide & Residue Pulled	**Low Ionic Strength**	**High Ionic Strength**
Native GnRH-I – Arginine	0.575eV	0.931eV
Native GnRH-I – N-terminus	0.224eV	0.615eV
Cys-GnRH-I – Arginine	0.815eV	0.86eV
Cys-GnRH-I – N-terminus	0.678eV	0.568eV

Chapter 4 – Silica Nanoparticle Synthesis and Peptide Adsorption

4.1 Aims

In order for silica to be useful as an adjuvant in vaccine formulations, it needs to effectively adsorb the associated antigen and in such a way that the antigen is presented to the surrounding environment. The effective adsorption and surface coverage can be measured using various analytical techniques.

The aims of this chapter are to:

- Characterise the size, morphology and effective charge of synthesised Stöber silica nanoparticles.
- Determine the effective adsorption of native GnRH-I and cys-GnRH-I on silica using quartz crystal microbalance and surface plasmon resonance techniques. These experiments were performed at the Jerzy Haber Institute in Krakow, Poland, under the supervision of Dr Barbara Jachimska.
- Investigate how native GnRH-I and cys-GnRH-I peptides behave in monolayered clusters using molecular dynamics simulations.
- Investigate how cys-GnRH-I peptides are presented to the surrounding solvent when bound to BSA using molecular dynamics simulations.

4.2 Materials and Methods

4.2.1 Silica Nanoparticle Synthesis

Spherical silica nanoparticles were prepared using Stöber synthesis. EtOH (Sigma Aldrich Ltd, UK, anhydrous, ≥99.5%) was used as the alcohol in the procedure as higher alcohols have been known to produce larger particle size distributions (Stöber *et al.* 1968). TEOS (Sigma Aldrich Ltd, UK; 99.999% trace metals basis) and ammonium hydroxide (Sigma Aldrich Ltd, UK; ≥99.98%) were also used as the initial reactants for this synthesis. A peristaltic pump was used to control the addition rate of the TEOS/EtOH mixture. Various sizes of silica nanoparticles were prepared, but nanoparticles of ~200nm were used in this study as particles which are smaller are more likely to have cytotoxic effects (Mody *et al.* 2013). The size of Stöber silica nanoparticles can be tuned by altering the ratio of TEOS to ammonium hydroxide. In order to synthesise particles of 200nm, 2.16mL of a 2 molar ammonium hydroxide solution was added to a 22.3% (v/v) TEOS solution made up with EtOH and the rest of the Stöber method followed.

The resulting silica nanoparticles were analysed using DLS measurements, zeta potential measurements and scanning electron microscopy (SEM). All product was stored in a suspension of 50:50 ethanol:deionised water for 3 months at room temperature at a silica concentration of 0.2g/L. Product was analysed by DLS to make sure that aggregation had not occurred.

4.2.2 Protein-Peptide Conjugation

1-Ethyl-3-(3-dimethylaminopropyl) carbodiimide (EDC) (Sigma Aldrich Ltd, UK) enabled the conjugation of GnRH–I and its analogues to carrier proteins BSA (fraction V, ≥96%) and OVA (both purchased from Sigma Aldrich Ltd, UK). EDC linked the peptide to the carrier protein via a hydrolysis reaction between an amine group and a carboxylic acid group. BSA and OVA complexes were used for immunisation studies and as coating for ELISA studies respectively.

Each peptide and carrier protein was conjugated in a 1:1 weight ratio using the EDC reaction (Gebril *et al.* 2014) and separated using 30K Merck Millipore centrifugal units.

4.2.3 Dynamic Light Scattering (DLS)

The size of silica nanoparticles were determined by DLS measurements using a Malvern zetasizer Nano ZS with a measurement range spanning from 0.6nm to 6µm. Non-invasive backscattering optics were used in this instrument. Samples were measured at silica concentrations varying from 200ppm to 1500ppm (diluted from sample in section 4.2.1), diluted with NaCl salt solution at ionic strengths ranging from $1x10^{-3}$M to $1x10^{-2}$M. The effect of pH was also investigated on the dynamic behaviour of the particles, as a range from pH 2 to pH 10 was used in these studies – pH levels were altered using hydrochloric acid or sodium hydroxide. Each measurement was carried out three times and the average result was taken.

4.2.4 Scanning Electron Microscopy (SEM)

Images of silica nanoparticles were taken by SEM using a JEOL JSM-3700F field emission SEM at an operating voltage of 15keV. This work was undertaken under the supervision of Dr Barbara Jachimska at the Jerzy Haber Institute in Krakow, Poland.

SEM is a characterisation technique that produces images at the nanoscale of a sample by scanning the sample with a focussed beam of electrons. The secondary electrons emitted by the atoms excited by the incident electron beam are detected and combined with the scanned electron beam to produce an image of the topography of the sample (Atkins, 2006).

In order to take SEM images of the Stober nanoparticles, a small amount of the silica suspension had to be dried on a support. Upon drying, the silica nanoparticles were more likely to aggregate. Therefore, this was not the ideal condition in which to take images of the silica, but a 'wet' method of SEM was not available so the investigation proceeded with a dry sample.

4.2.5 Zeta Potential

The zeta potential measurements were performed using a Malvern Zetasizer Nano ZS. This equipment utilises the laser Doppler velocimetry (LDV) technique. The sample solution was placed in a standard cell with opposing palladium electrodes and the velocity of charged particles to their opposing electrodes was measured and expressed as electrophoretic mobility. Consequently the zeta potential was calculated.

The zeta potential was measured at an ionic strength regulated by sodium chloride salt addition up to 1 x 10^{-2}M over a range of pH values to ascertain the isoelectric point (the pH at which the particle becomes uncharged) of the silica.

4.2.6 Quartz Crystal Microbalance (QCM)

QCM studies were performed using a silica coated disc and the amount of peptide (GnRH-I [Genosphere Biotech, France, >95%] or cys-GnRH-I [Immune Systems Ltd, UK, >95%]) or peptide-BSA conjugate adsorbed was observed. The QCM measurements were performed by allowing a peptide (concentration ranged from 5ppm to 50ppm), or peptide-BSA conjugate, solution to flow over the silica disc for 90 min. These measurements were made over a varied pH range and at an ionic strength I=1 x 10^{-3}M. The QCM sensor was then rinsed with a NaCl solution (I=1 x 10^{-3}M) for 90 min to investigate the reversibility of adsorption.

The QCM measurements were performed using a Q-sense E4 instrument (Vastra Frolunda, Sweden).

4.2.7 Surface Plasmon Resonance

A MP-SPR Navi 200 model (BioNavis Ltd, Finland) was used to perform SPR measurements. This is a prism-coupling based device (Krechmer mode) which uses two independent channels and a peristaltic pump. The apparatus has a wide angular scan range (between 40°-78°) at a wavelength of either 670nm or 785nm. A silica sensor was used to measure the adsorption of each GnRH peptide and the GnRH peptide-BSA complex on a silica surface. The parameters of this sensor were found

using the SPR Navi Data Viewer program – Bionavis Winspall 3.02 software. At wavelengths of 670nm and 785nm the k x d (layer thickness) values were 1.0 x 10^{-7}nmdeg^{-1} and 1.9 x 10^{-7}nmdeg^{-1} respectively. For the peptide solution the $\frac{dn}{dc}$ (refractive index) value was 0.181cm^{3}g^{-1} and the BSA-peptide complex had a $\frac{dn}{dc}$ value of 0.137cm^{3}g^{-1}.

Adsorption of the GnRH peptides and GnRH-BSA complexes were monitored using the measured changes in resonance angle, with the adsorbed surface mass per cm^2 (Γ_{SPR}) calculated as a function of time using the equation given above. The SPR measurements were performed by allowing a peptide (concentration = 5ppm), or peptide-BSA conjugate (5ppm), solution to flow over the silica disc for 90 min. These measurements were made over a varied pH range and at an ionic strength I=1 x10^{-3}M. The SPR sensor was then rinsed with a NaCl solution (I=1 x 10^{-3}M) for 90 min to investigate the reversibility of adsorption.

4.2.8 Molecular Dynamics Simulations of Peptide Clusters

For both native and cys-GnRH-I cluster simulations the same software and CHARMM27 forcefield parameters were used as per previous simulations (section 3.2.1) and were analysed as before using VMD.

Both simulations were prepared by taking the atomic coordinated of each individual peptide from an adsorbed ‘standing’ state from section 3.3. This peptide was then copied and transposed in all directions from the original peptide to create a silica slab with 9 adsorbed peptides (Figure 25). Each peptide was carefully placed in

order to make sure that the van der Waals boundaries of each peptide did not overlap with each other.

The systems were neutralised with NaCl atoms and made up to 88 Na and Cl ions in order to simulate a highly ionic environment. The system was solvated with TIP3P water molecules. Simulations were run for 50ns at 310K (body temperature) and contained approximately 50,000 atoms. The systems were then setup with equilibration and heating steps as per previous simulations (section 3.2). An SMD simulation was run on the cys-peptide cluster from the end-point of the initial cluster simulation. One peptide was pulled by the N-terminus (cysteine residue) in the +z direction (away from the surface) at 0.005Å/ps (as per section 3.2.2).

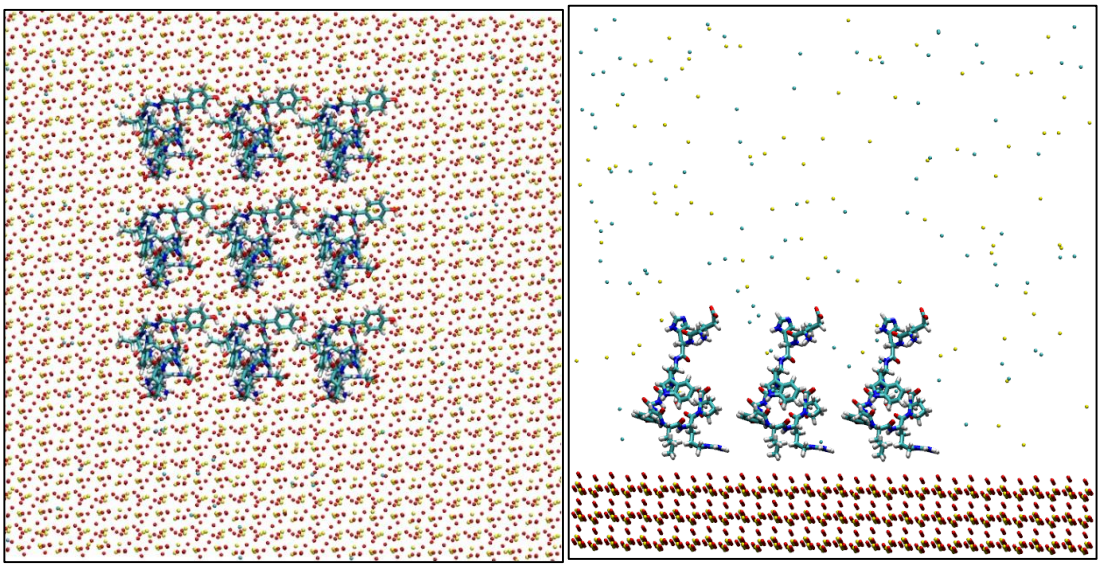

Figure 25: Top view and side view of the native peptide cluster starting positions

4.2.9 Molecular Dynamics Simulations of BSA-Peptide Complex

All previous simulations software and parameters were used in the preparation and running of the simulation with a BSA monomer with two cys-GnRH-I peptides chemically bonded. The BSA monomer 3VO3.pdb was taken from the protein data bank (Majorek *et al.*, 2012) and isolated.

The simulation was prepared by running a trajectory with 12 cys-GnRH-I peptides in various positions around a BSA monomer in a TIP3P water solvent. This allowed the optimal locations for peptide interaction with BSA. Two locations were chosen and one peptide was chemically bound in each position as if an EDC hydrolysis reaction had taken place. The positions of binding were at opposite termini in order to investigate the effect of binding site. The BSA-peptide complex was prepared by Dr Karina Kubiak-Ossowska and subsequently used in this study.

The simulation box was neutralised and made up to a concentration of 0.05M NaCl salt. The system was then solvated as in previous simulations and the final simulation contained approximately 180,000 atoms and was run at 310K for 5ns. The system was setup with equilibration and heating steps as per previous simulations (section 3.2.1).

4.3 Results

4.3.1 Dynamic Light Scattering

Stöber silica nanoparticles were measured using DLS measurements. The average size was found to be approximately 190nm:

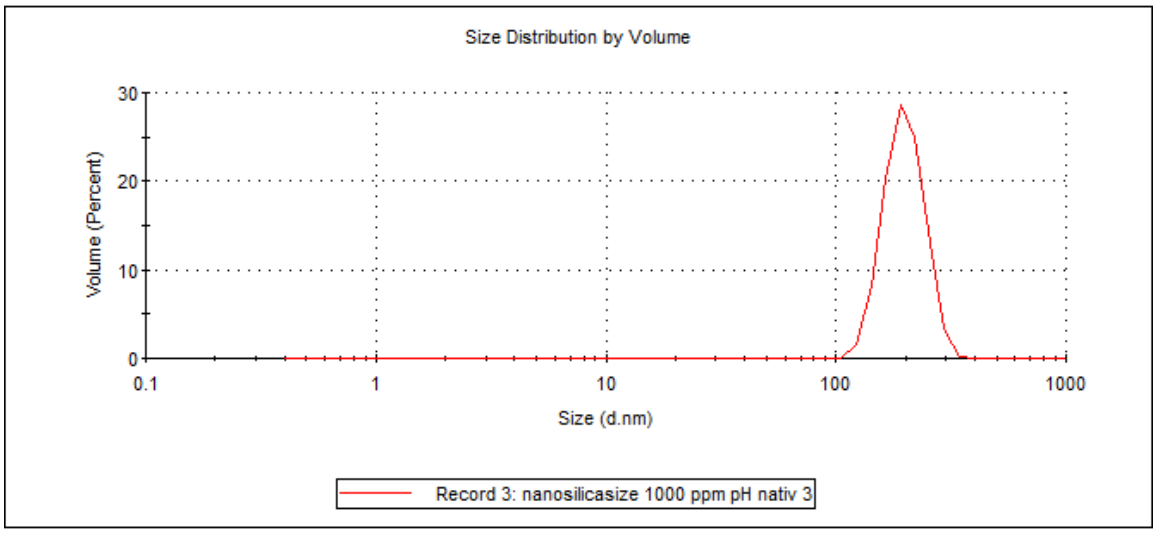

Graph 10: Size distribution of Stober silica at 1000ppm

These DLS measurements were carried out in various conditions to investigate the effect of silica concentration and ionic strength on the size of the Stöber spheres. The size distribution curve shown in Graph 10 shows that the average size of silica nanospheres is 195.8nm, with a polydispersity index (PDI) of 0.056. Such a low PDI indicates that these particles are of a monodisperse nature.

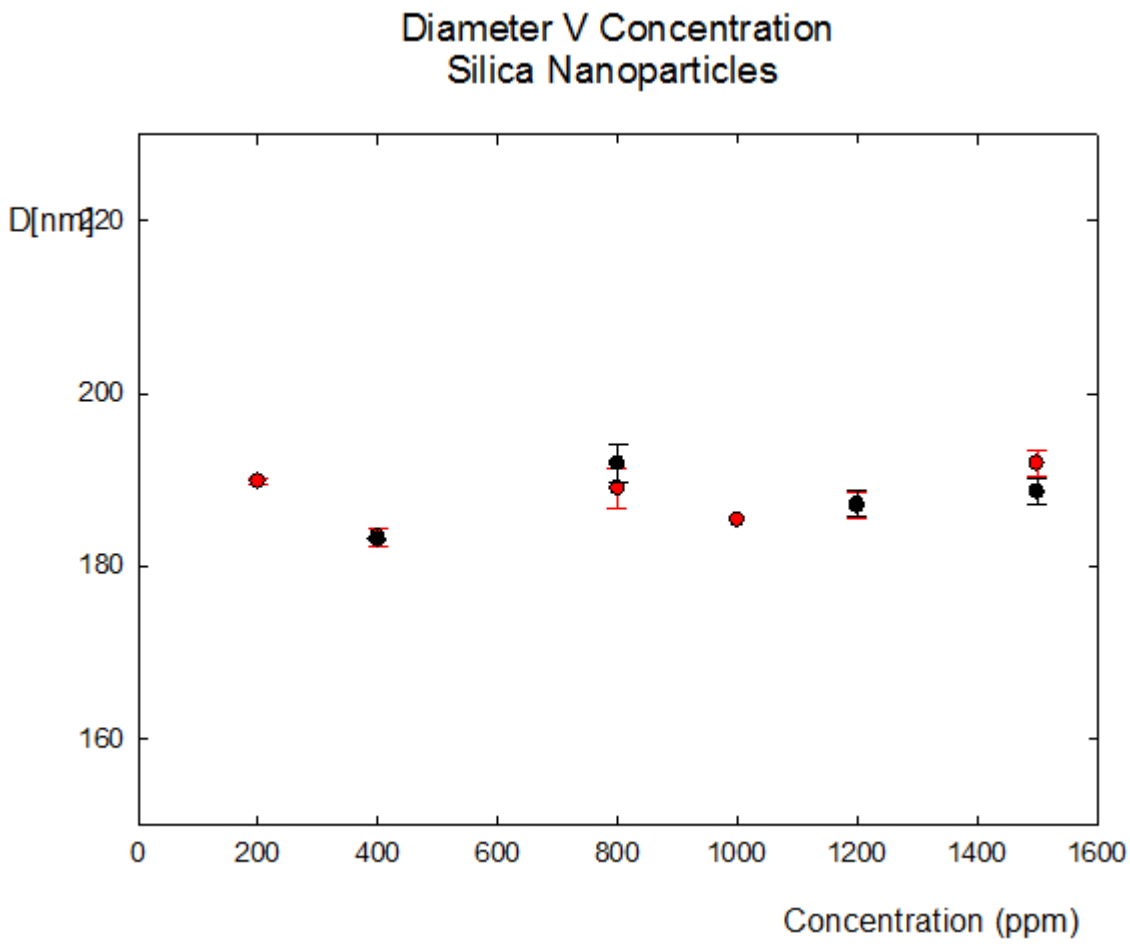

Graph 11: Size of Stober spheres of varying concentrations of nanoparticles

As can be observed in Graph 11, the concentration of silica used in the DLS measurements does not seem to affect the size of the nanospheres too greatly. The size tends to hover around 190nm without a discernible pattern with increasing concentration.

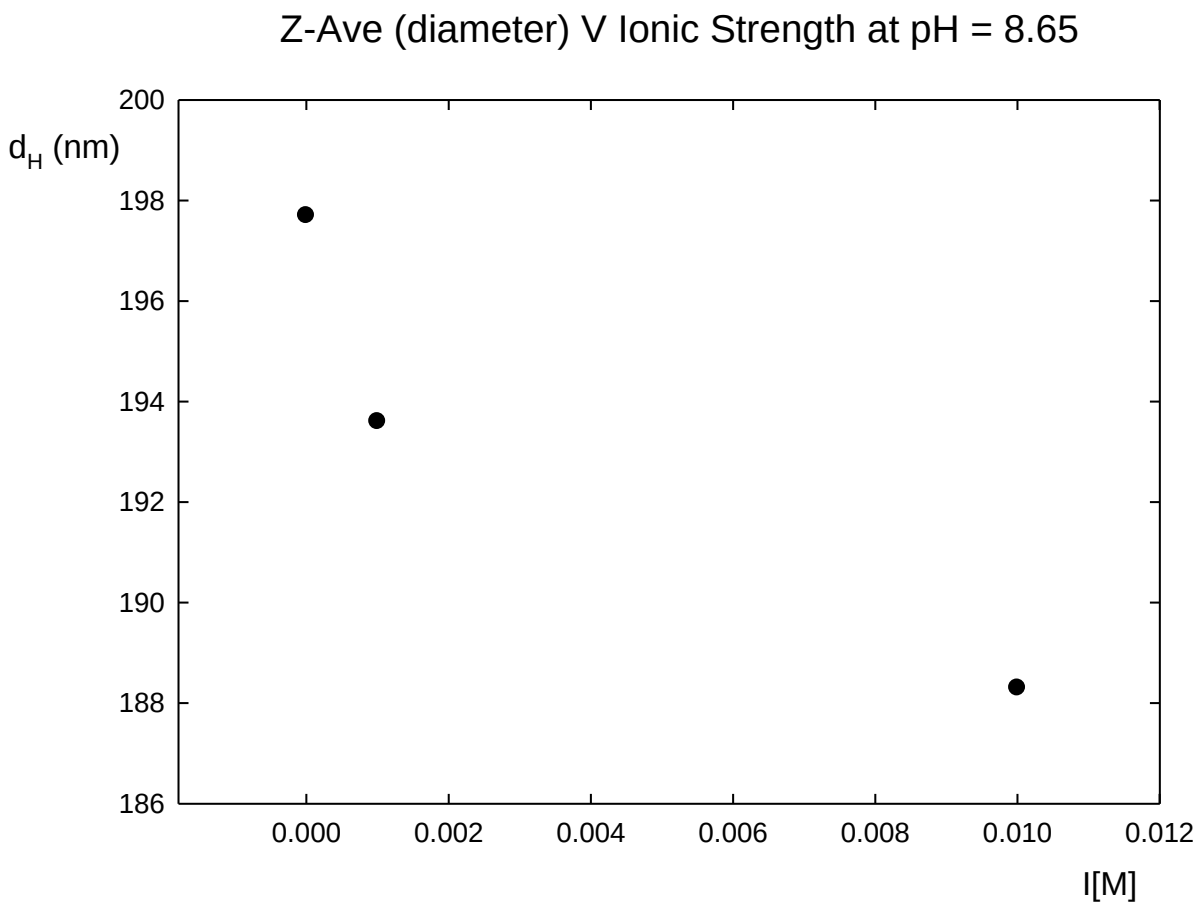

Graph 12: Size of Silica Nanospheres with Varying Ionic strengths

Graph 12 shows how the sizes of silica nanospheres change with ionic strength. DLS measurements were performed using 1000ppm of Stober in different concentrations of NaCl solutions (ionic strength of 0.00 is silica in deionised water). It can be observed that the size of silica nanospheres decreases with increasing ionic strength. However, this effect is small (n.b. the scale on the y-axis Graph 12). This may be a result of swelling effects of silica as ionic strength decreases. However, another measurement at an ionic strength of 0.15M NaCl was also taken. This gave results of 192.0nm sized silica spheres with a PDI of 0.069. As such, a larger range of ionic strengths should be investigated to fully understand the effect of ionic strength on the

size of silica nanoparticles, but it appears that any effects are relatively modest in size.

It was found that the nanoparticles aggregated when close to the isoelectric point (~pH 3.0) to sizes of over 1,000nm. This behaviour was not unusual as the change in charge of the particles would cause aggregation, thus the solution would become polydisperse.

4.3.2 Zeta Potential

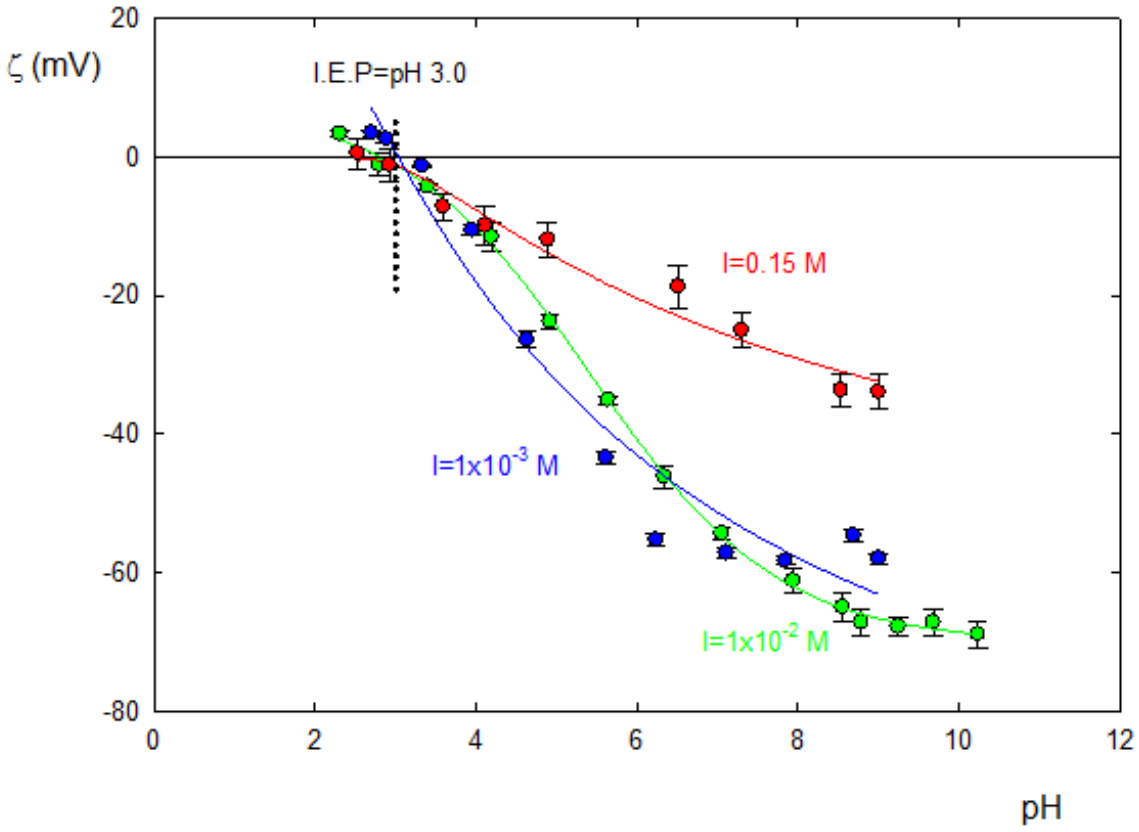

Graph 13: Comparison of zeta potential of silica at varying ionic strengths of electrolyte solution (1000ppm silica)

Zeta potential measurements were carried out on Stober silica nanoparticles in conjunction with DLS measurements. The zeta potential and mobility of the particles were measured in varying ionic strengths and pH conditions. It was found that the isoelectric point of the Stober particles was around pH 3.0 (as seen in Graph 13).

It was found that the ionic strength of the NaCl solution affected the zeta potential of the silica particles – with a higher ionic strength being associated with a lower charge on the particles due to counter-ions adsorbing on the particle surface reducing the zeta-potential. Morga *et al.* (2016) found a similar trend with zeta potential of mica in increasing ionic strengths.

4.3.3 Scanning Electron Microscopy

Figure 26 shows a SEM image of the silica nanoparticles manufactured in this study, indicating that they are approximately spherical with a diameter ~200nm and good homogeneity. The DLS measurements confirmed this, finding a mean diameter of 193nm at pH 8.7 (polydispersity index, PDI, of 0.079) to 199nm at pH 4.0 (PDI of 0.09). It was observed in DLS studies that the particles swelled in size with decreasing pH and below the isoelectric point (approximately pH 3.0) the particle size greatly increased (to 1210nm at pH 2.9), indicating the formation of aggregates.

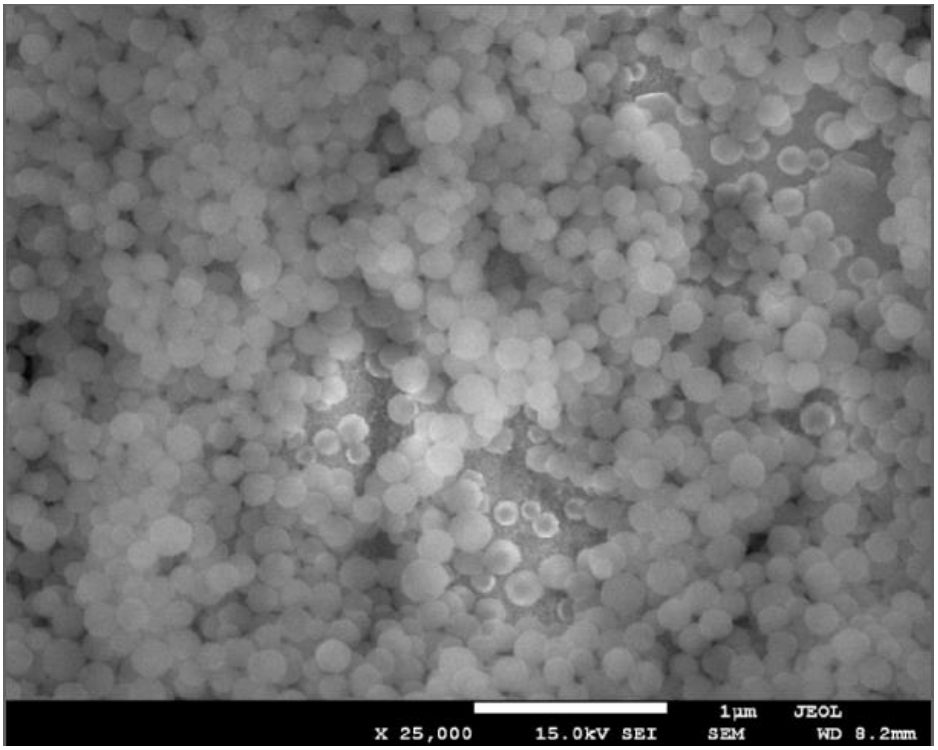

Figure 26: SEM image of spherical silica nanoparticles

4.3.4 Peptide Adsorption

4.3.5 Quartz Crystal Microbalance (QCM)

QCM studies were undertaken to investigate how the native and cys-GnRH peptides adsorbed to a silica surface. BSA-peptide complexes were also included in this study.

4.3.6 Native Peptide

The native GnRH-I peptide has a molecular weight of 1311.42g/mol with an isoelectric point at pH 8. Overall it has a neutral charge at pH 7, but does include some charged residues (Arg [+ve], Glu [-ve]).

The adsorption of native GnRH on a silica surface was investigated by using a silica sensor in the QCM apparatus. All QCM measurements were carried out using a $1x10^{-3}$M NaCl solution as an electrolyte medium and with a peptide concentration ranging from 5 to 25ppm. All measurements were also performed with a 90 min adsorption period followed by a rinsing period of 90 min.

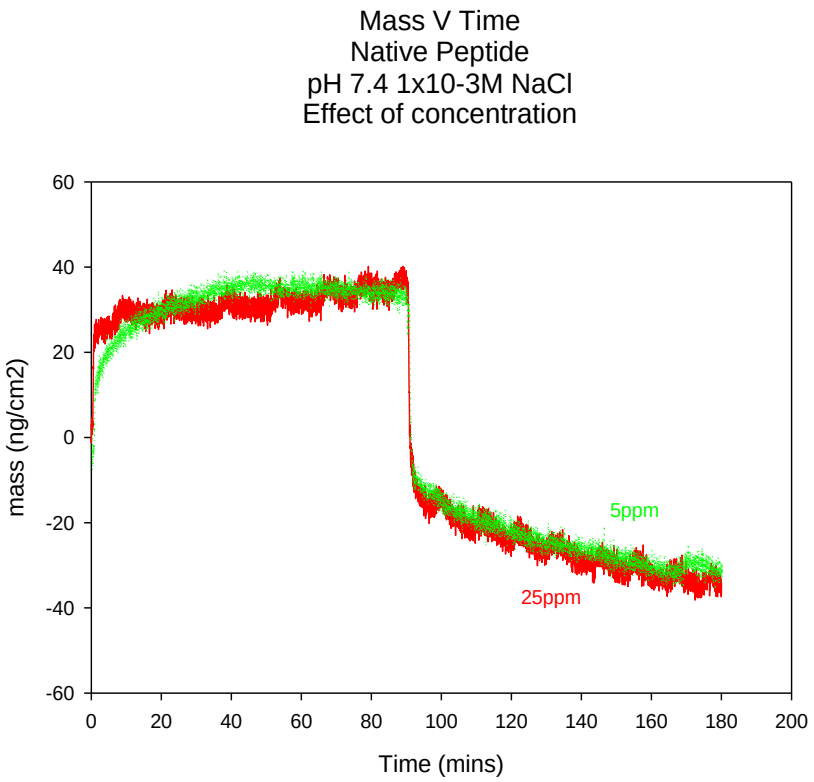

Graph 14: Effect of native peptide concentration on silica surface adsorption. A rinsing step was carried out at 90 min.

Graph 14 shows that a saturated surface coverage of native GnRH peptide is reached at a concentration of 5ppm (or possibly even less). This is shown as there is no extra adsorption with an increase in concentration to 25ppm of the peptide. Graph 14 also suggests that the peptide adsorption is reversible as the mass adsorbed is reduced to a negligible amount at the rinsing step. Consequently, subsequent native peptide adsorption QCM studies were all undertaken with a peptide concentration of 5ppm. This was advantageous as only a small amount of the native peptide was available due to its high cost.

The waves that are apparent in the measurement at 25ppm concentration occur due to the pumping of fluid over the sensor by the peristaltic pump. It was also observed that after the rinsing step the adsorbed mass dropped below 0 ng/cm^2, this may be down to a change in pH levels between the peptide solution and the rinsing solution.

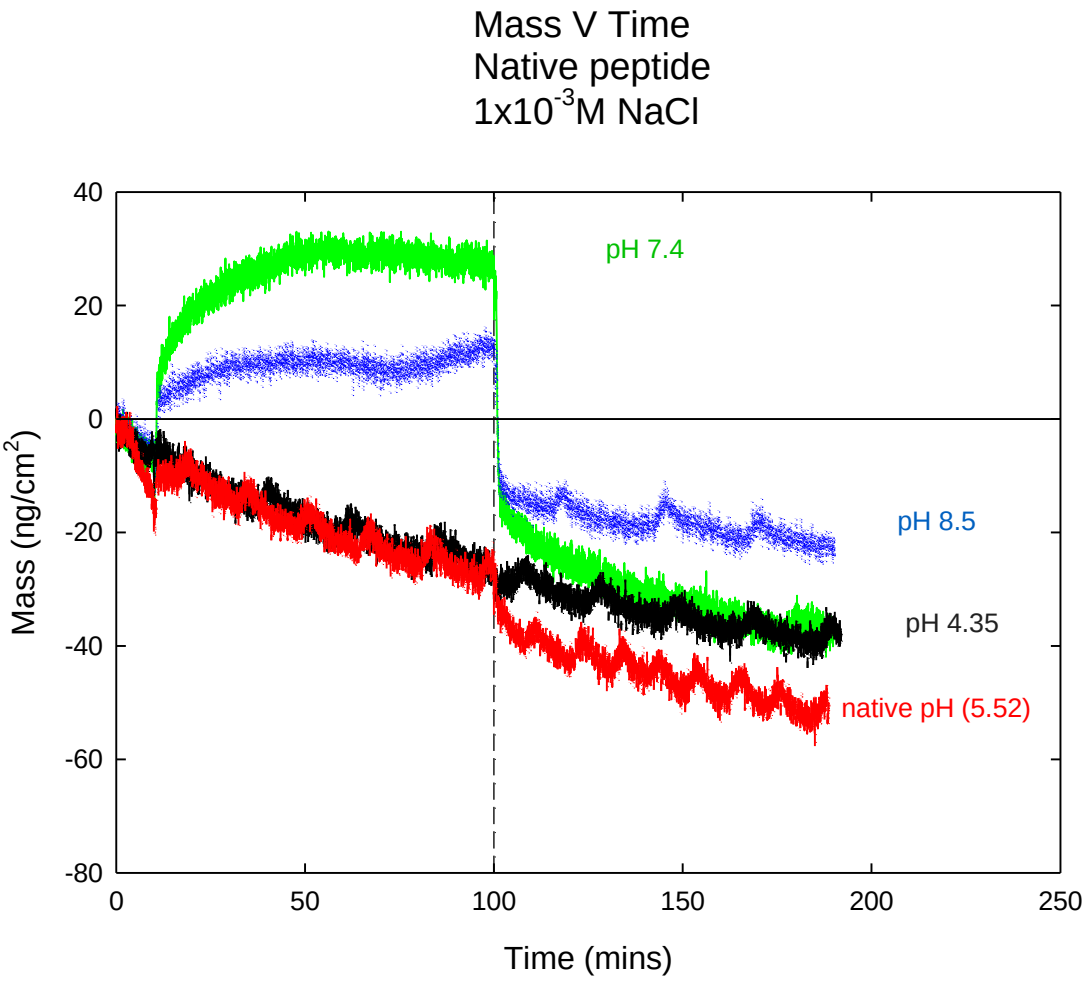

Graph 15: Effect of pH on native peptide adsorption on a silica sensor

The effect of pH on the adsorption of native GnRH was investigated. Graph 15 shows that at measured pH levels lower than 7, the peptide does not adsorb to the silica surface. The peptide appears to have maximum adsorption at around neutral pH (7.4), with reduced adsorption at a higher pH of 8.5. This could be due to changing

charges on the peptide with varying pH (Voievoda *et al.*, 2015). The adsorbed mass is calculated using the Sauerbrey equation (Chapter 2, section 2.2.5). These results are echoed in Graph 16, which shows the thickness of the adsorbed layer. It is also apparent that the adsorption of native GnRH is reversible regardless of the pH of the conditions.

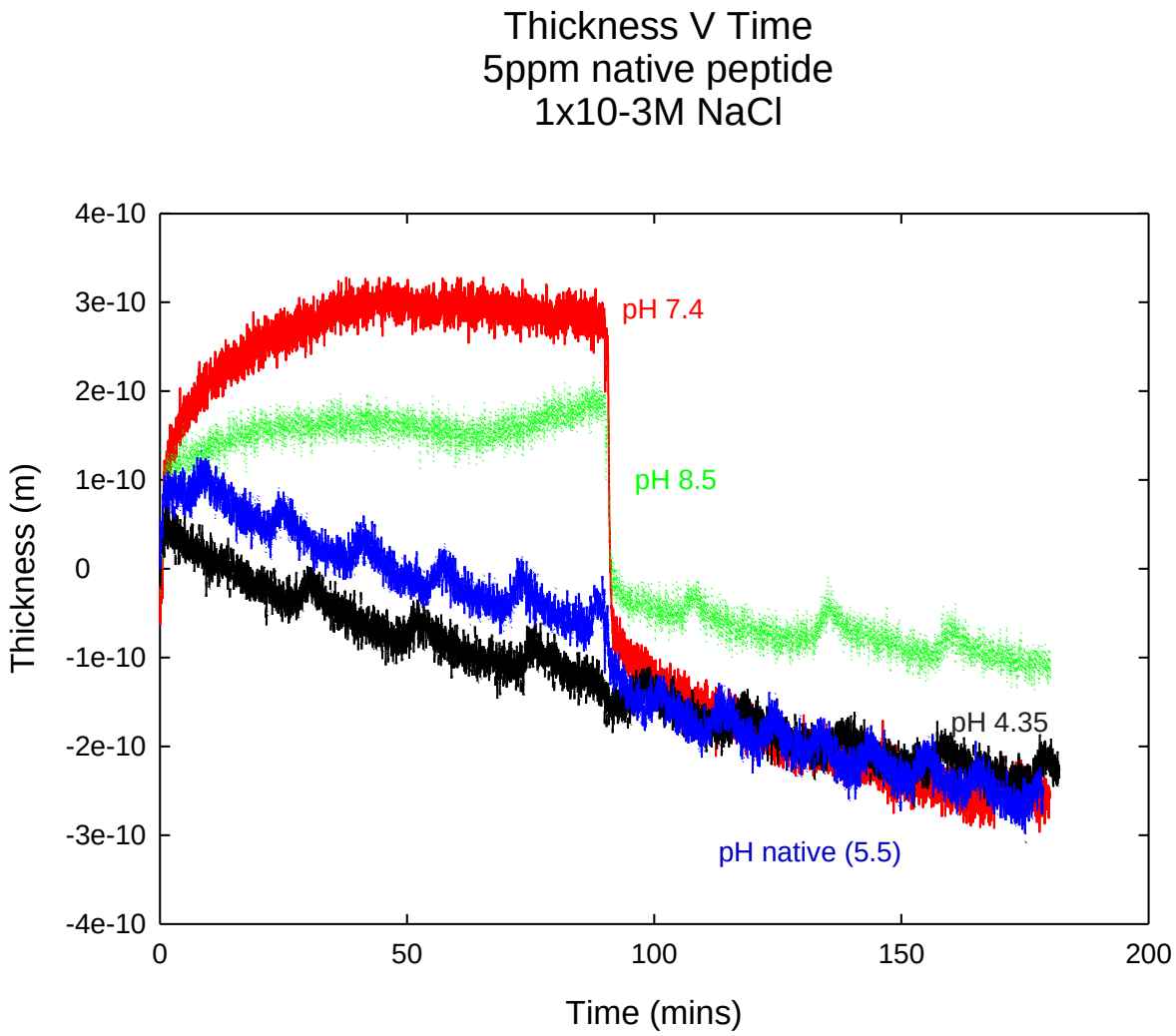

Graph 16: Effect of pH on the thickness of the adsorbed native GnRH layer.

4.3.7 Cys Peptide

The cys-GnRH-I peptide has a molecular weight of 1216.39g/mol with an isoelectric point at pH 9.16. Overall it has a charge of +1 at pH 7. This is due to the presence of one charged residue (arginine). As such, it may be more likely to be attracted to negatively charged particles and surfaces – i.e. the Stöber silica surface the zeta potential of which has been found to be negative.

Adsorption studies of the mutated (cys) GnRH peptide were undertaken using mainly silica surfaces, but a gold surface was also used for contrast. Each QCM measurement was completed using an electrolyte solution of $1x10^{-3}$M NaCl. An electrolyte solution of $1x10^{-2}$M NaCl was also used. As with the native peptide, each measurement was allowed 90 minutes for adsorption and 90 minutes for rinsing.

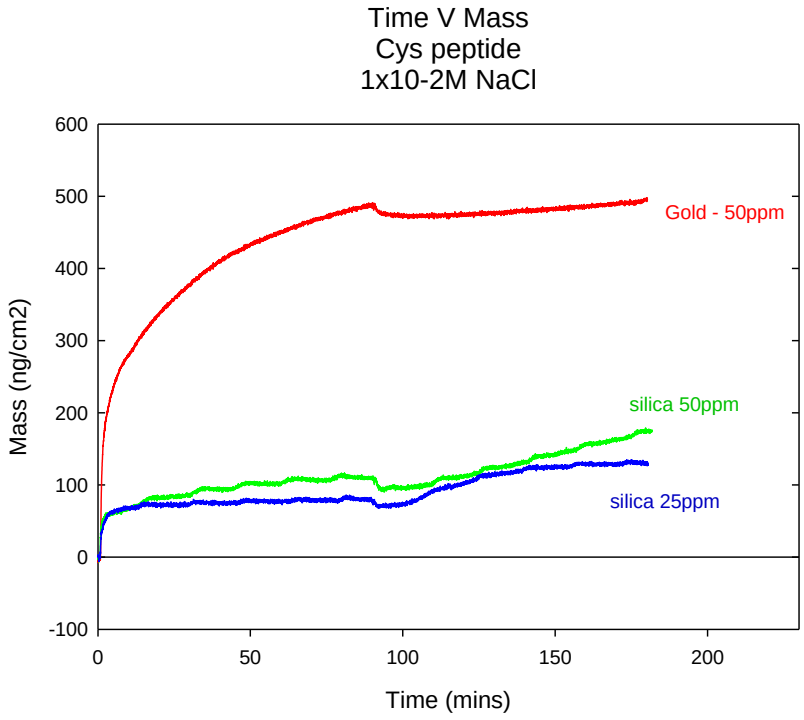

Graph 17: Effect of Cys-peptide concentration on silica surface adsorption and the effect of sensor choice on adsorption. Rinsing step after 90 mins.

Graph 17 shows that, at neutral pH, a peptide concentration of 25ppm allows maximum adsorption onto a silica surface and that increasing the concentration to 50ppm does not have a great effect on the adsorption of the peptide. It can also be observed that there is a higher degree of irreversible adsorption of the cys peptide. This is advantageous in the synthesis of peptide-functionalised silica nanoparticles as it suggests that the peptide will stay adhered to the silica surface *in-vivo* (these experiments were carried out at pH 7.4 – the same as that of the bloodstream).

From Graph 17 it can also be seen that the mutated peptide adsorbs much more effectively to the gold surface. From this result it could be argued that gold could be used as a useful carrier particle for peptides. However, for the purposes of this work it may prove ineffective as the binding might be too strong to allow the secondary structure of the adsorbed peptide to interact with the surrounding environment *in-vivo*. Also, 'bare' gold nanoparticles aggregate in solution, unlike silica nanoparticles, so would not provide a good vehicle for drug delivery and vaccines.

A study into the effect of pH levels on the adsorption of the cys-peptide onto a silica sensor was also carried out:

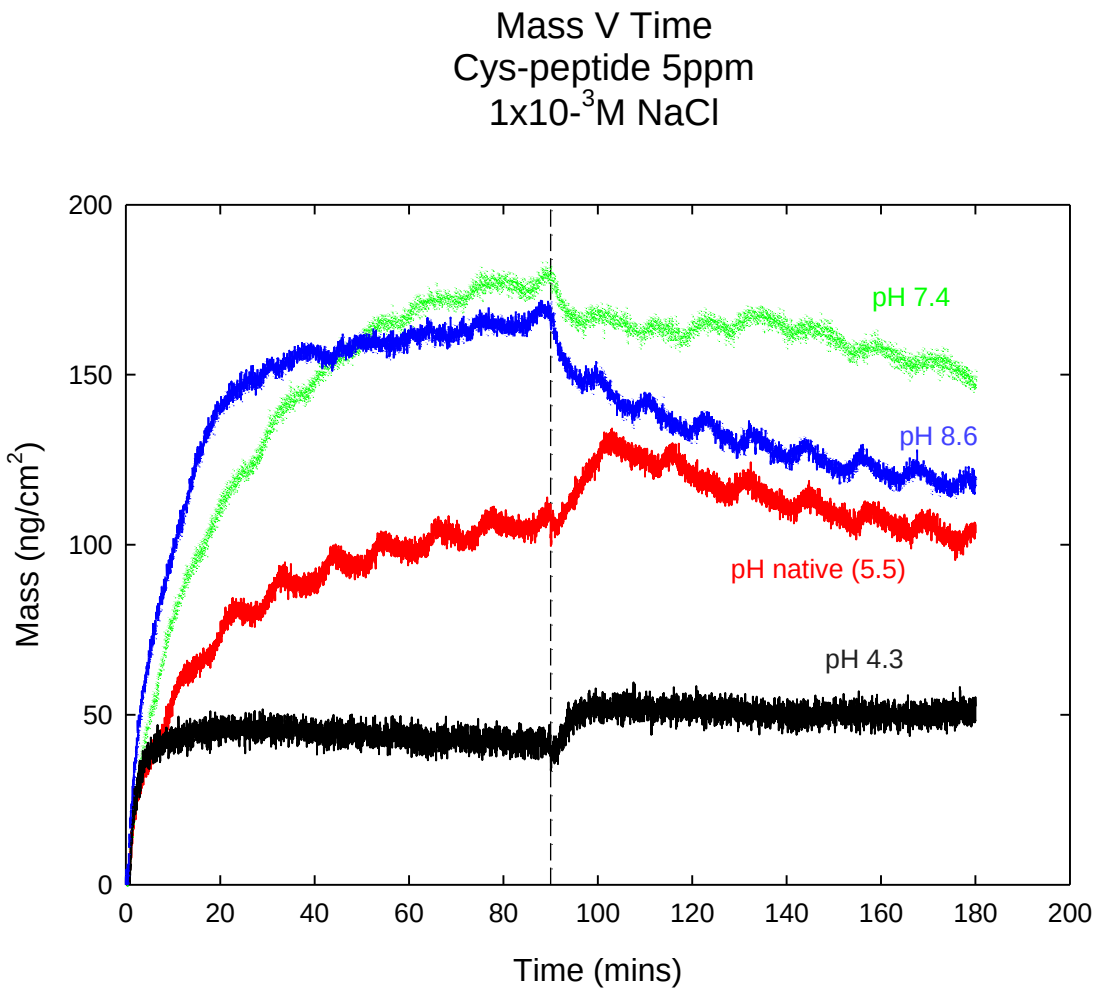

Graph 18: Comparison of cys-peptide adsorption levels at various pH levels on a silica surface

Similar to the results shown for the native peptide (Graph 15), Graph 18 shows that the peptide adsorbs most effectively at a neutral pH level of 7.4. However, adsorption of the cys-peptide appears to happen at all pH levels investigated, which is not apparent with the native peptide. Graph 18 also reiterates that the cys peptide allows irreversible adsorption on silica to a degree at all pH levels measured. This suggests that the cys peptide may be better suited for use in *in-vivo* experiments.

In some cases the adsorbed mass appears to increase upon rinsing. This is most likely due to a sudden change in pH over the QCM sensor. This effect was kept to a minimum by carefully controlling the pH of solutions used, but pH control proved to be difficult.

4.3.8 Comparison of Peptides

Graph 19 clearly shows that the cys-peptide adsorbs to a much greater degree than the native GnRH peptide at pH 7.4. At maximum adsorption, the cys peptide has approximately six times the amount of mass adsorbed that the native peptide has. It can also be clearly observed that, although there is some desorption of the cys-peptide, there is a high degree of irreversible adsorption, whereas the native peptide exhibits completely reversible adsorption to the silica surface. This desorption is also much more rapid for the native peptide, probably due to the poor electrostatic interactions between the peptide and the silica sensor.

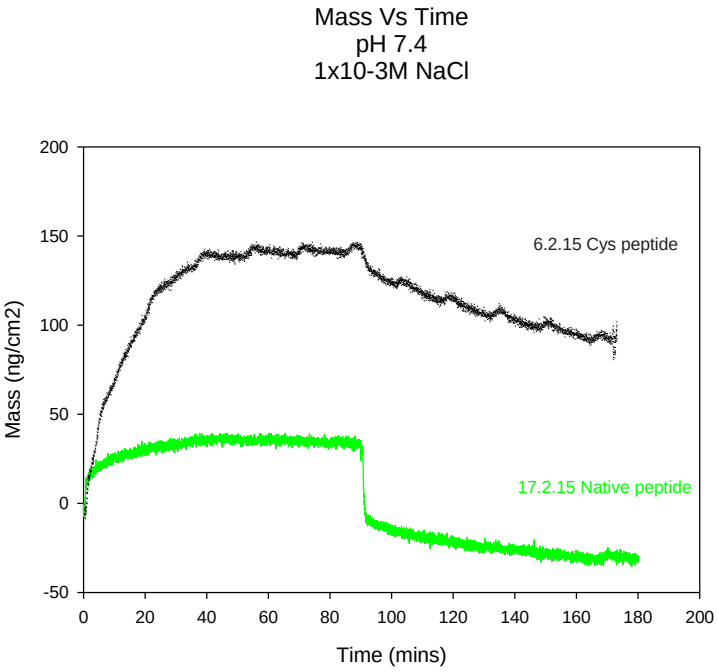

Graph 19: Comparison of peptide adsorption on a silica surface. The y-axis denotes the mass adsorbed on the silica sensor.

Graph 20 shows that the cys-peptide is able to bind to the silica surface at all pH levels, but most effectively at a near-neutral pH of 7.4, whereas at lower pH levels, the native GnRH-I peptide fails to adsorb.

It can be surmised from this data that a pH level of 7.4 lends itself to the most effective binding of either peptide on a silica surface. This is advantageous as 7.4 is physiological pH.

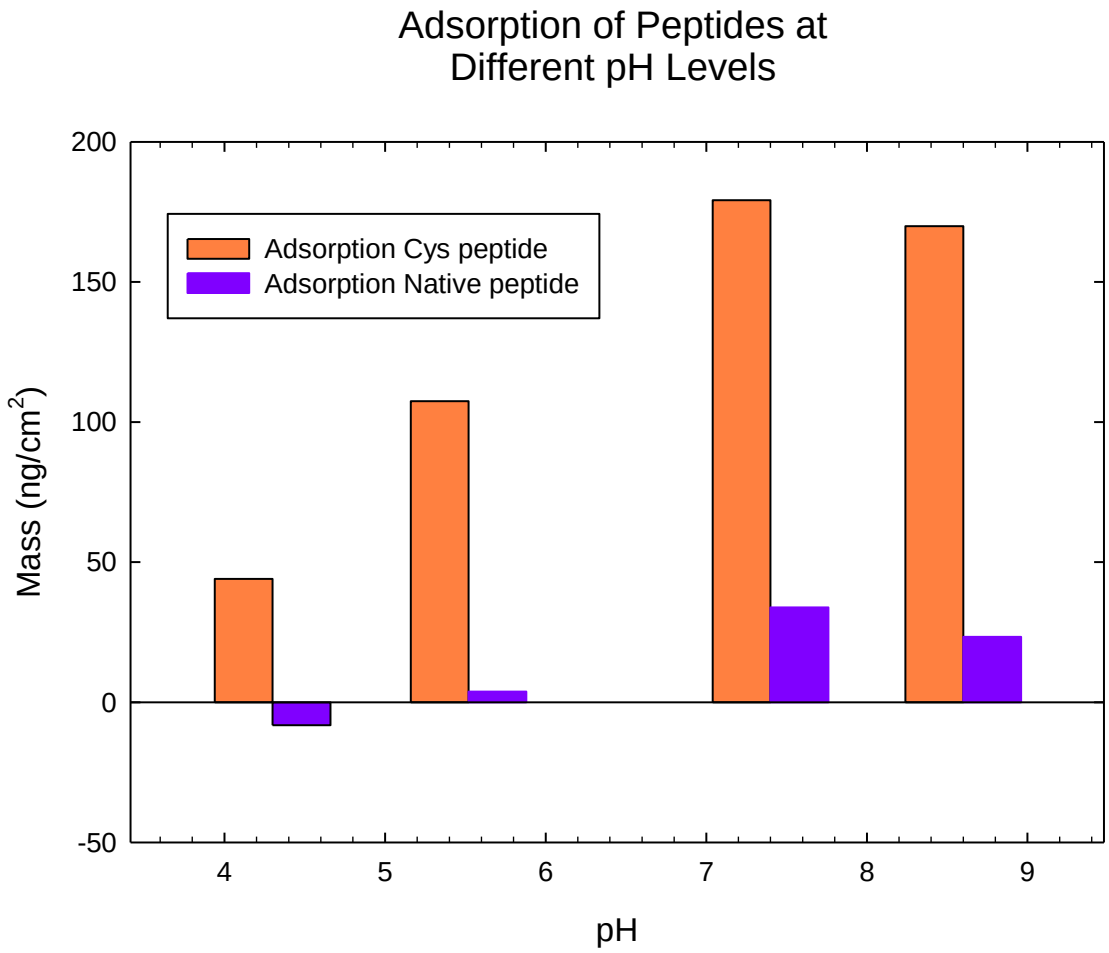

Graph 20: Comparison of reversible peptide adsorption at varying pH levels

4.3.9 BSA-Peptide Complexes

As the native GnRH peptide does not adsorb well on a silica surface, BSA was used as a carrier protein for this peptide to improve its adsorption capabilities. These complexes were synthesised using the EDC reaction, which forms chemical bonds between the peptide and various sites on the BSA protein. QCM measurements of these complexes were then undertaken to investigate to what extent they adsorb on a silica surface.

Graph 21 illustrates how the BSA conjugates adsorb in comparison to the native GnRH peptide and also BSA alone. It can be seen that each BSA conjugate exhibits some irreversible adsorption to the silica surface, which is in stark contrast to the native peptide alone, which does not effectively adsorb at all.

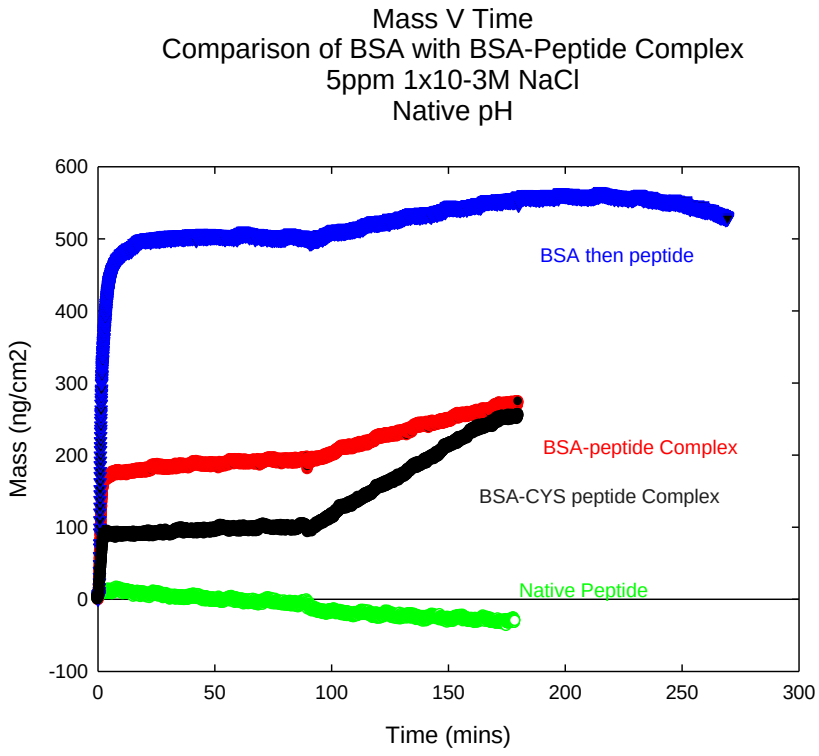

Graph 21: Adsorption comparison of BSA-peptide complex on a silica sensor

Graph 22 illustrates the BSA-peptide conjugate results and the experiments where BSA was adsorbed followed by each peptide. It can be clearly observed that there is no meaningful adsorption of either peptide after BSA has been adsorbed to the surface. This is probably due to the adsorbed BSA covering the available silica surface and the peptides not adhering to the adsorbed BSA. Once again the mass observed to increase upon rinsing for some of the experiments. This is possibly due to a sudden change in pH as mentioned previously.

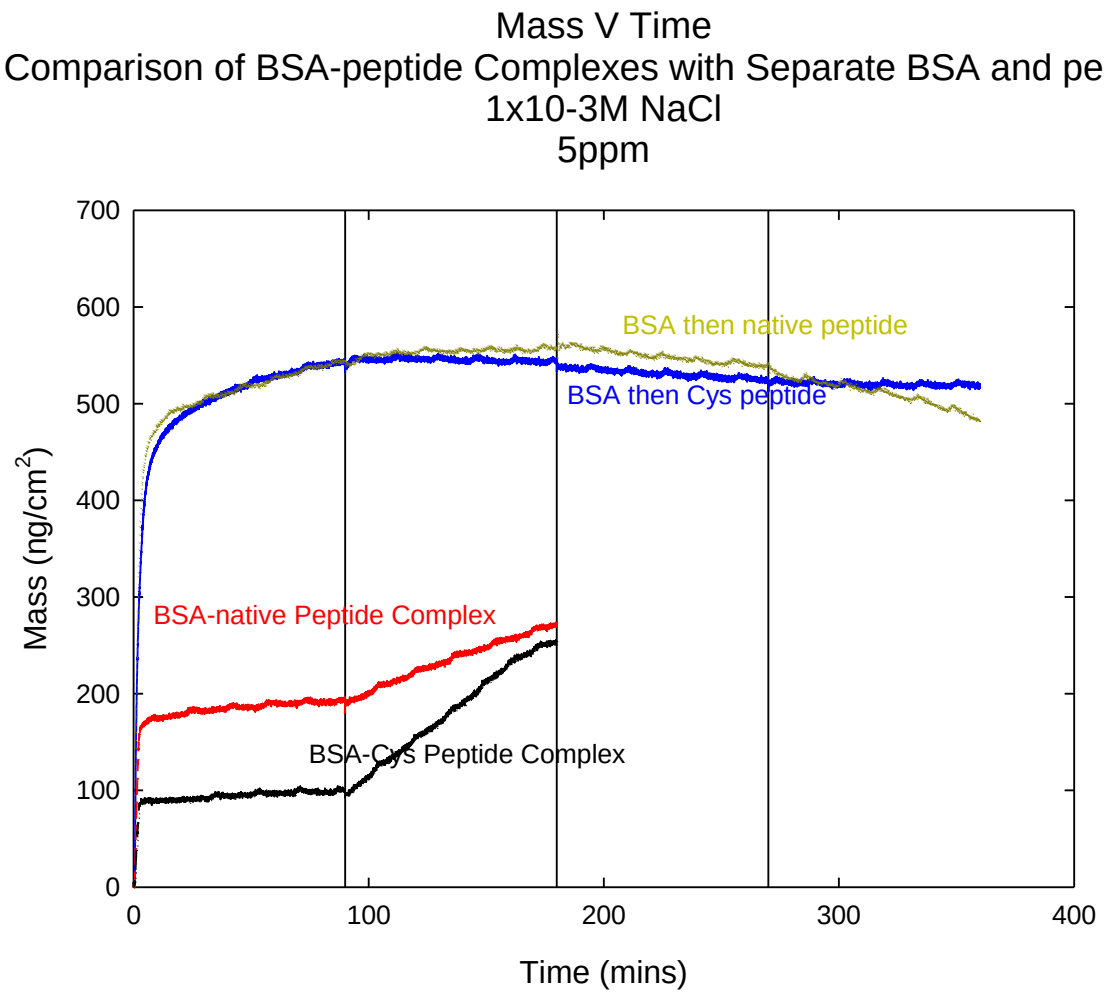

Graph 22: Adsorption comparison of the BSA-peptide complexes with BSA followed by peptide adsorption

It can be seen in Graph 23 that the adsorption levels of the free cys-peptide and the BSA-cys peptide conjugate are approximately the same. This suggests that either could be used with Stöber silica nanoparticles to be carried into the body. However, this may be due to a concentration problem associated with the conjugate. A yield of 100% was assumed from the EDC reaction (conjugating peptide and BSA), however this was likely to be lower. Consequently, the concentration of BSA-peptide conjugate used was probably lower than 5ppm.

What should be taken from this graph is that the synthesis of a BSA-native peptide conjugate is an effective method to adsorb native GnRH peptide material onto a silica nanoparticle.

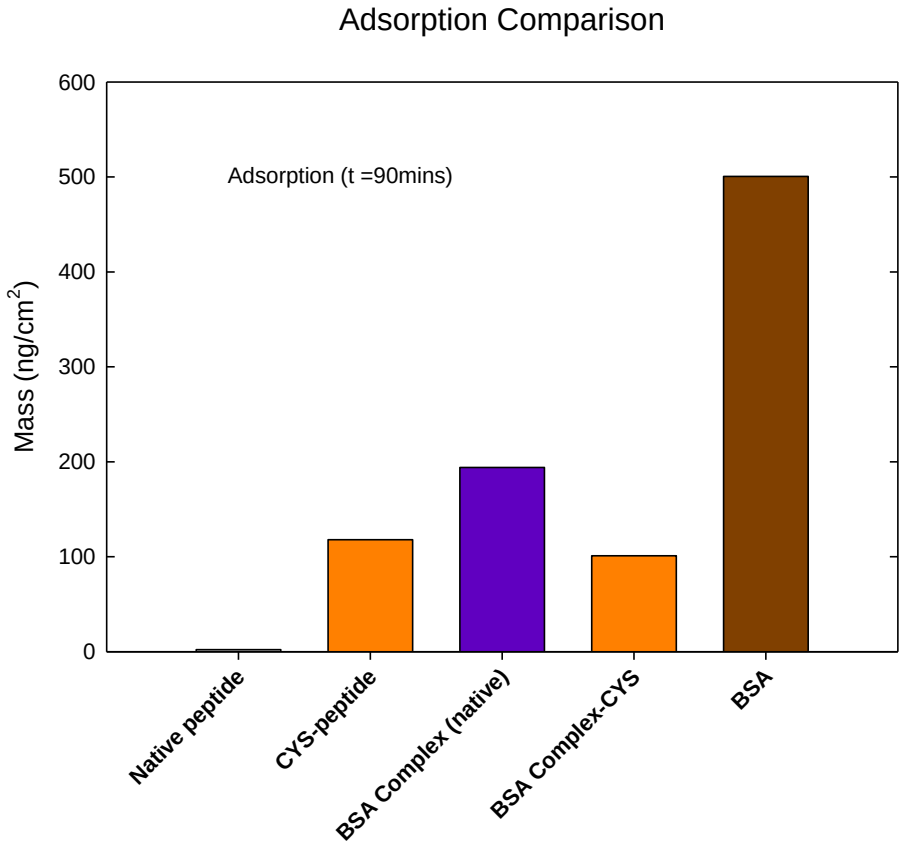

Graph 23: Reversible Adsorption comparison of peptides and BSA-peptide complexes.

4.3.10 Surface Plasmon Resonance

Surface plasmon resonance measurements were taken in order to find out how effectively each peptide and BSA complex adsorbed to a silica surface. SPR can be more accurate in comparison to QCM as SPR does not include the associated solvent and ions in the adsorbed material measurements.

4.3.11 Native Peptide

From the SPR measurements undertaken it was found that the amount of native GnRH-I that absorbed to the silica surface after 90 min was 9.86ng/cm^2. It was also noted that the adsorption appeared to increase during the rinsing step with NaCl salt solution and followed a linear trajectory for a further 90 min (Graph 24). This was unexpected as it shows a similar rate of adsorption to the 5ppm peptide solution. However, the adsorption of the native peptide is rather ineffective on the silica surface and the adsorbed material could be a build up of peptide and positively charged sodium ions.

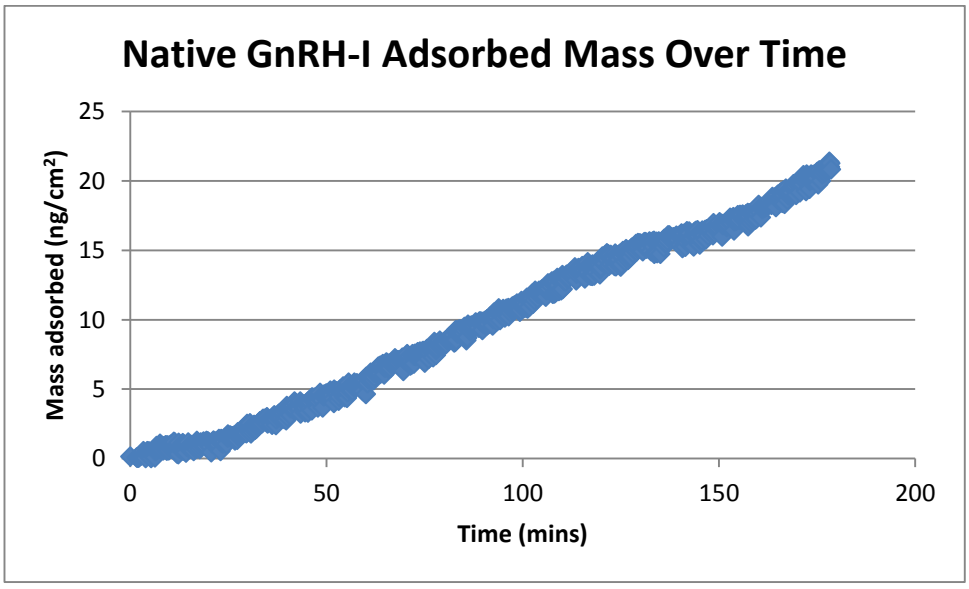

Graph 24: SPR Measurement of Native GnRH-I on a silica surface

4.3.12 Cys-GnRH-I Peptide

It was found that the amount of cys-GnRH-I peptide that adsorbed to the silica sensor after 90 min was 85.1ng/cm^2. The bulk of this adsorption occurred within the initial 20 min of the adsorption, suggesting that the sensor nears an adsorption saturation point for this peptide. In a similar vein to the native GnRH-I peptide SPR measurement the adsorption appears to increase during the rinsing step with NaCl solution (Graph 25). This could be a build up of positively charged sodium ions on the surface from the rinsing solution. This is less than the adsorbed amount observed via QCM measurements (~150ng/cm^2). This is most likely due to the inclusion of solvent and ions in the QCM measurement.

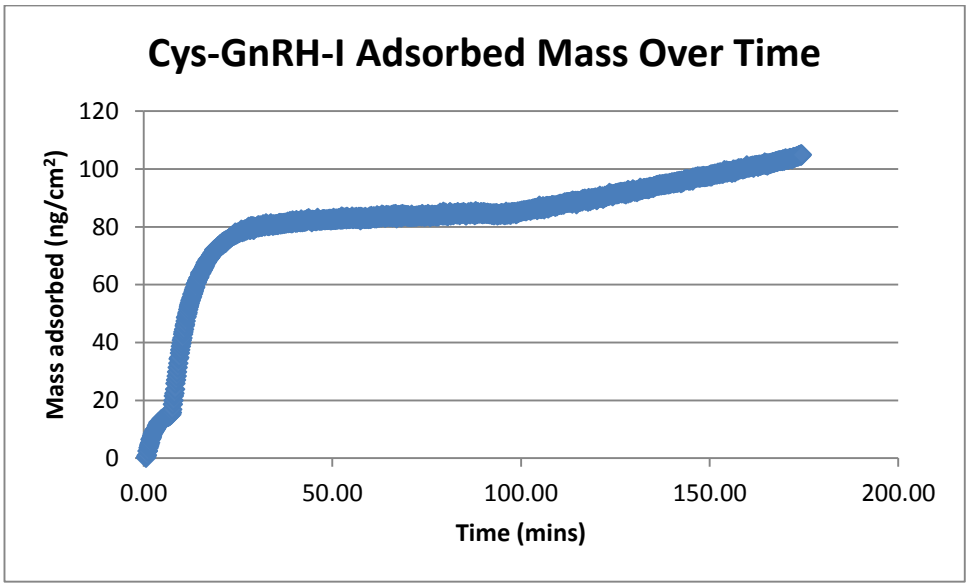

Graph 25: SPR Measurement of Native GnRH-I on a silica surface

4.3.13 Molecular Dynamics Simulations of Peptide Clusters

Peptide clusters on a silica surface were simulated in order to investigate the dynamics of how adsorbed clusters of peptides behaved and to show how monolayers may be formed. In the simulation of both the native and cys-GnRH-I peptide clusters on the silica surface it could be observed that all peptides remained adsorbed to the surface through the 50ns trajectory. However, there were differences in the two peptide cluster simulations.

It was observed in the native GnRH-I cluster simulation that the peptides tended to spread out over the surface away from each other. Upon doing this the native peptides then adopted a more 'collapsed' conformation on the silica surface, thus covering a greater surface area than if they remained upright (~25% of the available surface area) (Figure 27).

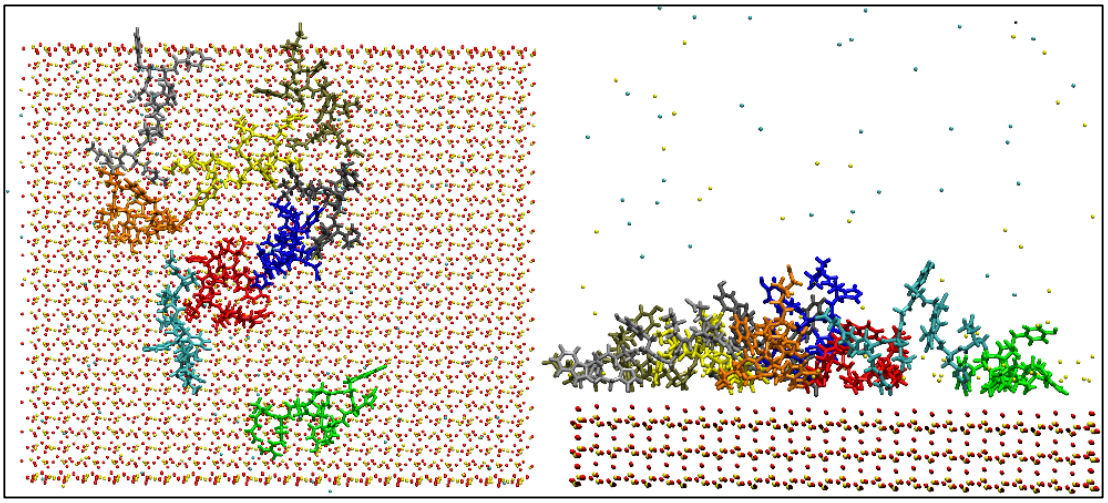

Figure 27: Top and side view of native GnRH-I peptide cluster adsorbed to silica surface

In the cys-GnRH-I cluster simulation it was apparent that most of the peptides tended to stay in a close-packed cluster formation on the silica slab, except one peptide,

which moved away from the cluster. In the main cluster, the peptides on the outside of the formation tended to collapse more onto the surface. Whereas the cys-GnRH-I peptides on the inside of the cluster tended to remain in a 'standing' position on the silica slab (Figure 28). If there were enough peptides present to cover the majority of the silica surface, then this may have been the case for all of the inner-cluster peptides.

If the peptide cluster occupies approximately 25% of the silica substrate then a quarter of the 88 Na^+ screening ions are excluded from interacting with the surface. The cys-peptide competes for 9 of these positions due to its positive charge, but the native peptide will not directly compete for any of these adsorption sites. Electrostatics could be a stronger driving force for the cys-peptide due to its charge, than it would be for the native peptide, thus explaining why the cys-peptide forms a more closely-packed cluster than the native peptide.

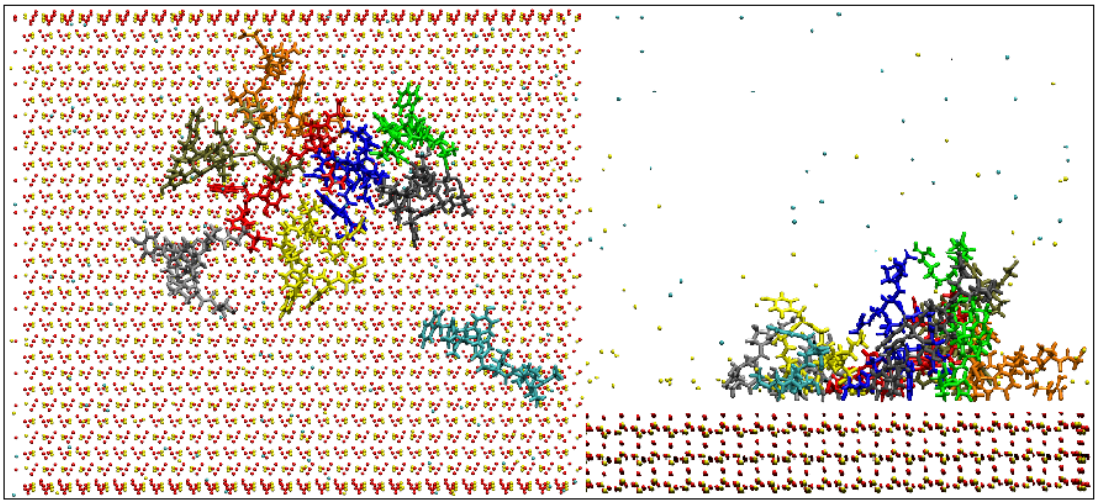

Figure 28: Top and side view of cys-GnRH-I peptide cluster adsorbed to silica surface.

4.3.14 Cys-Peptide Cluster SMD

Pulling in +z direction

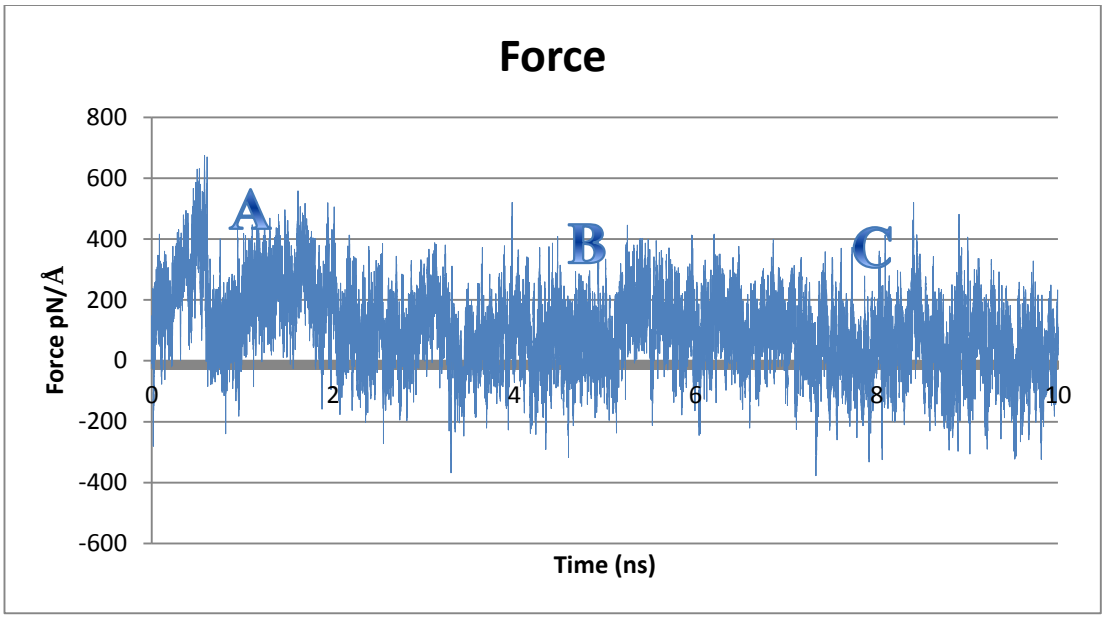

Graph 26: Force against time graph for the SMD trajectory pulling the N-terminus (cysteine residue) of an absorbed cys-GnRH-I peptide in a cluster of adsorbed peptides at high ionic strength.

After the adsorbed cluster simulation had completed, a peptide from the middle of the cluster was pulled by the N-terminus (cysteine residue) in the +z direction away from the surface at a rate of 0.005Å/ps for 10ns in order to investigate how peptides desorb from peptide clusters and the relative binding energy of an adsorbed peptide in a cluster. Each jump in force correlates with an event in the desorption process. The energy of these events was calculated and the strength of the adsorbed peptide was compared to previous SMD studies (section 3.4). Figure 29 illustrates the main events in this simulation.

Events

A – The peptide pulled from the surface at 2.6ns (0.2eV) (with adsorbed cysteine desorption at approximately 0.8ns (0.3eV)) → 0.3eV + 0.2eV = 0.5eV

B – Peptide begins to move away from cluster → 0.14eV

C – Peptide fully desorbs from cluster → 0.1eV

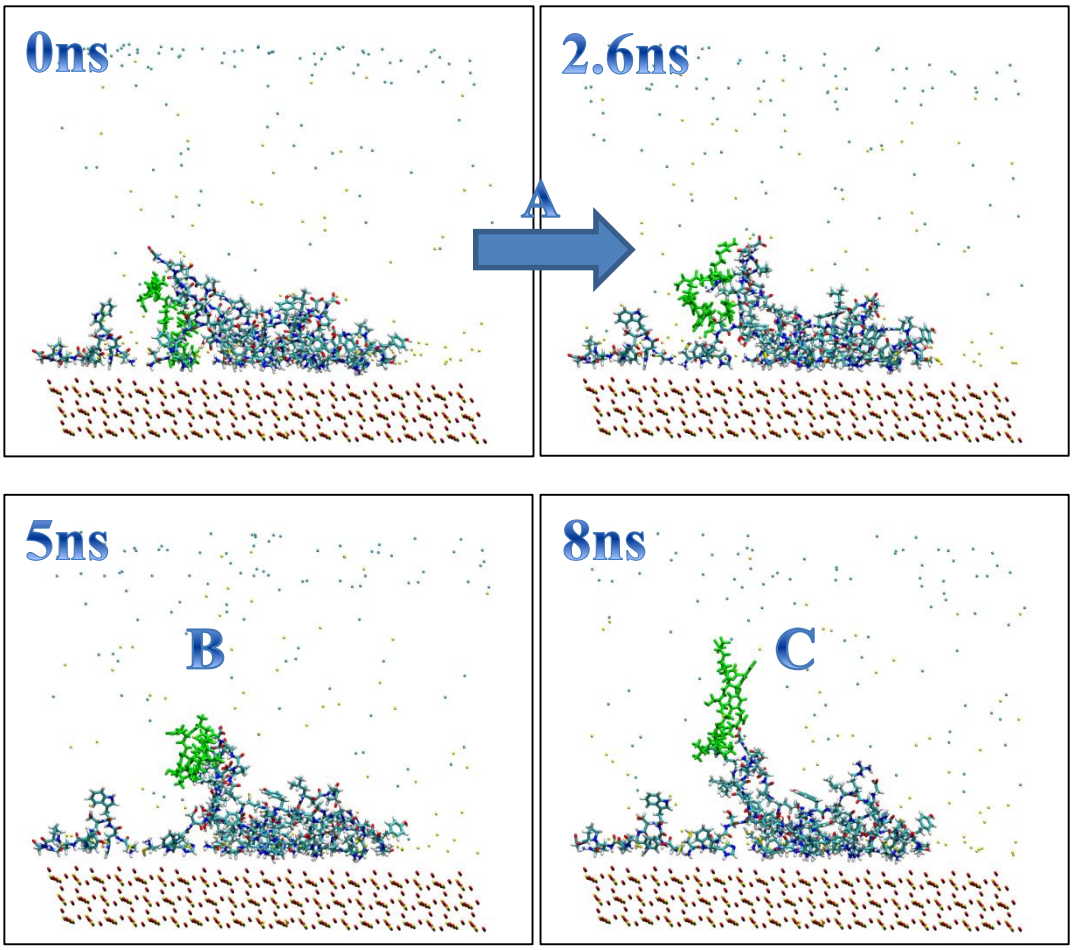

Figure 29: SMD simulation event images for pulling the N-terminus of an adsorbed cys-GnRH-I peptide from an adsorbed cys-peptide cluster in high ionic strength. The pulled residue is highlighted in green (water not shown for clarity).

4.3.15 Molecular Dynamics Simulations of BSA-Peptide Complex

Two cys-GnRH-I peptides were chemically bonded to a BSA monomer in regions where peptide-BSA interactions seemed to be strong in previous simulations. These peptides were placed between residues 113 (proline) and 114 (leucine) [blue peptide] and also residues 306 (alanine) and 307 (phenylalanine) [red peptide]. In this simulation it was observed that one cys-GnRH-I peptide [red] interacts heavily with the BSA molecule staying largely 'adsorbed' to the protein structure. Whereas the other linked peptide [blue] was observed to be pointed outwards from the main BSA structure, thus presented to the surrounding environment consistently for the entire 50ns simulation (Figure 30). Both peptides were bound by different termini: blue – bound by N-terminal; red – bound by C-terminal.

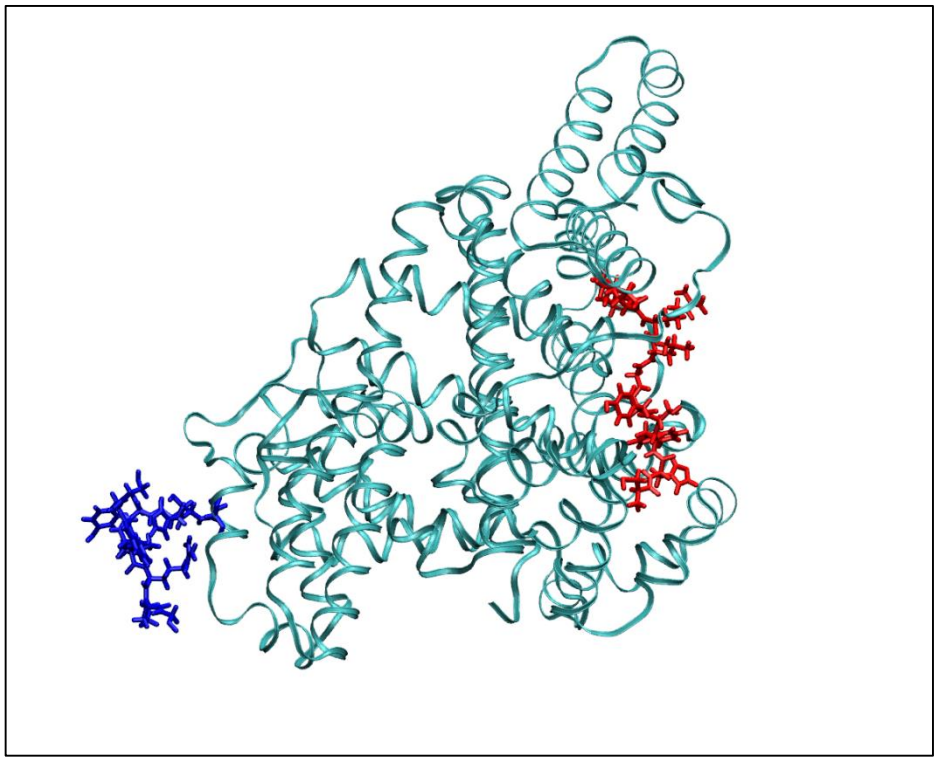

Figure 30: Image of two cys-GnRH-I peptides chemically linked to a BSA monomer. The secondary structure of BSA is shown for clarity.

4.4 Discussion

The aim of this chapter was to synthesise and characterise spherical silica nanoparticles and to investigate how native GnRH-I and cys-GnRH-I peptides adsorbed on silica surfaces using complementary analytical techniques.

Established characterisation methods were used to find the size, shape and zeta-potential of the silica nanoparticles produced. From DLS measurements it was found that the size of nanoparticles produced was approximately 200nm as expected. However, a little particle swelling was observed with decreasing pH, until the isoelectric point was reached (at approximately pH 3.0) where the particles agglomerated. This effect was expected as at the isoelectric point there would be a lack of significant electrostatic repulsion preventing agglomeration. This observation is significant as it helps determine through what route silica systems can be administered – for example oral delivery of silica systems may not be practical as the silica particles would likely agglomerate in the stomach due to low pH levels. SEM used in this study confirmed the spherical shape and monodispersity of the silica nanoparticles produced, as expected by the Stöber synthesis method and DLS results (Stöber *et al*. 1968; Nozawa *et al*. 2005). Zeta potential measurements showed that the surface charge of silica nanoparticles was negative (-57.2mV at pH 7.1). This suggests that adsorption of positively charged peptides (i.e. cys-GnRH-I) would be more favourable than negatively charged or neutral peptides.

In order to examine surface adsorption of peptides in more detail, QCM measurements were taken of each peptide on a silica substrate. From the results shown in Graph 19 it is clear that the cys-GnRH-I peptide adsorbs much more readily than the native GnRH-I peptide. This corresponds well with the zeta potential

results as the positively charged cys-peptide should adsorb more readily to the negative silica surface than the overall uncharged native peptide.

Graph 20 shows that the cys-peptide is able to bind to the silica surface at all pH levels, but most effectively at a near-neutral pH of 7.4, whereas at lower pH levels, the native GnRH-I peptide fails to adsorb effectively whatsoever. The reason for the change at lower pH levels may be due to the protonation of the histidine residue in acidic conditions, which would change the overall charge of the peptide and thus its dynamic behaviour. However, this is not fully confirmed by this study and would have to be looked into further. In both peptides, the adsorption is greatest at a pH of 7.4, which is advantageous as 7.4 is physiological pH, suggesting that the peptides are more likely to remain adsorbed to the silica adjuvant *in vivo.* The exact reason for this is unknown, but it could be due to the isoelectric points of both peptides being at basic pH levels (pH 8 for native GnRH-I; pH 9.16 for cys-GnRH-I). Above this isoelectric point peptide aggregation may occur and the secondary structure of each peptide is likely to alter, thus affecting the dynamic ability in solvent of the peptide in question.

From QCM measurements the BSA-native GnRH-I complex exhibits irreversible adsorption to the silica surface. This is in stark contrast to the unbound native GnRH-I peptide which does not exhibit effective permanent adsorption on a silica surface. As such, the BSA-peptide complex may be a suitable candidate for delivery of native GnRH-I into the bloodstream. However, QCM does not provide information on how the peptide molecules are presented on the BSA surface to the surrounding environment.

Graph 23 also clearly shows that BSA appears to bind more readily than either of the BSA complexes. However, this may be down to a concentration issue. BSA was used at a concentration of 5ppm for this experiment, whereas the complexes were assumed to be at a concentration of 5ppm. However, this was impossible to know for sure as it was unclear how much of each pure BSA-complex was produced through the EDC reaction. It was assumed to have a yield of 100%, but in reality this is likely to be lower. It may have been useful to repeat these experiments at a higher concentration.

However, QCM can only measure the mass adsorbed on the surface, which includes associated solvent and ions. As such, it is not clear whether a peptide monolayer or multilayer is formed on the silica surface and how these peptides are presented on the surface to the surrounding environment. SPR measurements were used to measure the contact angle of peptide adsorption, thus providing a more accurate adsorption level for each peptide.

From SPR measurements of the native GnRH-I peptide it was found that at a wavelength of 670nm that 9.86ng/cm^2 of peptide adsorbed on a silica surface. From Graph 24, it was also observed that the amount of adsorbed material on the sensor increased during the rinsing step at around the same rate as the peptide adsorption step. This may be due to positively charged sodium ions ($1x10^{-3}$M NaCl solution was used for the rinsing process) becoming trapped between adsorbed peptides, or it could also be the same positively charged sodium ions adsorbing on the silica surface. In any case, these SPR measurements show that the adsorption of the native GnRH-I peptide on silica is not very effective. However, the SPR measurement of the cys-GnRH-I peptide on the silica surface shows a much more effective

adsorption. During the adsorption step 85.1ng/cm^2 of cys-GnRH-I peptide adsorbed onto the silica surface relatively quickly, as the sensor appears to show saturation after approximately 20 min for this peptide. This illustrates that the cys-GnRH-I peptide adsorbs much more effectively than the native peptide, which correlates with data acquired from QCM measurements. It should be noted that during the rinsing step with the NaCl solution that the adsorbed mass on the silica sensor increases at roughly the same rate as that of the native peptide adsorption. This suggests that there was some adsorption of positively charged sodium ions on the silica sensor during the rinsing step of both peptide adsorptions.

In order to further investigate how peptide monolayers would behave on a silica surface molecular dynamics simulations were performed. These simulations were prepared with clusters of native GnRH-I and cys-GnRH-I peptides adsorbed in a 'standing' conformation to a silica slab. From these simulations it was observed that from an already adsorbed state that both peptides didn't desorb from the surface. However, the native GnRH-I cluster appeared to spread out more (Figures 27 and 28) than its cys-GnRH-I counterpart, which generally remained in a close-packed form. It was also noted that the peptides in the native GnRH-I cluster had a tendency to collapse on the surface, whereas it was only the peptides on the fringes of the cys-GnRH-I cluster that collapsed. This correlated with earlier simulations, which suggested that once adsorbed, the cys-GnRH-I peptide requires less amino acid 'anchors' to remain attached to the silica surface. The tightly packed nature of the cys-GnRH-I cluster also correlated somewhat with the QCM and SPR measurements, as it would suggest that a greater mass of peptide would adsorb per unit area on a

silica surface. However, it must be noted that this result is not as prominent in these cluster simulations as it was in physical experiments.

An SMD study of the cys-peptide cluster was also performed. This showed that all of the events which happened during the cys-peptide desorption occurred on a nanosecond timescale, agreeing with the Arrhenius rates of previously studied desorption simulations (section 3.4). However, the 0.4eV barrier, which corresponds to microsecond timescales (section 3.2.2, Table 2) was not breached spontaneously in this simulation. The cumulative estimated activation energy of desorption is above 0.4eV, which explains why there is no spontaneous adsorption in the cys-peptide cluster simulation as the simulation is on a nanosecond timescale. An SMD comparison between the native and cys-peptide clusters would likely see the activation energy for desorption lower for the native cluster. This would mainly be due to the lack of a charge interaction between the peptides and the surface in the native cluster.

A molecular dynamics simulation was also carried out to investigate the dynamic behaviour of cys-GnRH-I peptides chemically linked to a BSA monomer. In a simulation with two peptides attached to a BSA molecule it was observed that one peptide (bound by N-terminus) was presented effectively to the surrounding solvent, whereas the other (bound by C-terminus) adsorbed fully onto the large BSA protein. The result from this simulation is encouraging as it suggests that with only two cys-GnRH-I peptides conjugated to BSA, one of these peptides will be free to interact with the surrounding environment. In a 1:1 weight ratio of BSA to peptide there would actually be approximately 20 peptides free to conjugate to each BSA monomer. Therefore it could be suggested that there would be various points on the

peptide-BSA conjugate that would have cys-GnRH-I epitopes for the immune system to interact with. However, further simulations would need to be carried out in order to investigate how a greater amount of peptides bound to BSA would appear and also how native GnRH-I would behave in a similar system.

Chapter 5 – Immunological Study

5.1 Aims

The application of GnRH-I peptides has previously been studied in the formulation and development of vaccines for hormonal and fertility treatments (Levy *et al*., 2004; Levy *et al*., 2011; Khan *et al*., 2007). However, as GnRH-I is a peptide produced naturally *in vivo* (ie a self peptide), it requires the addition of a carrier protein and adjuvant to improve its immunogenic properties in order for the body to recognise the antigen as "foreign". Silica nanoparticles have been used in order to transport and increase the immunogenicity of biomolecules in previous studies (Mody *et al.,* 2013), however the morphology of these nanoparticles dictates the inherent cytotoxic properties. Mesoporous silica nanoparticles can cause oxidative stress on cells, whereas non-porous Stöber silica show low cytotoxicity and have a reduced inflammatory response (Han *et al.*, 2011; Blumen *et al.*, 2007). The aim of this chapter is to:

- Illustrate the effectiveness of Stöber silica nanoparticles as a carrier for GnRH-I and its modified analogue cys-GnRH-I.
- Compare the use of Stöber silica as an adjuvant with that of BSA and in conjunction with BSA by measuring the GnRH-I specific IgG antibody response of immunised male BALB/c mice.
- Investigate the effect of these GnRH treatments on the associated GnRH hormonal pathways by measuring the effect on testosterone production of treated male BALB/c mice.

5.2 Materials and Methods

5.2.1 Cytotoxicity Study

In order for the silica nanoparticles to be useful as a carrier/delivery system they need to be safe to use *in vivo*. As such, a cytotoxicity study of Stöber silica was performed on a normal cell line (human prostate epithelial cells – PNT2A), kindly supplied by Mrs Louise Young, SIPBS, University of Strathclyde. Human prostate cells were preferred over mouse leukocytes as prostate cells are homogenous cell type, thus providing a more definitive experiment. Prostate cells are also able to be grown easily compared to some other cell types. The cells were prepared and exposed to varying concentrations of Stöber silica as follows, under sterile conditions in a tissue culture laminar hood:

A 1mL aliquot of cells was removed from frozen liquid nitrogen storage and placed into complete Roswell Park Memorial Institute (RPMI) 1640 medium (10% v/v foetal bovine serum (FBS), 1% v/v penicillin/streptomycin, 2mM glutamine) and incubated at 37°C, 100% humidity and 5% CO_2. The cells were monitored daily by looking at morphology and confluency under a light microscope and checking for microbial contamination. The cell medium was replaced every 2-3 days to replenish nutrients. When the cells were 70-80% confluent, they were trypsinised with 5ml 0.25% (v/v) ethylenediaminetetraacetic acid (EDTA)-trypsin and incubated for 10 min (37°C, 5% CO_2). The cells were then centrifuged at 1000g for 4 minutes. The supernatant was disposed of and the cells were resuspended in 10ml complete RPMI medium. The cells were then counted with the aid of a haemocytometer (Figure 31). This was facilitated by mixing 100µL of cell suspension with 100µL trypan blue. A glass coverslip was then fixed to the haemocytometer and 10µL of the trypan blue-

cell suspension was added to each chamber. The live cells (clear as opposed to blue) in the centre and in each corner of the grid were then counted and an average was taken and multiplied by the dilution factor and 100 to obtain the total number of cells per mL.

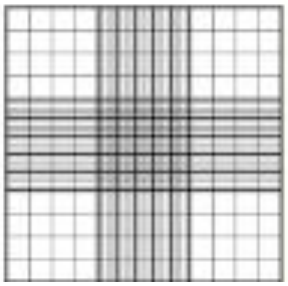

Figure 31 – Haemocytometer Grid

A Newbauer haemocytometer was used to count the cells (Figure 31). The desired volume of cell stock solution to be diluted for the cytotoxicity study was then calculated; 1 x 10^5 cells/ml were required for the study. One hundred µL of cell suspension was added into individual wells on a 96 well plate in rows A to F, with medium only added to rows G and H. The plate was then tapped to ensure an even spread of cells and the plate was incubated at 37°C, 100% humidity, 5% CO_2 for 24 h.

A resazurin reduction assay was used as an indicator to measure the metabolically active cells in this cytotoxicity study. Resazurin is a deep blue coloured solution which turns pink when cells with functioning metabolic processes reduce resazurin to resorufin, a pink fluorescent product (Riss *et al*. 2013). The quantity of reduced resazurin can then be measured using a microplate fluorometer with an excitation/emission filter set of 560nm/590nm respectively.

Five mg resazurin salt was dissolved in 50mL deionised water. This was then filter sterilised (using a 0.22µm pore size filter unit) and aliquoted into 5ml bijoux, wrapped in foil to occlude light and stored at 4°C until used. The resazurin stock solution was then diluted by adding 1.2ml of the resazurin to 10.8ml RPMI complete medium. One hundred µL of this solution was added to each well of the 96 well plate, covered with foil and incubated at 37°C for 24 h. The excitation/emission was then read at 560nm/590nm.

Sterilised Silica Nanoparticles

The effect of thermo-sterilisation of the Stöber silica nanoparticles was also investigated. A sample (5ml) of Stöber silica was dried in a vacuum oven at 180°C for 5 h and then left under vacuum overnight. The resulting powder was weighed (1.02g) and suspended in 5ml of complete RPMI medium. The resulting mixture was sonicated until complete dissolution had taken place – producing a milky pink solution. A non-sterilised silica sample was also prepared to the same concentration as the sterilised silica (0.2g/ml).

Two hundred µL of both nanoparticle samples were added in triplicate to column 1 (see Table 4) and 100µL of complete RPMI media was added to the remaining columns up to column 11. A 1 in 2 serial dilution of the nanoparticles was then carried out across the plate by transferring 100µL of the nanoparticles in column 1 to the adjacent column. This dilution was repeated until column 11, where the last 100µL was discarded (see Table 4 for plate template).

In column 12 positive and negative controls were added to the well plate. The positive control was performed in triplicate and contained cells only, whereas the

negative control was performed in triplicate and was spiked with 0.22µm filter-sterilised dimethyl sulphoxide (DMSO), in order to trigger cell death. Further controls were also prepared in rows G and H. These rows contained nanoparticles only (see Table 4 for plate template).

The plate was tapped gently to ensure the nanoparticles were spread evenly. The plate was then placed in an incubator at 37°C, 5% CO_2 and 100% humidity for 24 h.

Conc. (g/ml)	0.2	0.1	0.05	0.025	0.0125	0.00625	3.125×10^{-3}	1.563×10^{-3}	7.81×10^{-4}	3.91×10^{-4}	1.95×10^{-4}	
	1	2	3	4	5	6	7	8	9	10	11	12
A												Cells Only
B												Cells Only
C												Cells Only
D												DMSO
E												DMSO
F												DMSO
G	No Cells	No Cells	No Cells	No Cells	No Cells	No Cells	No Cells	No Cells	No Cells	No Cells	No Cells	
H	No Cells	No Cells	No Cells	No Cells	No Cells	No Cells	No Cells	No Cells	No Cells	No Cells	No Cells	

Table 4 – Make-up of Well Plate Used in Cytotoxicity Study

Key	Unsterilised particles
	Sterilised particles
	Cells only

5.2.2 Animal Study

All animal experiments were conducted in accordance with UK Home Office Legislation and were approved by the University of Strathclyde Animal Welfare and Ethical Review Committee. In-house bred male BALB/c mice, aged 8 weeks at the start of the study, were kept in a controlled environment: room temperature 22°C; 50-70% humidity; summertime light cycle of 14 hours light per day; 5 animals per cage. All mice were ear coded; food and water were supplied *ad libitum*. Unless stated otherwise, subcutaneous injections were administered fortnightly as detailed below and blood samples were taken in alternate weeks. The mice were sacrificed after 13 weeks. The immunisation regime for each group is given in Table 5.

Table 5: The immunisation regime used in this study. For clarity, the results identify the groups with the treatment received, rather than group number.

Group	Immunogen	Adminstration Route	Peptide Dosage
I	Untreated Control	N/A	N/A
II	GnRH-I-Silica	s.c	50µg in 100µL
III	Cys-GnRH-I-Silica	s.c	50µg in 100µL
IV	Cys-GnRH-I-BSA	s.c	50µg in 100µL
V	Cys-GnRH-I-BSA-Silica	s.c	50µg in 100µL
VI	GnRH-I-BSA	s.c	50µg in 100µL
VII	GnRH-I-BSA-Silica	s.c	50µg in 100µL
VIII	GnRH-I	i.n	50µg in 20µL
IX	GnRH-I-BSA	i.n	50µg in 20µL

In all immunisation treatment groups, each mouse was administered a dose of 0.1mL subcutaneously, s.c (except in groups VIII and IX in which 20µL were administered nasally, i.n) containing the equivalent of 50µg of peptide per dose fortnightly. Tail bleeds were collected 7 days after each immunisation. Serum was prepared by centrifuging each blood sample at 1000g for 20 min. The serum was then collected in fresh 0.5mL microfuge tubes and frozen at -20°C until analysed by ELISA. At the end of the study, blood was collected via cardiac puncture and serum prepared.

One control group was deemed satisfactory for this study as only one strain of inbred BALB/c mice from the same animal house was used over a short period of time.

5.2.3 Immunogen Preparation

The Group II treatment was formulated by mixing 100µL silica (0.2g/ml) and 900µL water. One mg native-GnRH (Genosphere Biotech, France, >95%) was dissolved in 1mL water and added to this solution. The resulting mixture was stirred at room temperature for 1 h and then frozen until further use.

The Group III treatment was prepared by mixing 100µL silica (0.2g/ml) and 900µL water. One mg cys-GnRH (Immune Systems Ltd, UK, >95%) was dissolved in 1mL water and added to this solution. The resulting mixture was left to stir magnetically for 1 h and then frozen until further use.

The treatment for Group IV was prepared by conjugating cys-GnRH-I and BSA using the EDC reaction (section 4.2.2) with the final sample containing 2.5mg peptide. The resulting solution was then frozen until further use.

Group V treatment was prepared via the same steps used in that of Group IV with the resulting mixture being mixed with 100µL silica (0.2g/ml) + 900µL water and then frozen to await further use.

Similarly, treatments for Groups VI and VII were prepared using the same steps as Group IV and V respectively, but the cys-GnRH-I peptide was substituted for the native GnRH-I peptide. The treatment for Groups VIII and IX were also prepared in the same way, but with water in order to provide a concentration of 50µg per dose of 20µL.

5.2.4 Measurement of Specific Antibody Levels

The specific antibody levels were measured using an ELISA as follows:

OVA-peptide conjugate (equivalent to 1.25µg per well in 100µL phosphate buffer saline solution (PBS [137mM NaCl, 2.7mM KCl, 4.3mM Na_2HPO_4, 1.47mM KH_2PO_4], pH 7.4) was coated onto tissue culture grade 96-well plates overnight in a fridge. The plates were washed twice with washing buffer (PBS, containing 0.05% Tween 20) and blocked with 3% (w/v) non-fat milk protein (Marvel, Premier Foods, UK) in PBS for 2h at 37°C. The plates were then washed 3 times with washing buffer. Mouse sera (1.2µL in 1mL PBS, prepared from tail bleeds) was incubated per well for 1h at 37°C (carried out in triplicate for each sample). The plates were then washed 3 times with washing buffer. Anti-mouse IgG horseradish peroxidase (HRP) was diluted 1:5000 in PBS and 100µL per well was incubated for 45 min at 37°C. The wells were then washed three times with washing buffer and twice with PBS alone and developed with 100µL Ultra-TMB (3,3',5,5'-tetramethylbenzidine) substrate per well. This elicits a blue colour when mixed with antibody bound-HRP conjugate. The antibody used was goat anti-mouse IgG (heavy and light chain; Pierce Antibody, Thermo Fisher Scientific, UK). The reaction was stopped with 100µL per well 10% (v/v) sulphuric acid after 15 min which turned the blue colour to yellow and the A_{450} read on a SpectraMax M5 plate reader. The intensity of this yellow colour is inversely proportional to the concentration of antibody present in the test sera (i.e. the A_{450} value [blue in spectrum] is higher for a higher antibody concentration). The mean and standard deviations of the triplicate results were calculated and plotted against the study week number.

5.2.5 Testosterone Study

Testosterone levels in the serum of the immunised mice were measured using a testosterone ELISA kit (Alpha Diagnostic Internations, USA) which is a competitive solid phase ELISA. Any testosterone in the serum competitively binds to antibody sites (in competition with enzyme-linked testosterone). When performing the assay the serum was incubated with anti-testosterone and testosterone-HRP (horseradish peroxidase) conjugate. Any testosterone which was unbound to the antibody sites was washed away with washing buffer (as in section 5.2.4). After antibody binding, TMB was added and after 15 min, the reaction was halted. The intensity of colour is inversely proportional to the concentration of testosterone in the serum and was read by plate reader (SpectraMax M5 – Absorbance 450nm).

All mouse sera samples were assayed in duplicate and low and high testosterone control samples were included in all runs.

5.3 Results

5.3.1 Cytotoxicity Results

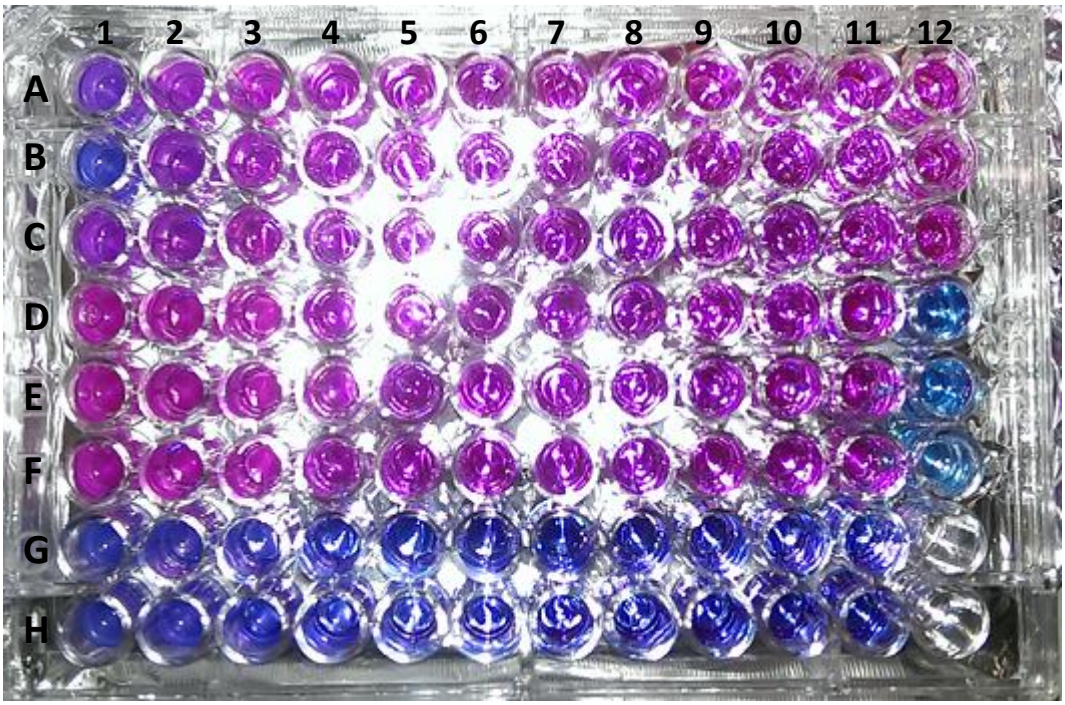

Figure 32 – A typical 96 well plate after incubation with resazurin

The make-up of the plate in figure 32 is as follows:

- Cells A1 to A11 contain cells which have been incubated with unsterilised Stöber silica nanoparticles, in decreasing concentration along the row.
- Cell A12 contains only living cells that have not been in contact with silica as a positive control.
- Rows B and C are duplicates of row A.
- Cells D1 to D11 contain cells which have been incubated with temperature-sterilised Stöber silica nanoparticles, in decreasing concentration along the row.

- Cell D12 contains cells that have been killed using DMSO as a negative control.
- Rows E and F are duplicates of row D.
- Rows G and H contain Stöber silica in decreasing concentration across the row, but with no cells present as a negative control.
- For a more detailed description refer to section 5.2.1, Table 4.

In figure 32 above, the negative controls have all remained blue, while the sterilised Stöber nanoparticles do not appear to exhibit cytotoxic effects, with all of the wells showing a bright pink colour. The majority of the unsterilised Stöber also appear to be non-toxic to these cells. However, the highest concentration of these particles exhibited toxic properties (indicated by the blue colour). The reason for this is unknown, as they are at the same concentration as the sterilised Stöber particles and do not exhibit cytotoxic properties at lower concentrations.

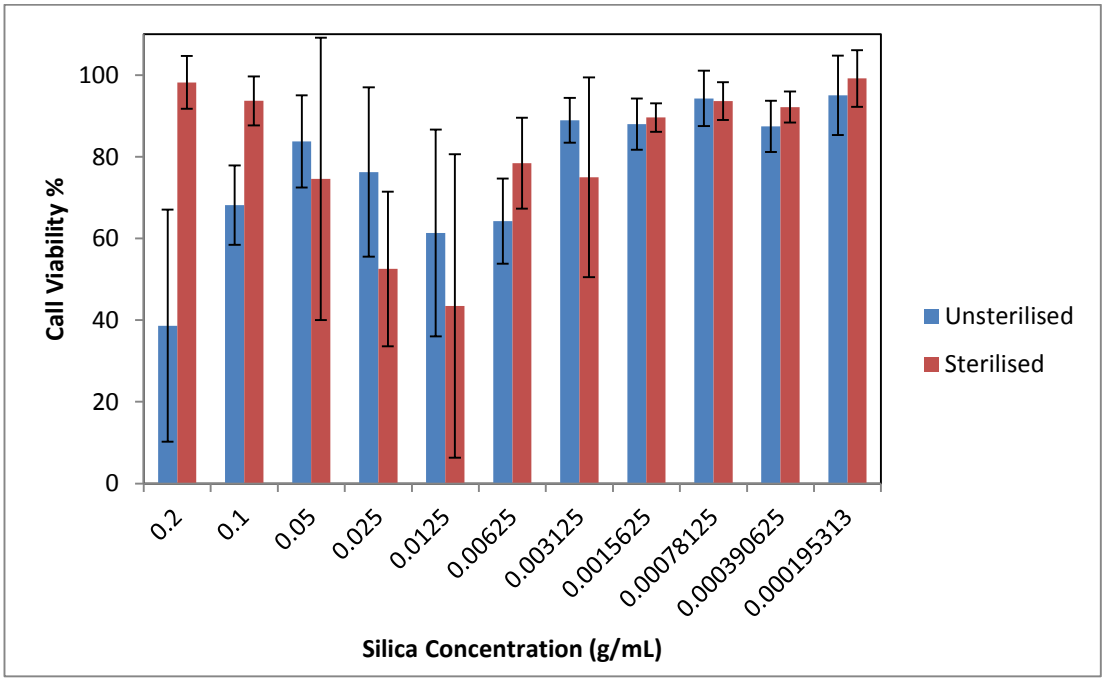

Graph 27: Toxicity measurements of silica nanoparticles at varying concentrations. Each bar is the mean of triplicate readings with ±SD (n=3).

Graph 27 shows that the cells exposed to sterilised silica are largely viable, however there is increased toxicity at a sterilised silica concentration 0.0125g/mL. However, there is a large standard deviation at this concentration, suggesting that there may have been some contamination in the cells. It is not clear whether the same result would be obtained with a repeat measurement.

5.3.2 Antibody

Specific anti-GnRH-I antibody levels varied in the sera of the different groups of immunised mice. Two animal studies were run separately, with Groups II-V run first and Groups VI-IX (plus control group) performed after this study. Graphs 28 and 29 show that a specific IgG response to GnRH-I was seen in groups immunised with native GnRH-I-silica (0.53 ± 0.01), cys-GnRH-I-silica (0.61 ± 0.02), cys-GnRH-I-BSA-silica (1.07 ± 0.01) and cys-GnRH-I-BSA (0.82 ± 0.01) by week 5 of treatment with A_{450} above 0.5, indicating a specific immune response. After week 7 the animals were not immunised for a period of 4 weeks to investigate the effect on antibody levels during this period. The group treated with silica-BSA-cys-GnRH-I conjugate mean antibody titre continued to increase (1.23 ± 0.01 to 1.59 ± 0.41) in this period, with the response for all other groups decreasing; in fact groups immunised with native GnRH-I-silica and cys-GnRH-I-silica decreased to a negligible level. After the final vaccination at week 13 all treatment groups showed an increased specific IgG response once again.

The group treated with the silica-BSA-cys-GnRH-I conjugate showed a GnRH-I specific IgG level increase throughout the study. The final antibody response in this group (A_{450} of ~2.60 ± 0.26) was much higher than any other group. The group treated with BSA-cys-GnRH-I also exhibited a response (a final A_{450} of

~0.90 ± 0.33), but the inclusion of silica elicited a much higher immune response from the animals.

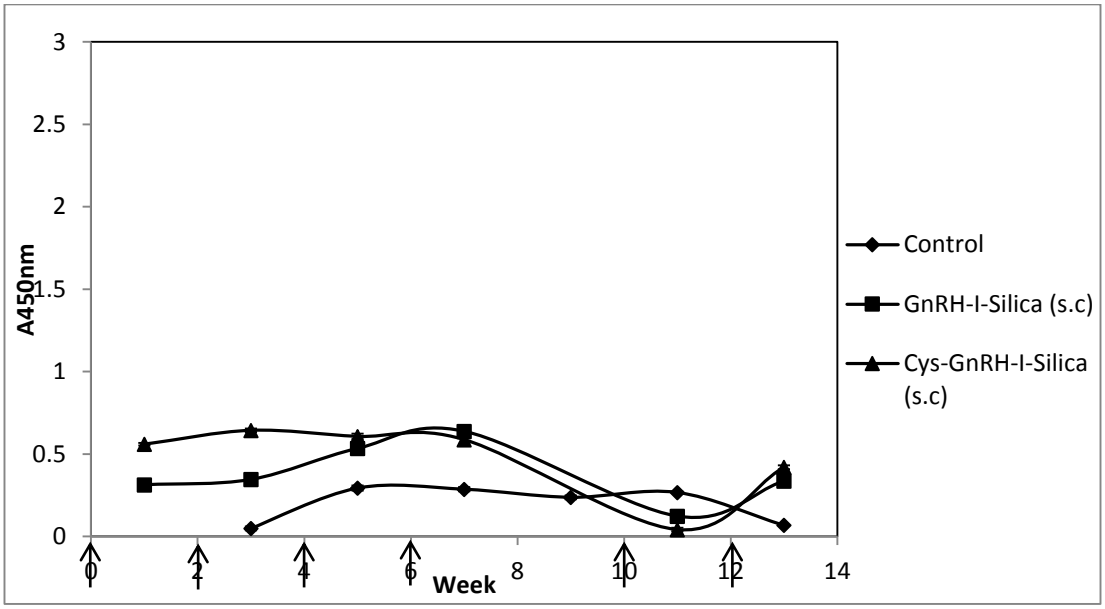

Graph 28: GnRH-I specific IgG response for animals immunised against native GnRH-I and the modified analogue (Cys-GnRH-I) adsorption to silica nanoparticles. The absorbance results were measured from ELISAs undertaken on OVA-GnRH-I coated plates. Each data point is the average of triplicate A450 readings with ±SD (n=5). Immunisations were administered subcutaneously in weeks 0, 2, 4, 6, 10 and 12 (marked with arrows) with bloods taken a week after each injection.

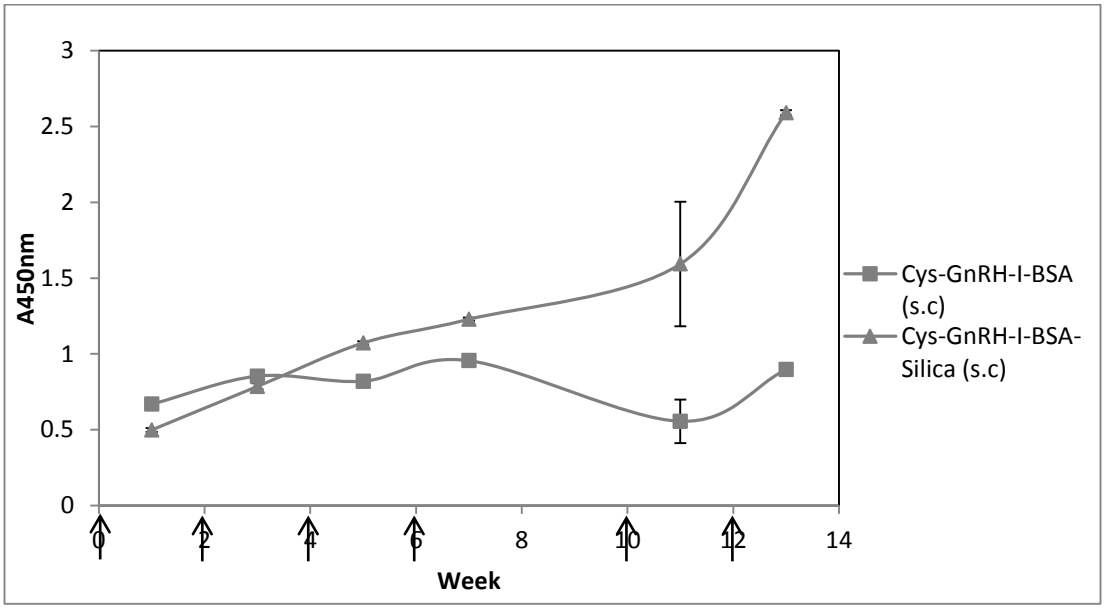

Graph 29: GnRH-I specific IgG response for animals immunised against the modified GnRH-I analogue (Cys-GnRH-I), conjugated to BSA and with/without adsorption to silica. The absorbance results were measured from ELISAs undertaken on OVA-GnRH-I coated plates. Each data point is the average of triplicate A450 readings with ±SD (n=5). Immunisations were administered subcutaneously in weeks 0, 2, 4, 6, 10 and 12 (marked with arrows) with bloods taken a week after each injection.

Graph 30 shows that after 5 weeks of treatment, mice immunised with silica-BSA-GnRH-I exhibited a specific IgG antibody response with A_{450} above 0.5 (0.84 ± 0.018). The antibody response in this group appeared to increase with subsequent booster immunisations. At the conclusion of the study the antibody response reached a peak A_{450} reading of 2.10 ± 0.022. However, mice immunised with native GnRH-I-BSA conjugate and the control group did not show a high specific antibody response in the first 5 weeks of treatment. A significant change in immune response was noted after a period of 11 weeks of treatment for the group immunised with BSA-Native GnRH-I (A_{450} reading of 0.69 ± 0.01), which continued to increase to the conclusion of the study to an A_{450} reading of 2.11±0.03. As expected, the antibody response of the control group never reaches an A_{450} reading of 0.5, peaking at 0.29 (± 0.01) before tailing off at the end of the study to 0.07 (± 0.004).

Both groups that were treated i.n showed relatively poor specific antibody responses in the first 7 weeks of the study. Mice treated i.n with silica-native GnRH-I displayed poor antibody responses throughout the study, with a peak A_{450} reading of 0.08 after 9 weeks. Whereas mice treated i.n with silica-BSA-native-GnRH-I displayed a small increase in specific antibody production after 9 weeks, with an A_{450} reading peaking at 0.49 (SD ± 0.03), which is still a relatively poor immune response.

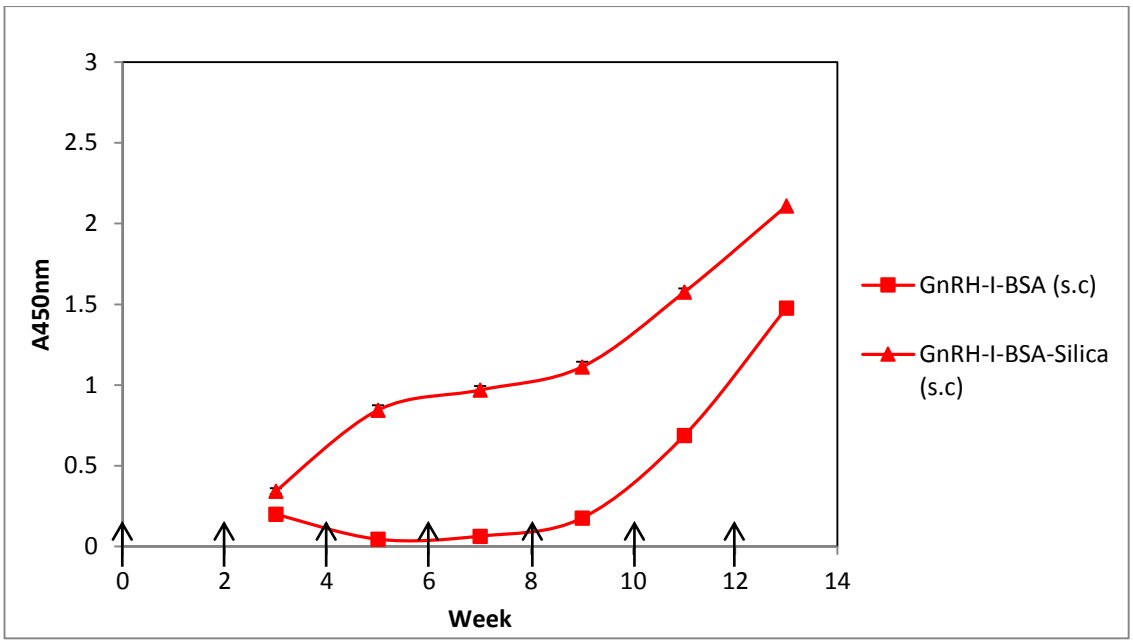

Graph 30: GnRH-I specific IgG response for animals immunised against native GnRH-I conjugated to BSA and with/without adsorption to silica. Immunisations were performed subcutaneously. The absorbance results were measured from ELISAs undertaken on OVA-GnRH-I coated plates. Each data point is the average of triplicate A450 readings with ±SD (n=5). Immunisations were administered subcutaneously in weeks 0, 2, 4, 6, 8, 10 and 12 (marked with arrows) with bloods taken a week after each injection.

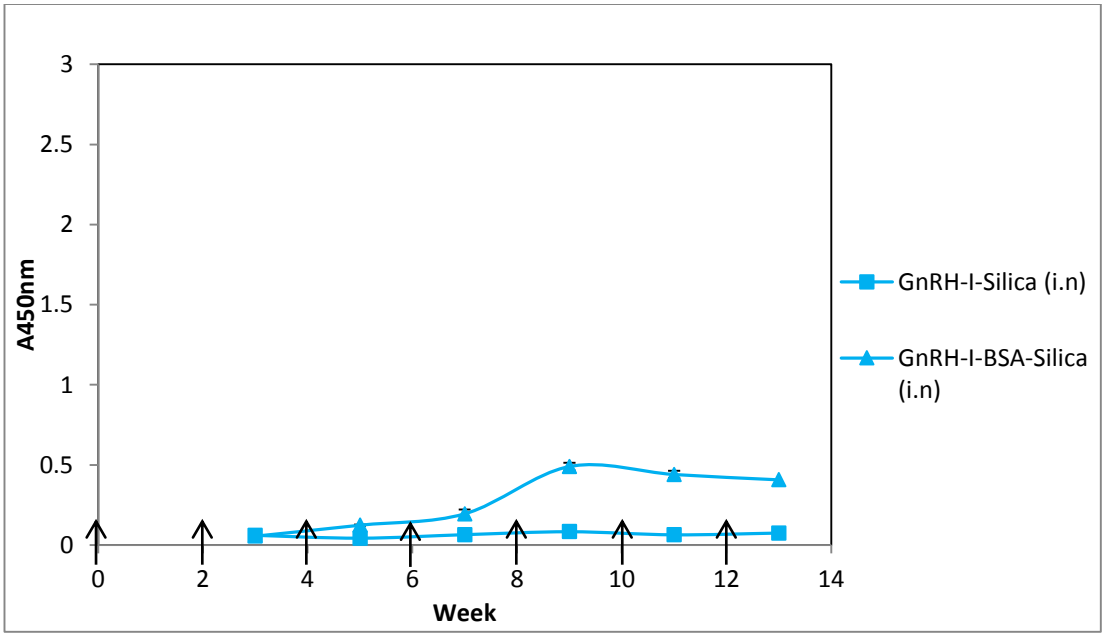

Graph 31: GnRH-I specific IgG response for animals immunised against native GnRH- with/without conjugation to BSA and adsorbed to silica. Immunisations were performed intranasally. The absorbance results were measured from ELISAs undertaken on OVA-GnRH-I coated plates. Each data point is the average of triplicate A450 readings with ±SD (n=5). Immunisations were administered i.n in weeks 0, 2, 4, 6, 8, 10 and 12 (marked with arrows) with bloods taken a week after each injection.

From Graph 32 it can be seen that those groups immunised with vaccine formulations including silica, BSA and either peptide exhibit the greatest specific IgG antibody response at the end of the study, with the silica-BSA-cys-GnRH-I conjugate showing the highest response (A_{450} reading of 2.59±0.26). Graph 32 also illustrates that vaccines formulations which consist of just peptides adsorbed on a silica surface alone show poor immunogenicity after a treatment period of 13 weeks.

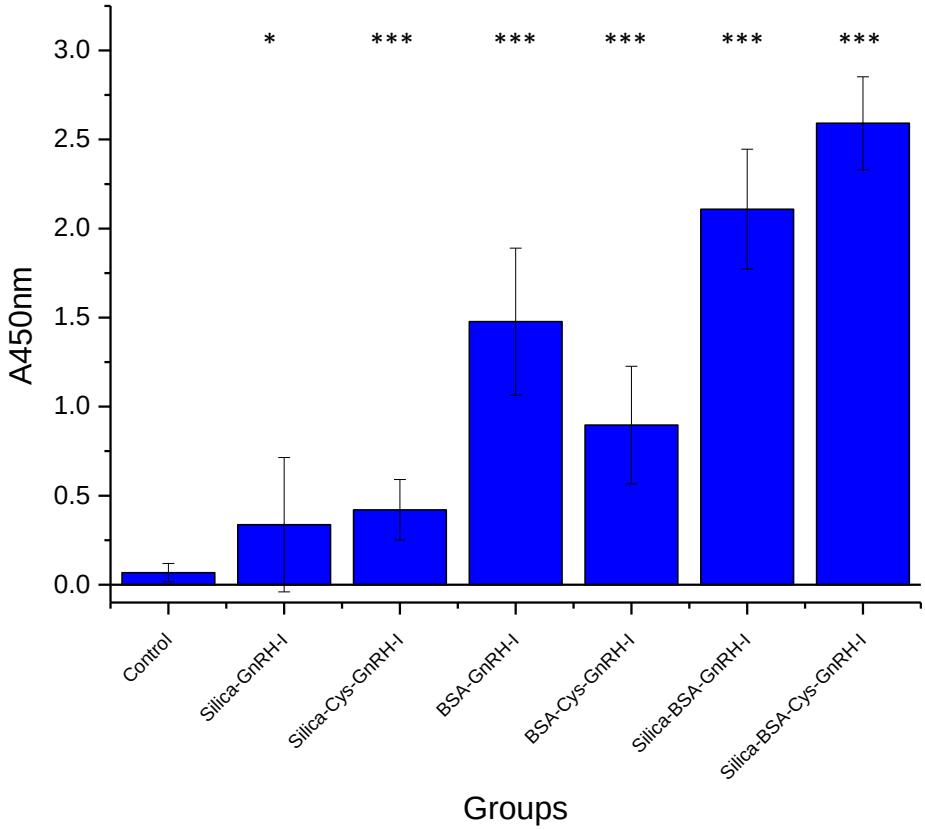

*Graph 32: GnRH-I specific IgG response for male BALB/c mice immunised against native GnRH-I and the modified analogue (Cys-GnRH-I), with/without conjugation to BSA and with/without adsorption to silica. Immunisations were performed subcutaneously. The absorbance results were measured from ELISAs undertaken on OVA-GnRH-I coated plates. Each column is the average of triplicate A450 readings with ±SD (n=5). These are the final specific IgG antibody levels at the end of the study after 13 weeks and are ordered in a manner which gives direct comparisons between each peptide. ***P < 0.001; *P < 0.25.*

Graph 33 further illustrates that silica-peptide vaccine formulations exhibit poor immunogenicity, with the cys-GnRH-I-silica variation proving to be slightly more effective at provoking an immune response in comparison to its native GnRH-I

counterpart. It can also be observed that the conjugation of GnRH peptide to BSA increases the effectiveness of the vaccine formulation, which can be enhanced further with the addition of silica as an adjuvant.

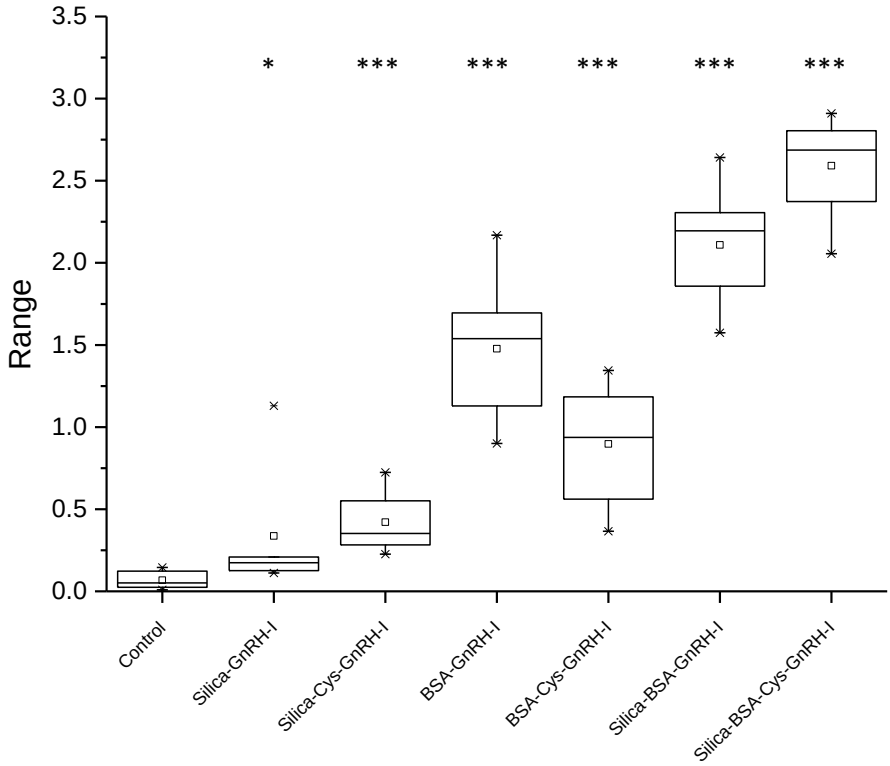

*Graph 33: GnRH-I specific IgG response for male BALC/C mice immunised against native GnRH-I and the modified analogue (Cys-GnRH-I), with/without conjugation to BSA and with/without adsorption to silica. Immunisations were performed subcutaneously. The absorbance results were measured from ELISAs undertaken on OVA-GnRH-I coated plates. Presented are boxplots of triplicate A450 readings for each group. These are the final specific IgG antibody levels at the end of the study after 13 weeks. ***P < 0.001; *P < 0.25.*

5.3.3 Testosterone

Two animal studies were run separately, with Groups II-V run first and Groups VI-IX (plus control group) performed after this study. All treatments administered produced a reduction in testosterone levels after 13 weeks as shown in Graph 34. In particular, immunisation with the native GnRH peptide directly adsorbed to the silica nanoparticle surface showed the greatest effect on reducing the average testosterone levels, with a decrease of ~9.5ng/ml (>95%) from that of the control group. Treatment with cys-GnRH-BSA exhibited the lowest reduction in testosterone levels after 13 weeks, but 7 weeks into the study, the testosterone reduction was greatest in this group. It could also be observed that mice treated with cys-GnRH-I-silica exhibited a dramatic reduction in testosterone between 7 and 13 weeks, with a reduction of 8.7ng/mL in this time period.

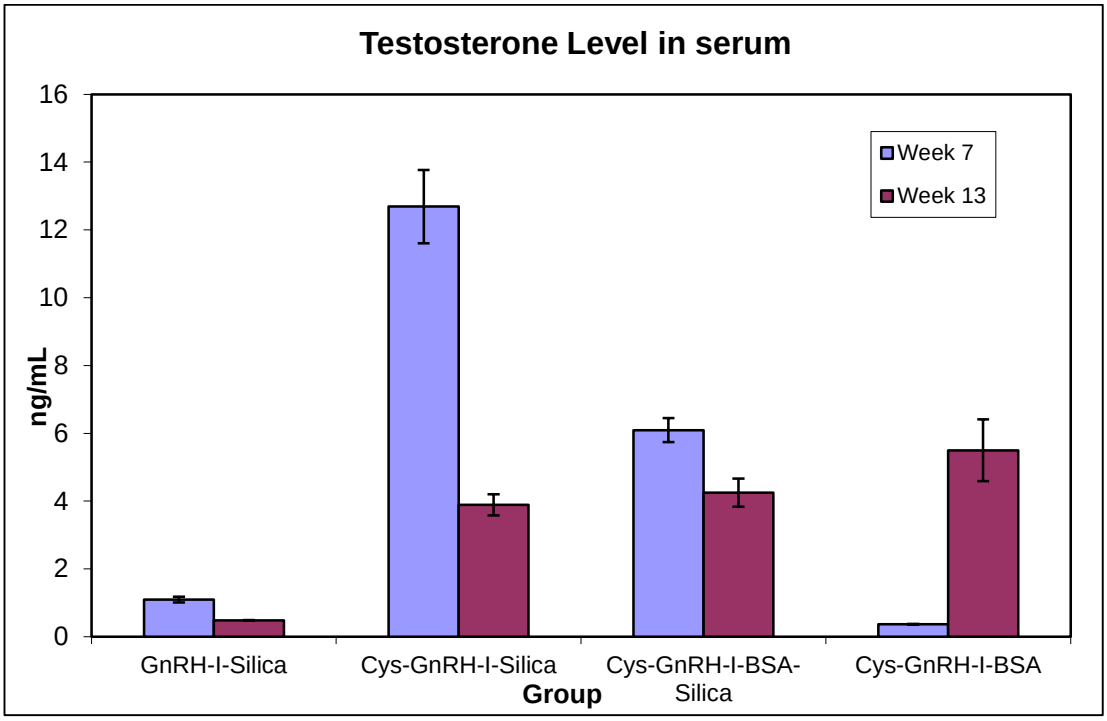

Graph 34: Testosterone levels in blood serum from animals immunised against GnRH-I and its modified analogue (cys-GnRH-I), with/without conjugation to BSA and with/without adsorption to silica. The testosterone levels were determined using a testosterone assay kits 7 and 13 weeks post treatment. Each point represents the mean of duplicate readings with ±SD (n=5).

Graph 35 clearly displays that there is a variation in the testosterone levels of all groups after 13 weeks of treatment. These boxplots show that there is a mean reduction in the testosterone levels of all groups except those mice treated with silica-cys-GnRH-I, which has a slightly higher level of testosterone than that of the control group. It is clear that groups treated with native GnRH-I (silica-native GnRH-I, BSA-native GnRH-I and silica-BSA-native GnRH-I) show a significant decline in testosterone production. Whereas those treated with formulations including the cys-GnRH-I peptide show a less dramatic effect on testosterone production. Graph 35 shows that treatments of BSA-cys-GnRH-I and silica-BSA-cys-GnRH-I show a mean reduction in testosterone from the control group. Mice treated with silica-cys-GnRH-I does not show a great change in testosterone levels from the control after 13 weeks.

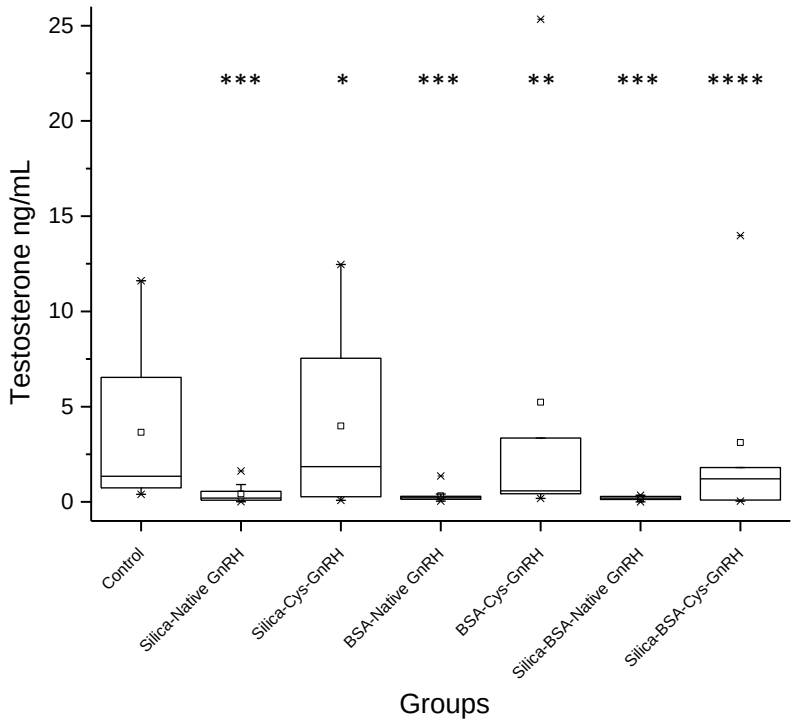

*Graph 35: Testosterone levels in blood serum from animals immunised against GnRH-I and its modified analogue (cys-GnRH-I), with/without conjugation to BSA and with/without adsorption to silica as specified. The testosterone levels were determined using a testosterone assay kits at the end of the study after 13 weeks. Presented are boxplots of duplicate readings. ***P < 0.001; *P < 0.25; **P < 0.6; ****P < 0.75.*

5.4 Discussion

It has already been found that GnRH-based vaccines can be formulated for both humans and animals. Examples include GnRH conjugated to keyhole limpet haemocyanin (KLH), which can induce infertility in female deer and GnRH vaccines using Alum as an adjuvant for use as an immunotherapy for fertility control and tumour growth (Miller *et al*., 2008; Talwar *et al*., 1997). Consequently, this study was undertaken in order to investigate the effects of silica as an adjuvant and if it could be used in such a way that it could cause the immune system to generate antibodies against 'self-peptides'.

In order for silica nanoparticles to be useful in a novel vaccine formulation, they need to display minimal cytotoxic effects *in vivo.* Figure 32 and Graph 27 shows that temperature sterilised Stöber silica nanoparticles is consistently non-toxic at concentrations up to at least 0.2g/mL silica. Stöber nanoparticles that were not temperature sterilised are consistently non-toxic up to, and including, a concentration of 0.1g/mL. Concentrations of 0.01g/mL were used in each dose used for animal immunisation. As such, the use of Stöber silica was likely to have minimal cytotoxic effects in this study.

Silica nanoparticles smaller than 200nm have been shown to display increased cytotoxic properties, with detrimental effects on the respiratory system reported and other associated issues (Han *et al.*, 2011). This is due to their increased surface area which would have a greater weight ratio of surface silanol groups. These exposed silanol groups generate reactive oxygen species, which promote cytotoxic effects. The silica nanoparticles in this work were approximately 200nm in size (chapter 4, Figure 11). These particles would be excreted from the body through the

waste system, however, smaller silica nanoparticles (<45nm) are renally filtered and would therefore have associated toxic effects (Mody *et al.,* 2013). The negative surface charge of the Stöber nanoparticles used also adds to the improved biocompatibility of Stöber silica as these particles are less likely to aggregate, thus reducing the likelihood of large aggregates forming, which can have cytotoxic effects on biosystems (Chen *et al.,* 2015).

Native GnRH-I and cys-GnRH-I peptides adsorbed straight onto silica nanoparticles were generally poor at eliciting an effective immune response with peak mean A_{450} values of ~0.64 for each during 13 weeks of treatment by subcutaneous vaccination. From the QCM results previously undertaken (chapter 4, Figure 14) it can be seen that the native GnRH-I peptide does not effectively adsorb onto the silica surface, which could explain why this formulation is not useful in immunisation studies. From simulation studies and QCM measurement (section 3.3.4; section 4.3.7), it was observed that the cys-GnRH-I peptide managed to effectively bind to the silica surface. However, the formation of a monolayer of this peptide on the surface may not be conducive to efficient peptide presentation to the surrounding environment. Whereas, a BSA-cys-GnRH-I conjugate does effectively present the peptide to the surrounding solvent (chapter 4, figure 30). QCM measurements clearly show that BSA-peptide conjugates adhere to silica surfaces effectively (section 4.3.9). This could be due to the protein 'depot' effect, which prevents large proteins from being released as easily from the silica nanoparticle. In turn, this would allow ample time for antigen presentation to the immune system with the inclusion of silica as an adjuvant (Wang *et al.,* 2012).

Conjugation to BSA was used as previous studies show that conjugation of 'self-peptides' to large carrier proteins can significantly reduce testosterone production and spermatogenesis in male mice (Khan *et al*., 2007). However, treatment using GnRH-I-carrier protein conjugates without the presence of an adjuvant have not been successful in eliciting a significant specific antibody response (Mann *et al*., 2006; Ferro *et al*., 1998). In this study treatment with both GnRH-I analogues adsorbed on the silica adjuvant alone show a similar specific GnRH-I IgG response, with antibody concentrations peaking at approximately 0.6 (A_{450}). However, groups treated with cys-GnRH-I conjugated to BSA appeared to show a higher specific IgG response than those groups that received treatment without the peptide-carrier protein conjugate (peak A_{450} of ~1.47 – native GnRH-I-BSA conjugate after 13 weeks). The addition of the silica adjuvant to this cys-GnRH-I conjugate showed a significant increase of specific IgG antibody levels, resulting in a final A_{450} of ~2.6 – over 250% higher than any other treatment group. As such, these results show that peptide conjugation to BSA along with adsorption to silica induces a high antigen-specific immune response. This suggests that the use of silica as an adjuvant may enhance the immunogenicity of 'self-peptides' and combination with a carrier protein shows a marked increase in specific IgG antibody response as this may invoke an increased T-cell response (Skrastina *et al*., 2014). This may be due to the increased surface interactions between the BSA molecule and the silica surface allowing more efficient adsorption and thus allowing the conjugated GnRH-I peptides more freedom to present themselves to the surrounding environment to be targeted by T-cells.

From the results presented in Graph 31 it can be clearly observed that treatments administered nasally are ineffective in provoking a specific antibody response. In each dose 50µg of peptide was used, which was effective in previous studies by Gebril *et al* (2014). However, in their study xanthan gum and non-ionic surfactant vesicles (NISV) were deployed as delivery systems. The results from Graph 31 suggests that silica and BSA may not be effective in delivery systems that are administered via nasal route.

Graphs 34 and 35 illustrate that the hormonal response from treated groups do not correlate well with the antibody response. All groups displayed an overall mean reduction in testosterone levels after 13 weeks, except from mice treated with silica-cys-GnRH-I, which had a slightly greater level of testosterone than the control group. This may be due to the pulsatile nature of testosterone release, which would result in variations of physiological hormone levels (Khan *et al.*, 2007). The most striking feature of the final hormone analysis is that all groups that were treated with a formulation that included the native GnRH-I peptide displayed a mass decrease in testosterone levels, whereas those groups treated using the cys-GnRH-I peptide showed a less marked variation in hormone levels. The exact cause of this is unknown, but it could be down to the native peptide binding with the GnRH receptor and then being blocked with the associated silica nanoparticle or attached BSA protein, thus preventing further GnRH binding to the receptor and stopping the hormonal cascade which results from this.

However, the cys-GnRH-I peptide may not bind to the GnRH receptor as efficiently, or this binding may be reversible, hence the reduced effect of cys-GnRH-I immunisation on testosterone levels. The cause of this receptor binding inefficiency

may be due to the substitution of the charged glutamic acid residue for a neutral cysteine residue, which could slightly alter the secondary structure of the peptide, thus affect its receptor binding efficacy. There was a flare in the testosterone levels after 7 weeks of treatment with cys-GnRH-silica, but this was resolved after 13 weeks of treatment back to control levels (section 5.3.3, Graph 34). Similar flares have been observed in treatment with other GnRH analogues, but these peptides retained the native terminal residues and overall charge of the native peptide and ultimately reduced testosterone production (Parmar *et al.,* 1987). The difference in the native and cys-GnRH-I peptides is clear to see in the adsorption simulations of each peptide and their adsorbed conformations (sections 3.3.1, 3.3.4 and Figure 33 below). From Figure 33 it can clearly be observed that the native GnRH-I is collapsed on the silica surface, whereas the cys-GnRH-I is 'standing', with the C-terminus exposed to solution. However, the presentation of these peptides on the silica surface may influence the efficiency of receptor blocking. The native GnRH-I peptide is anchored by the positively charged arginine residue, and as such the termini may have more freedom to interact with the surrounding environment and participate in receptor binding. Whereas, the cys-GnRH-I peptide is adsorbed to the silica surface via the N-terminal, with the C-terminal exposed to solution. As a result, the N-terminus is unlikely to be able to be involved in receptor binding, thus the GnRH receptor is less likely to be blocked by a formulation using silica-cys-GnRH-I.

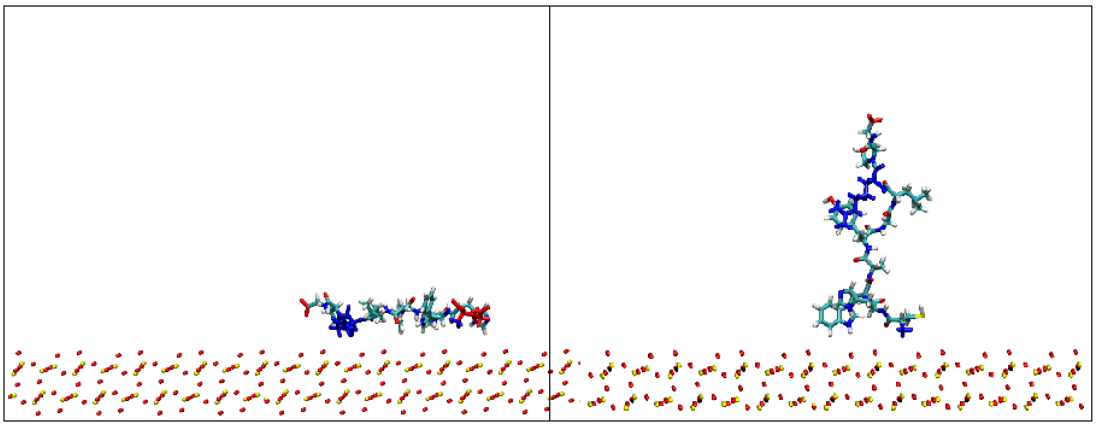

Figure 33: GnRH-I (left) and cys-GnRH-I (right) adsorbed to a silica surface with charged residues highlighted (red = negative; blue = positive). Native GnRH-I is collapsed on the surface, whereas cys-GnRH-I is 'standing' exposed to the solution.

Chapter 6 - Conclusion

In the past 200 years, billions of vaccinations have been administered, leading to the prevention, and in some cases the eradication, of various debilitating infectious diseases in many parts of the world (Zhu *et al.,* 2014). Many vaccines have been formulated by attenuating a pathogen and exposing a subject to the attenuated virus (or bacterium), thus allowing the host to build an immune response against the pathogenic antigen without contracting the associated disease (The National Institute of Allergy and Infectious Diseases, 2013). However, vaccines can also be synthesised using non-pathogenic vectors. Non-pathogenic vectors are advantageous as they mimic the natural course of infection and therefore may be able to produce a similar immune response to live vaccines. However, live vaccines can occasionally revert back to a harmful state once inside a host cell. Non-pathogenic vectors are unable to replicate inside target cells and are removed from the body after only a few days, thus making non-pathogenic vaccines safer than live vaccines (Bolhassani, A *et al.,* 2012). Other types of non-pathogenic vaccines involve immunising against self-peptides, which can be utilised to treat many conditions, such as prostate cancer or to induce a contraceptive effect (Pham *et al.,* 2016; Herbert *et al.,* 2005).

In this work, vaccines against GnRH-I were produced using native GnRH-I and cys-GnRH-I as model antigens. GnRH-I is a decapeptide produced in the hypothalamus that effectively regulates fertility in mammals (see section 1.2.1) (Roch *et al.,* 2011). However, as GnRH-I is a self-peptide it needs to be attached to a large carrier molecule or adjuvant in order to elicit an immune response (Herbert *et al.,* 2005). One of the main adjuvants used in current vaccinations is aluminium oxyhydroxide (alum). Using alum as an adjuvant can help induce a strong antibody response against an antigen as it remains at the site of injection, allowing DCs more

time for antigen uptake and thus subsequent production of specific antibodies (Mody *et al.,* 2013). However, alum is known to cause pain and inflammation at the site of administration and has even been shown to accumulate in the brain (Skrastina *et al.,* 2014; Gherardi *et al.,* 2015). In this study nanoparticulate silica has been used as an adjuvant for GnRH-I. Silica nanoparticles show good biocompatibility and are chemically stable (Du *et al*, 2010; Nozawa *et al*, 2005). Silica nanoparticles greater than 200nm in diameter also show particularly low cytotoxicity (Han *et al*, 2011).

Male BALB/c mice were immunised subcutaneously with native GnRH-I and cys-GnRH-I using Stöber silica nanoparticles as an adjuvant. Over a study period of 13 weeks it was found that mice treated with GnRH-I peptide adsorbed directly onto a silica nanoparticle did not exhibit a strong specific IgG antibody response against the GnRH-I antigen (chapter 5, Graph 28), although both were slightly higher than that of the control group. From QCM surface adsorption experiments it was apparent that the native GnRH-I peptide does not adsorb directly onto silica very effectively, however the cys-GnRH-I peptide did (Section 4.3.8). This was most likely due to the charged residues present on each peptide. The native peptide overall carried a neutral charge, however the cys-GnRH-I peptide was positively charged overall as the negative glutamic acid residue had been replaced with the neutral cysteine. As such, the cys-GnRH-I peptide was more likely to adsorb effectively on the negative silica surface (surface charge of approximately -50mV as found by zeta potential measurements [chapter 4, Graph 13]. From these results it could be surmised that the cys-GnRH-I peptide on silica should be more effective at interacting with the surrounding physiological environment, thus eliciting an immune response. However, the manner in which the peptide is presented to the immune cells is crucial

in eliciting a specific antibody response (Mody *et al.,* 2013). From molecular dynamics simulations it can be noted that the native GnRH-I peptide effectively collapses on the silica surface (Chapter 3, Figure 13), whereas the cys-GnRH-I peptide is able to 'stand' on the surface, anchored by the terminal cysteine residue. From the outset, the cys-GnRH-I peptide looks as though it is presented to the surrounding environment more effectively than the native peptide. However, the secondary structure of the peptide is of great importance to its associated biological behaviour (Millar, 2005). GnRH-I should be in a hairpin loop conformation, this is not apparent in the adsorption simulation of cys-GnRH-I peptide on the silica surface as they peptide has somewhat straightened out. This could be due to the inherent electric field present at the silica surface, causing the dipole moment of the cys-peptide to align and lose its hairpin loop conformation.

However, the native peptide retains its hairpin loop conformation once adhered to the silica surface. This may help explain the change in testosterone levels of treated mice after 13 weeks. It was observed that mice treated with silica-native GnRH-I showed a significant decline in testosterone production, whereas mice treated with silica-cys-GnRH-I did not display a great change in testosterone levels from the control group (Chapter 5, Graph 35). On binding to the GnRH receptor, the GnRH peptide adopts a hairpin loop conformation with both termini heavily involved with receptor binding (Millar, 2005). The native GnRH-I peptide not only retains a hairpin loop conformation, but both termini may be available to bind to the receptor as C-terminal is negatively charged, therefore will not be strongly bound to the silica surface and although the N-terminal is positively charged, the terminal residue (glutamic acid) carries a negative charge, allowing the N-terminal some freedom

from the surface. Once bound to the GnRH receptor the silica nanoparticle attached to the peptide may block the receptor from further binding to free GnRH peptides, thus effecting a drop in testosterone production as the hormonal cascade would be halted (Chapter 1, section 1.2.1). The cys-GnRH-I-silica formulation would not be able to effectively interact with the GnRH receptor due to the loss of the hairpin loop conformation and also because the N-terminal would be unavailable to interact with the receptor, due to being adsorbed on the silica surface. Consequently the silica would be unable to block the receptor and testosterone production would continue as normal.

Another method to increase the immunogenicity of a self-peptide is to attach it to a large biomolecule as a carrier protein, such as BSA or ovalbumin (Saenz *et al.,* 2009; Geary *et al.,* 2006). The addition of BSA to silica also increases the biocompatibility of the silica adjuvant (Lim *et al.,* 2012). In order to evoke an effective specific antibody response to GnRH-I, the native and cys-GnRH-I peptides were conjugated to BSA carrier molecules via the EDC reaction (section 4.2.2). Male BALB/c mice were immunised with these conjugates over a period of 13 weeks and a much higher specific IgG antibody response was observed for both peptide conjugates than those of the peptides adsorbed directly onto silica (native – 1.48 to 0.34; cys – 0.90 to 0.42 A_{450} levels) (chapter 5, Graph 32). The increased antibody levels may be due to both peptides being free to interact with the physiological environment, whilst also retaining their hairpin loop secondary protein structure. Molecular dynamics simulations illustrated that bound cys-GnRH-I peptides to a BSA monomer could be exposed to the surrounding solution in such a way that their secondary structure is retained (Chapter 4, figure 30). However, from the same

simulation it was also apparent that not all conjugated peptides are available to interact with the surrounding solvent. There is also no great associated electric field on the surface of the BSA protein, thus the bound GnRH peptides would be able to retain their hairpin loop conformation more easily.

Mice treated with the native GnRH-I-BSA conjugate also showed a dramatic decrease in testosterone production in comparison to the control group (Chapter 5, Graph 35). In comparison, those mice treated with the cys-GnRH-I- BSA conjugate showed a much smaller decline in testosterone production. As per the native peptide adsorbed directly onto the silica nanoparticle, this could be down to the BSA blocking the GnRH receptor once the native peptide binds, halting testosterone production. Whereas the cys-GnRH-I-BSA conjugate is unable to effectively block the GnRH receptor as the cys-peptide may not be able to bind properly to the receptor due to the substituted cysteine N-terminal residue. This substitution alters the charge at the terminal, which may greatly affect its GnRH receptor binding ability.

As BSA increases the biocompatibility of silica, male BALB/c mice were also treated with native and cys-GnRH-I-BSA conjugates adsorbed on silica nanoparticles as an adjuvant (Lim *et al.*, 2012). Both of these groups saw an increase in the specific antibody levels after 13 weeks (Chapter 5, Graphs 29 and 30) over other groups (A_{450} readings of 2.11 and 2.59 for native and cys peptides respectively). This clearly shows that the addition of silica to the vaccine formulations has increased the immunogenicity of the self-peptide, thus eliciting a greater specific IgG antibody response. The addition of silica has possibly increased the half-life of the peptide *in vivo*, allowing more efficient uptake of the GnRH

antigen to DCs and antigen presenting cells (Penchala *et al.,* 2015). As such, an effective T-cell response was elicited, rather than an inflammatory response, thus allowing effective immunisation to occur. However, once again mice treated with the native peptide vaccine formulation showed a mass decline in testosterone production, whereas those mice treated with cys-GnRH-BSA-silica displayed a smaller decrease in testosterone production. These hormonal responses are probably due to peptide termini presentation and residue substitution as described previously.

To increase the knowledge of this study further molecular dynamics simulations could be performed with an increased amount of peptides conjugated to the BSA monomer and also with the native GnRH-I peptide conjugated to the monomer. This would provide further insight into how each peptide is presented to the surrounding environment when bound to BSA and the likelihood of peptides retaining their hairpin loop secondary structure. This would be beneficial for further studies as the secondary structure of proteins is crucial to their *in vivo* behaviour and can determine whether they can interact with their associated receptors. Similar work using MD simulations has been undertaken by Pal *et al.* (2016) to investigate the thermodynamic binding of the neurotransmitter gamma-aminobutyric acid with BSA. Histological analysis of the mice used in the study could also be carried out. In particular, analysis of the testes would provide information on the effects of the various treatments on testosterone production by analysing how many sperm cells are produced. Furthermore, GnRH receptor studies could also be undertaken in order to further understand how the various treatments used interact with, and affect, receptor activation (Naor, 2009).

Bibliography

Allen, MP; Tildesley, DJ., "Computer Simulation of Liquids". *Clarendon Press – Oxford University Press,* Published 1987.

Atkins, P; De Paula, J., "Atkins' Physical Chemistry". *Oxford University Press,* Published 2006.

Barbieri, RL., "Clinical applications of GnRH and its analogues"., *Trends in Endocrinology & Metabolism,* 1992, **3(1),** 30-34.

Baxby, D., "Edward Jenner's Inquiry: a bicentenary analysis". *Vaccine,* **1999,** 17, 301-307.

Bergmann-Leitner, ES; Leitner, WW., "Danger, death and DNA vaccines"., *Microbes and Infection,* 2004, **6,** 319-327.

Blumen, SR; Cheng, K; Ramos-Nino, ME; Taatjes, DJ; Weiss, D; Landry, CC; Mossman, BT., "Unique mechanisms of uptake of acid-prepared mesoporous spheres (APMS) by lung epithelial and mesothelioma cells". *Am. J. Respir. Cell Mol. Biology*, 2006**, 36**, 333-342.

Bolhassani, A; Zahedifard, F., "Therapeutic live vaccines as a potential anticancer strategy"., *International Journal of Cancer,* 2012, **131,** 1733-1743.

Chen, G; Teng, Z; Su, X; Liu, Y; Lu, G., "Unique biological degradation behavior of Stöber mesoporous silica nanoparticles from their interiors to their exteriors"., *Journal of biomedical nanotechnology,* 2015, **11,** 722-729.

Chen, WH; Cohen, MB; Kirkpatrick, BD; Brady, RC; Galloway, D; Gurwith, M; Hall, RH; Kessler, RA; Lock, M; Haney, D; Lyon, CE; Pasetti, MF; Simon, JK;

Szabo, F; Tennant, S; Levine, MM., "Single-dose live oral cholera vaccine CVD 103-HgR protects against human experimental infection with vibrio cholera O1 El Tor"., *Clinical Infectious Diseases,* 2016, **62 (11),** 1329-1335.

Coffman, RL; Sher, A; Seder, RA., "Vaccine adjuvants: putting innate immunity to work"., *Immunity*, 2010, **33(4),** 492-503.

Du, X; He, J., "Fine-tuning of silica nanosphere structure by simple regulation of the volume ratio of cosolvents"., *Langmuir*, 2010, **26**, 10057–10062.

Ellis, RW., "Technologies for the design, discovery, formulation and administration of vaccines"., *Vaccine,* 2001, **19,** 2681-2687.

Euston, S., "Molecular dynamics simulation of protein adsorption at fluid interfaces: A comparison of all-atom and coarse-grained models"., *Biomacromolecules,* 2010, **11,** 2781-2787.

Ferro, VA; Stimson, WH., "Investigation into suitable carrier molecules for use in an anti-gonadotrophin releasing hormone vaccine". *Vaccine,* 1998, **16**, 1095-102.

Ferro, V.A; Costa, R; Carter, K.C; Harvey, M.J.A; Waterston, M.M; Mullen, A.B; Matschke, C; Mann, J.F.S; Colston, A; Stimson, W.H., "Immune responses to a GnRH-based anti-fertility immunogen, induced by different adjuvants and subsequent effect on vaccine efficacy"., *Vaccine*, 2004, **22,** 1024-1031.

Foged, C., "Subunit vaccines of the future: the need for safe, customized and optimized particulate delivery systems"., *Therapeutic Delivery,* 2011, **2,** 1057-1077.

Forester, TR; Smith, W., "SHAKE, Rattle, and Roll: Efficient constraint algorithms for linked rigid bodies"., *Journal of Computational Chemistry*, 1998, **19 (1),** 102-111.

Freund, J; Casals, J; Hosmer E., "Sensitization and antibody formation after injection of tubercle bacili and parafin oil"., *Proc Soc Exp Biol Med*, 1937, **37**, 509–513.

Friedman, R., "Nano dot technology enters clinical trials"., *Journal of the National Cancer Institute,* 2011, **103,** 1428-1429.

Garside, D.A; Gebril, A; Nimmo, N; Alsaadi, M; Mullen, A.B; Ferro, V.A., "An Update on Developments in Female Hormonal Contraception"., *Current Women's Health Reviews,* 2012, **8,** 276-288.

Geary, TW; Grings, EE; MacNeil, MD; de Avila, DM; Reeves, JJ., "Use of recombinant gonadotropin-releasing hormone antigens for immunosterilization of beef heifers"., *Journal of Animal Science*, 2006, **84,** 343-350.

Gebril, AM; Lamprou, DA; Alsaadi, MM; Stimson, WH; Mullen, AB; Ferro, VA., "Assessment of the antigen-specific antibody response induced by mucosal administration of a GnRH conjugate entrapped in lipid nanoparticles". *Nanomedicine*, **2014,** 10, 971-979.

Gennari, M; Bouthillier, Y; Ibanez, OM; Ferreira, VCA; Mevel, JC; Reis, MH; Piatti, RM; Ribeiro, OG; Biozzi, G., "Effect of silica on the genetic-regulation of antibody responsiveness"., *Annales de l Institut Pasteur-Immunology*, 1987, **138,** 359-370.

Gherardi, RK; Eidi, H; Crepeaux, G; Authier, FJ; Cadusseau, J., "Biopersistence and brain translocation of aluminium adjuvants of vaccines"., *Frontiers in Neurology,* 2015, **6(4),** 1-8.

Halstead, SB; Thomas, SJ., "New Japanese encephalitis vaccines: alternatives to production in mouse brain"., *Expert Review of Vaccines*, 2011, **10(3)**, 355-364.

Han, B; Guo, J; Abrahaley, T; Qin, L; Wang, L; Zheng, Y; Li, B; Liu, D; Yao, H; Yang, J; Li, C; Xi, Z; Yang, X., "Adverse effect of nano-silicon dioxide on lung function of rats with or without ovalbumin immunization". *PLoS One,* 2011**, 6(2)**, e17236.

Hartono, SB; Gu, W; Kleitz, F; Liu, J; He, L; Middelberg, APJ; Yu, C; Lu, GQ; Q, SZ., "Poly-L-lysine functionalized large pore cubic mesostructured silica nanoparticles as biocompatible carriers for gene delivery"., *American Chemical Society,* 2012, **6(3),** 2104-2117.

Herbert, C.A; Trigg, T.E., "Applications of GnRH in the control and management of fertility in female animals"., *Animal Reproduction Science,* 2005, **88,** 141-153.

Hosseinzadeh, S; Bolhassani, A; Rafati, S; Taheri, T; Zahedifard, F; Daemi, A; Taslimi, Y; Hashemi, M; Memamejadian, A., "A non-pathogenic live vector as an efficient delivery system in vaccine design for the prevention of HPV16 E7-overexpressing cancers"., *Drug Delivery*, 2013, **20(3-4),** 190-198.

Humphrey, W; Dalke, A; Schulten, K., "MD: Visual Molecular Dynamics", *Journal of Molecular Graphics,* **1996,** 14, 33-38.

Huygen, K., "Plasmid DNA vaccination"., *Microbes and Infection*, 2005, **7(5-6),** 932-938.

Jachimska, B; Lapczynska, M; Zapotoczny, S., "Reversible swelling process of sixth-generation poly(amido amine) dendrimers molecule as determined by quartz crystal microbalance technique"., *Journal of Physical Chemistry C*, 2012, **117,** 1136-1145.

Jacob, NT; Lockner, JW; Schlosburg, JE; Ellis, BA; Eubanks, LM; Janda, KD., "Investigations of enantiopure nicotine haptens using an adjuvanting carrier in anti-nicotine vaccine development"., *Journal of Medicinal Chemistry,* 2016, **59,** 2523-2529.

Janeway, CA Jr., "Immunobiology (5th edition)"., *Garland Publishing*, Published 2001.

Jardon-Valadez, E; Aguilar-Rojas, A; Maya-Nunez, G; Leanos-Miranda, A; Pinerio, A; Conn, PM; Ulloa-Aguirre, A., "Conformational effects of Lys191 in the human GnRH receptor: mutagenesis and molecular dynamics simulations studies"., *Journal of Endocrinology,* 2009, **201,** 297-307.

Jenner, Edward., "An Inquiry Into the Causes and Effects of the Variolae Vaccinae: A Disease Discovered in Some of the Western Counties of England, Particularly Gloucestershire, and Known by the Name of the Cow Pox"., *London,* Published 1798.

Jorgensen, WL; Chandrasekhar, J; Madura, JD; Impey, RW; Klein, ML., "Comparison of simple potential functions for simulating liquid water". *Journal of Chemical Physics*, 1983, **79,** 926-935.

Kauffman, AS., "Emerging functions of gonadotropin-releasing hormone II in mammalian physiology and behaviour"., *Journal of Neuroendocrinology*, 2004, **16,** 794-806.

Khan, MAH; Prevost, M; Waterston, MM; Harvey, MJA; Ferro, VA., "Effect of immunisation against gonadotrophin releasing hormone isoforms (mammalian GnRH-I, chicken GnRH-II and lamprey GnRH-III) on murine spermatogenesis"., *Vaccine*, 2007, **25,** 2051-2063.

Kim, IY; Joachim, E; Choi, H; Kim, K., "Toxicity of silica nanoparticles depends on size, dose, and cell type"., *Nanomedicine*, 2015, **11(6),** 1407-1416.

Krugman, S; Giles, JP; Jacobs, AM; Friedman, H., "Studies with live attenuated measles virus vaccine"., *American Journal Public Health*, 1962, **52,** 16-28.

Kubiak-Ossowska, K; Mulheran, P., "Protein diffusion and long-term adsorption states at charged solid surfaces"., *Langmuir*, 2012, **28,** 15577-15585.

Kubiak-Ossowsak, K; Burley, G; Patwardhan, SV; Mulheran, PA., "Spontaneous membrane –translocating peptide adsorption at silica surfaces: A molecular dynamics study"., *The Journal of Physical Chemistry B*, 2013, **117,** 14666-14675.

Kubiak-Ossowska, K; Cwieka, M; Kaczynska, A; Jachimska, B; Mulheran, P., "Lysozyme adsorption at a silica surface using simulation and experiment: effects of pH on protein layer structure"., *Phys Chem Chem Phys*, 2015, **17(37),** 24070-24077.

Kutzler, MA; Weiner, DB., " DNA Vaccines: ready for prime time?"., *Nature Reviews Genetics,* 2015, **9(10),** 776-788.

Levy, JK; Miller, LA; Crawford, PC; Ritchey, JW; Ross, MK; Fagerstone, KA., "GnRH immunocontraception of male cats"., *Theriogenology,* 2004, **62,** 1116-1130.

Levy, J.K; Friary, J.A; Miller, L.A; Tucker, S.J; Fagerstone, K.A., "Long-term fertility control in female cats with GonaCon™, a GnRH immunocontraceptive"., *Theriogenology,* 2011, **76,** 1517-1525.

Lim, JS; Lee, K; Choi, JN; Hwang, YK; Yun, MY; Kim, HJ; Won, YS; Kim, SJ; Kwon, H; Huh, S., "Intracellular protein delivery by hollow mesoporous silica capsules with a large surface hole"., *Nanotechnology,* 2012, **23,** 085101.

Lin, YS; Haynes, CL., "Impacts of mesoporous silica nanoparticle size, pore ordering, and pore integrity on hemolytic activity"., *Journal of American Chemical Society,* 2010, **132(13),** 4834-4842.

Majorek, KA; Porebski, PJ; Chruszcz, M; Almo, SC; Minor, W., "Structural and immunologic characterization of bovine, horse and rabbit serum albumins"., *Molecular Immunology,* 2012, **52,** 174-182.

Mann, JF; Scales, HE; Shakir, E; Alexander, J; Carter, KC; Mullen, AB., "Oral delivery of tetanus toxoid using vesicles containing bile salts (bilosomes) induces significant systemic and mucosal immunity"., *Methods,* 2006, **38**, 90-95.

Maassab, HF., "Adaptation and growth characteristics of influenza virus at 25 degrees C"., *Nature,* 1967, **213 (5076),** 612-614.

Matsuo, H; Baba, Y; Nair, RMG; Arimura, A; Schally, AV., "Structure of the porcine LH- and FSH-releasing hormone. I. The proposed amino acid sequence"., *Biochemical and Biophysical Research Communications,* 1971, **43(6),** 1334-1339.

Mbow, ML; De Gregorio, E; Valiante, NM; Rappuoli, R., "New adjuvants for human vaccines"., *Curr Opin Immunol,* 2010, **22(3),** 411-416.

McCluskie, MJ; Davis, HL., "Mucosal immunization with DNA vaccines" *Microbes and Infection,* 1999, **1(9),** 685-698.

Mercuri, LP; Carvalho, LV; Lima, FA; Quayle, C; Fantini, MC; Tanaka, GS; Cabrera, WH; Furtado, MF; Tambourgi, DV; Matos Jdo, R; Jaroniec, M; Sant'Anna, OA., "Ordered mesoporous silica SBA-15: A new effective adjuvant to induce antibody response"., *Small,* 2006**, 2,** 254-256.

Millar, R.P., "GnRHs and GnRH receptors"., *Animal Reproduction Science,* 2005, **88,** 5-28.

Miller, LA., Gionfriddo, JP; Fagerstone, KA; Rhyan, JC; Killian, GJ., "The single-shot GnRH immunocontraceptive vaccine (GonaCon) in white-tailed deer: comparison of several GnRH preparations"., *American Journal Reproductive Immunology,* 2008, **60 (3),** 214-223.

Mody, KT; Popat, A; Mahony, D; Cavallaro, AS; Yu, C; Mitter, N., "Mesoporous silica nanoparticles as antigen carriers and adjuvants for vaccine delivery"., *Nanoscale,* 2013, **5,** 5167-5179.

Morga, M; Adamczyk, Z; Kosior, D., "Silica monolayer formation and stability determined by *in situ* streaming potential measurements"., *Electrochimica Acta,* 2016, **206,** 409-418.

Mulheran, PA; Connell, DJ; Kubiak-Ossowska, K., "Steering protein adsorption at charged surfaces: Electric fields and ionic screening"., *RSC Advances,* 2016, **6,** 73709.

Naor, Z., "Signaling by G-protein-coupled receptor (GPCR): Studies on the GnRH receptor"., *Frontiers in Neuroendocrinology,* 2009, **30,** 10-29.

The National Institute of Allergy and Infectious Diseases (NIAID). (July 23, 2013). *Types of Vaccines.* Retrieved July 14, 2016 from http://www.vaccines.gov/more_info/types/.

Nayak, S; Herzog, RW., "Progress and Prospects: Immune responses to viral vectors"., *Gene Therapy,* 2010, **17(3),** 295-304.

Nozawa, K; Gailhanou, H; Raison, L; Panizza, P; Ushiki, H; Sellier, E; Delville, JP; Delville, MH., "Smart Control of Monodisperse Stöber Silica Particles: Effect of Reactant Addition Rate on Growth Process"., *Langmuir,* 2005, **21,** 1516-1523.

Pal, U; Pramanik, SK; Bhattacharya, B; Banerji, B; Maiti, NC., "Binding interaction of a gamma-aminobutyric acid derivate with serum albumin: an insight by fluorescence and molecular modelling analysis"., *SpringerPlus,* 2016, **5(1),** 1121.

Pandey, A; Singh, N; Vemula, SV; Couëtil, L; Katz, JM; Donis, R; Sambhara, S; Mittal, SK., "Impact of pre-existing adenovirus vector immunity on immunogenicity

and protection conferred with an adenovirus-based H5N1 influenza vaccine"., *PLoS One,* 2012, **7(3),** e33428.

Parmar, H; Edwards, L; Phillips, RH; Allen, L; Lightman, SL., "Orchiectomy versus long-acting D-Trp-6-LHRH in advanced prostatic cancer"., *British Journal of Urology,* 1987, **59(3),** 248-254.

Patwardhan, SV; Emami, FS; Berry, RJ; Jones, SE; Naik, RR; Deschaume, O; Heinz, H; Perry, CC., "Chemistry of Aqueous Silica Nanoparticle Surfaces and the Mechanism of Selective Peptide Adsorption"., *Journal of American Chemical Society*, **2012,** 134, 6244-6256.

Penchala, SC; Miller, MR; Pal, A; Dong, J; Madadi, NR; Xie, J; Joo, H; Tsai, J; Batoon, P; Samoshin, V; Franz, A; Cox, T; Miles, J; Chan, WK; Park, MS; Alhamadsheh, MM., "A biomimetic approach for enhancing the *in vivo* half-life of peptides"., *Nature Chemical Biology,* 2015**, 11**, 793-798.

Pham, T; Sadowski, MC; Li, HK; Richard, DJ; d'Emden, MC; Richard, K., "Advances in hormonal therapies for hormone naïve and castration-resistant prostate cancers with or without previous chemotherapy"., *Experimental Hematology and Oncology,* 2016, **5,** 15.

Phillips, JC; Braun, R; Wang, W; Gumbart, J; Tajkhorshid, E; Villa, E; Chipot, C; Skeel, RD; Kale, L; Schulten, K., "Scalable Molecular Dynamics with NAMD". *Journal of Computational Chemistry,* **2005,** 26, 1781-1802.

Plotkin, SA., "Vaccines: Past, present and future". *Nature Medicine*, 2005**, 11**, 4, 5-11.

Riss, TL; Moravec, RA; Niles, AL; Benink, HA; Worzella, TJ; Minor, L., "Assay Guidance Manual – Cell Viability Assays"., *editor. Cell Viability Assays*. 2013 May 1. editors. Assay Guidance Manual [Internet]. Bethesda (MD): *Eli Lilly & Company and the National Center for Advancing Translational Sciences*; 2004-. Available from: http://www.ncbi.nlm.nih.gov/books/NBK144065/

Robinson, HL; Pertmer, TM., " DNA vaccines for viral infections: Basic studies and applications"., *Advances in Virus Research,* 2000, **55,** 1-74.

Roch, G.J; Busby, E.R; Sherwood, N.M., "Evolution of GnRH: Diving deeper"., *General and Comparative Endocrinology*, 2011, **171,** 1-16.

Rosa DS; Apostólico, JdS; Boscardin, SB., "DNA Vaccines: How much have we accomplished in the last 25 years?"., *Journal of Vaccines and Vaccination,* 2015, **6,** 283.

Saenz, L; Neira-Carrillo, A; Paredes, R; Cortes, M; Bucarey, S; Arias, JL., "Chitosan formulations improve the immunogenicity of a GnRH-I peptide based vaccine"., *International Journal of Pharmaceutics,* 2009, **369,** 64-71.

Sataki, M; Hayashi, Y; Mido, Y; Iqbal, SA; Sethi, MS., "Colloidal and Surface Chemistry", *Discovery Publishing House,* Published 2003.

Savelkoul, HFJ; Ferro, VA; Strioga, MM; Schijns, VEJC., "Choice and design of adjuvants for parenteral and mucosal vaccines"., *Vaccines,* 2015, **3(1),** 148-171.

Sherwood, NM; Adams, BA., "Gonadotropin-releasing hormone in fish: evolution, expression and regulation of the GnRH gene"., in: Melamed, P; Sherwood, NM

(Eds)., “Hormones and their receptors in fish reproduction”., *World Scientific Publishing Co.,* Singapore, 2005, **1**, 1-39.

Skinner, DC; Malpaux, B; Delaleu, B; Caraty, A., “Luteinizing hormone (LH)-releasing hormone in third ventricular cerebrospinal fluid of the ewe: correlation with LH pulses and the LH surge”., *Endocrinology,* 1995, **136,** 3230-3237.

Skrastina, D; Petrovskis, I; Lieknina, I; Bogans, J; Renhofa, R; Ose, V; Dishlers, A; Dekhtyar, Y; Pumpens, P., “Silica nanoparticles as the adjuvant for the immunisation of mice using hepatitis B core virus-like particles”., *PLoS ONE,* 2014**, 9(12),** e114006.

Sleep, D., “Albumin and its application in drug delivery”., *Expert Opinion on Drug Delivery,* 2014, **12(5),** 793-812.

Spyroulias, GA; Zompra, A; Magafa, V; Cordopatis, P., “1YY1: NMR Conformational Analysis of LHRH and its analogues”, *Worldwide Protein Data Bank,* 2006.

Stewart, AJ; Katz, AA; Millar, RP; Morgan, K., “Retention and silencing of prepro-GnRH-II and type II GnRH receptor genes in mammals”., *Neuroendocrinology,* 2009, **90,** 416-432.

Stöber, Werner; Fink, Arthur; Bohn, Ernst., “Controlled Growth of Monodisperse Silica Spheres in the Micron Size Range”., *Journal of Colloid and Interface Science,* 1968, **26,** 62-69.

Tacket, CO; Losonsky, G; Nataro, JP; Cryz, SJ; Edelman, R; Kaper, JB; Levine, MM., “Onset and duration of protective immunity in challenged volunteers after

vaccination with live oral cholera vaccine CVD 103-HgR". *The Journal of Infectious Diseases,* 1992**, 166**, 837-41.

Talwar, G.P., "Fertility regulating and immunotherapeutic vaccines reaching human trials stage"., *Human Reproduction Update,* 1997, **3**, 301-310.

Temple, JL; Millar, RP; Rissman, EF., "An evolutionary conserved form of gonadotropin-releasing hormone coordinates energy and reproductive behaviour"., *Endocrinology,* 2003, **144,** 13-19.

Toole, MJ., "So close: remaining challenges to eradicating polio". *BMC Medicine,* 2016**, 14:43**, 1-4.

Tsirikis, P, Wilson, K; Kong, Y; Xiang, S; Selomulya, C; Plebanski, M., "Differential antibody induction to surface textured silica nanoparticle adjuvants"., *Journal of Immunology,* 2015, **194,** 1.

Vallhov, H; Gabrielsson, S; Stromme, M; Scheynius, A; Garcia-Bennett, AE., "Mesoporous silica particles induce size dependent effects on human dendritic cells"., *Nano Lett,* 2007**, 7**, 3576-3582.

Voievoda, N; Schulthess, T; Bechinger, B; Seelig, J., "Thermodynamic and biophysical analysis of the membrane association of a histidine-rich peptide with efficient antimicrobial and transfection activities"., *Journal of Physical Chemistry B,* 2015, **119,** 9678-9687.

Wang, T; Jiang, H; Zhao, Q; Wang, S; Zou, M; Cheng, G., "Enhanced mucosal and systemic immune responses obtained by porous silica nanoparticles used as an oral

vaccine adjuvant: effect of silica architecture on immunological properties”., *International Journal of Pharmaceutics,* 2012, **436,** 351-358.

World Health Organization (WHO) (2016). Live Attenuated Vaccines . Retrieved July 14, 2016 from http://vaccine-safety-training.org/live-attenuated-vaccines.html.

Wu, SH; Hung, Y; Mou, CY., “Mesoporous silica nanoparticles as nanocarriers”., *Chem Commun (Cambridge),* 2011, **47,** 9972-9985.

Zhou, B; Li, Y; Speer, SD; Subba, A; Lin, X; Wentworth, DE., “Engineering temperature sensitive live attenuated influenza vaccines from emerging viruses”., *Vaccine,* **30(24),** 3691-3702.

Zhu, M; Wang, R; Nie, G., “Applications of nanomaterials as vaccine adjuvants”., *Human Vaccines & Immunotherapeutics,* 2014, **10 (9),** 2761-2774.

Appendix

RSC Advances

PAPER

View Article Online
View Journal | View Issue

Cite this: RSC Adv., 2016, 6, 73709

Steering protein adsorption at charged surfaces: electric fields and ionic screening†

Paul A. Mulheran,* David J. Connell and Karina Kubiak-Ossowska

Protein adsorption at charged surfaces is a common process in the development of functional technological devices. Accurately reproducing the environment above the surface in simulations is essential for understanding how the adsorption process can be influenced and utilised. Here we present a simulation strategy that includes the electric field above the charged surface as well as the screening ions in solution, using standard molecular dynamics tools. With this approach we investigate the adsorption of Hen Egg White Lysozyme (HEWL) onto a model charged silica surface. We find that the screening effects of the ions slow down the adsorption process, giving the protein more time to find its optimal orientation as it adsorbs. Furthermore, we find that the concentrated ionic region directly above the surface helps to stabilise the protein structure in its adsorbed state. Together these effects imply that the adsorbed HEWL might retain its biological activity, with its active site exposed to solution rather than to the surface. Furthermore, this work shows how the steering effects of the electric field, coupled to the ionic screening, might be used to develop general strategies for surface functionalization through protein adsorption for technological applications.

Received 24th June 2016
Accepted 27th July 2016

DOI: 10.1039/c6ra16391b

www.rsc.org/advances

1 Introduction

Protein adsorption at materials surfaces is a crucial feature of many new biotechnological applications, and has been the focus of much recent research.[1–8] Key questions that still need to be addressed concern not only the extent of protein adsorption, *i.e.* whether complete surface coverage or even multilayer coverage is achieved, but also the strength of the adhesion to the surface and the functionality of the adsorbed protein.[9–14] These factors directly the affect the utility of the adsorbed proteins for functionalization of surfaces to induce biocompatibility, create antibacterial coatings, or yield novel nanoparticulate drug delivery systems.[1]

Modelling has played a major role in advancing our understanding of the adsorption process, since in principle it can reveal molecular-scale insight that is not available experimentally. Well-designed simulations can show not only how proteins adsorb to different surfaces, but also provide understanding of what the driving forces are and how they can be controlled through surface chemistry, and how bio-activity can be preserved by retaining the protein secondary and tertiary structures. There is growing consensus that the orientation of the protein at the surface is paramount, and that this depends on the surface chemistry.[11–13] Of particular note is the idea that electric fields above charged surfaces will play a crucial role in steering the protein during adsorption, and so determine protein orientation once adsorbed.[14–16] Provided that any unfolding induced by interactions with the surface are of limited extent, this provides the means to engineer surface functionalization through controlled protein adsorption.[12]

Fully atomistic Molecular Dynamics (MD) has proven to be a valuable modelling strategy, since it can address the 100 ns timescale necessary for the initial protein adsorption process with the necessary system size of $\sim 10^5$ atoms required to represent the surface, water, ions and protein.[13,16] Various open source simulation packages exist for this type of simulation, where use can be made of potential sets refined for protein systems, and many insightful studies have been completed. Hen Egg White Lysozyme (HEWL) has extensively been used as a model protein,[17–26] since it has anti-bacterial properties which might be preserved when adsorbed to a surface in the correct orientation. HEWL is a hard globular protein of modest size, making it ideal for simulation studies.[27–34] Previous work has considered how it is adsorbed at various surfaces, with the conclusion that negatively charged surfaces, such as mica or silica at physiological conditions, will be best at orienting the protein so that its active site is presented to solution.[27–30]

Given the importance of the electric fields at the charged surfaces, it is necessary to consider how the MD simulations can best replicate the environment experienced by the protein as it adsorbs. In recent work we have included electric fields in standard simulation methodology by employing silica surface models with intrinsic dipole moments.[14,35] However, we had not

Department of Chemical and Process Engineering, University of Strathclyde, James Weir Building, 75 Montrose Street, Glasgow G1 1XJ, UK. E-mail: paul.mulheran@strath.ac.uk

† Electronic supplementary information (ESI) available: The movies showing the trajectories discussed in the manuscript. See DOI: 10.1039/c6ra16391b

until now fully included the effects of ionic screening at the surface. It is the purpose of this paper to do this, and to explore the impact this has on the HEWL adsorption at the model surface. Of crucial importance, we aim to understand whether:

- ionic screening of the charged surface changes the adsorption of the protein or its adsorption pathway;
- the high concentration of ions above a charged surface impacts the structure of the protein in its adsorbed state;
- the electric field and screening effects can be used to enhance our ability to create stable, functional proteins adsorbed to materials with technological potential.

In the following section we will describe how we set up the simulations to capture the effects of electric field and ionic screening, and the simulation methodology we then employ. In Section 3 we present results from our HEWL adsorption simulations, and the discussion will draw out the comparisons to simulations without full ionic screening. In the final section, we will draw general conclusions that are relevant to the modelling of protein adsorption at charged surfaces.

2 Methodology

Oxide surfaces such as silica are known to possess a net negative charge at physiological pH. Whilst the detailed structure at the surface might be difficult to characterise, it is believed that the surface will expose hydroxyl and under-coordinated, terminal oxygen species to the solution,[26] which are responsible for the net negative charge. Simulations of protein adsorption to these surfaces needs to capture not only the chemistry of these species at the surface, but also the long-range electric field they create in the solution above the surface, which as we have discussed above can play a key role in determining protein orientation as it adsorbs. A key challenge for us is to capture these physical effects in our protein adsorption simulations.

The approach we adopt is illustrated in Fig. 1, where we show schematically the electric field surrounding a negatively charged nanoparticle in solution. These nanoparticles are usually ~200 nm size range (*e.g.* silica nanoparticles used for drug delivery[26]), and often much larger than the protein under consideration, so it is reasonable to model adsorption onto a flat surface. This surface needs to expose the relevant species to solution whilst creating the electric field required. In previous work with silica,[13,23] we have employed an alpha-crystabolite {11−1} model employed by other groups.[26] However, we consider a stoichiometric slab of the material which has been cut to create a dipole moment in the direction perpendicular to the largest slab surface, with under-coordinated negatively charged oxygen (siloxide groups) at the top surface and under-coordinated positively charged silicon on the bottom. When used in simulations with three-dimensional periodicity and the Ewald summation for electrostatic calculations, as we do here, this creates the desired electric field across the water space of the simulation cell as illustrated in Fig. 1. We note that using a fixed bounding potential without periodicity in the direction normal to the slab would not create the required electric field. In our simulations, the silica ions are frozen in

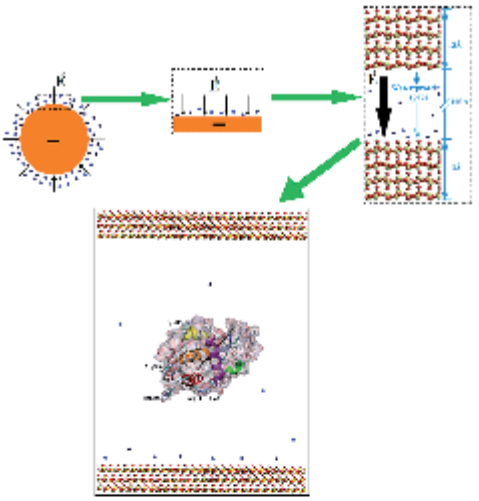

Fig. 1 Illustration of the simulation concept. On the left, a negatively charged nanoparticle in solution has an associated electric field screened by the counter ions of the solution. In the middle, we model a portion of the nanoparticle surface as a flat charged surface with a perpendicular electric field. On the right, we create a suitable electric field in a standard material slab model with periodic boundary conditions. Below, we simulate protein adsorption in this system.

place to maintain the electric field above the surface; using rigid surface model is a common simulation strategy.[27]

This allows us to simulate the adsorption of a protein onto the model negatively charged silica surface. We note that the opposite silicon-rich surface is an artificial construction which does not represent a physically acceptable model surface, so that we are only interested in adsorption to the siloxide-rich surface model. The strength of the electric field is determined by the net dipole moment across the slab and the relative size of the water space to the slab thickness. In the systems used here and in other work, the electric field is measured to be 0.2 V Å^{-1}, which is reasonable given the experimentally observed charge density on large silica nanoparticles at pH 7.[26]

As Fig. 1 also illustrates, in this work we are interested in the effects of ionic screening on the protein adsorption process. When ions are introduced to the simulation cell, the positive ones are drawn to the negative O-rich surface and the negative ones to the Si-rich surface. In the simulations presented here, the slab size (86 Å × 80 Å × 13 Å) is such that 88 ions of each type will perfectly screen the electric field by removing the dipole moment in the system. If fewer ions are used, we will have incomplete screening, and if more are used we will create a bulk ionic environment in the middle of the water space, which is then representative of the environment above the surface in experiments.

In this paper we consider adsorption simulations with N1 = 1, N2 = 49, and N3 = 182 Na^+ ions in the simulation, with the compensating number of Cl^- ions (*e.g.* N1 + 8, *etc.*) and a single

HEWL protein that has charge +8*e* at pH 7. These simulations are labelled SiO_2_N1a, SiO_2_N1b (a separate version with the same number of Na^+ ions), SiO_2_N2 and SiO_2_N3. Full details of our simulation protocol can be found in recent publications.[15,33] In brief, we use NAMD2.6 [38] with periodic boundary conditions, the TIP3P water model, the CHARMM27 force-field with a 12 Å cut-off for short-range potentials and the smooth particle mesh Ewald summation for the electrostatics.[39] Due to the screening effect of the ions, we do not apply any dipole correction to the Ewald summation. There is some debate about the accuracy of CHARMM27 for surface layer effects, however it is a good choice for protein systems.[40]

VMD was employed to analyse results.[41] The HEWL structure was downloaded from 1iee.pdb[42] and the four disulphide bridges were retained. The ions were introduced to the simulation box with a single HEWL followed by the SiO_2 surface and then the water. The system minimisation was performed in two steps: first water and ions only are allowed to move, and then water, ions and the protein can relax. The next step was 30 ps heating of the entire system to the desired 300 K temperature, followed by 270 ps equilibration at constant temperature. Finally the production simulations were performed for 100 ns with a time-step of 1 fs, employing the SHAKE algorithm and periodic boundary conditions. The electrostatic field drove the Na^+ and Cl^- ions towards the negative and positive surfaces during the early stages of the simulations, being apparent during the minimisation period. The ionic screening of the surface was completed within the first few ns of the production trajectories. In the case of the SiO_2_N2 and SiO_2_N3 simulations some ions remained in the bulk water, so that ion exchange was possible.

3 Results and discussion

Adsorption trajectories

In Fig. 2 we show protein structures from HEWL adsorption trajectories with the various ion numbers in the simulations. In each case, the protein starts above the negatively charged siloxide-rich SiO_2 surface with a minimum separation of 28 Å. During the trajectories the protein adsorbs to the surface adopting commonly observed orientations described elsewhere, namely "side on" and "between" which refer to the long-axis orientation of the protein in relation to the surface plane. In low ionic strength systems, SiO_2_N1a and SiO_2_N1b, where there is virtually no screening of the electric field, we have previously reported that the protein adsorbs within ~4 ns.[15] During the first 1 ns of the trajectory, the protein rotates and moves towards the surface. This aligns the HEWL dipole moment and presents the N,C-terminal face to the surface. The first contacts with the surface are usually made by the positively charged residues Arg128 (close to the N-terminus) and Lys1, and subsequently further anchoring interactions with the surface are made by available Arg and Lys residues amongst others.[15] We find two possible adsorption orientations due to the flexibility of the protein surface. However, as we explain below, much of the secondary and all the tertiary structure of the HEWL is preserved in these interactions with the model silica surface, and the active cleft of the enzyme is left exposed to solution.

During the preparation stage (potential energy minimisation, heating and equilibration) of the trajectory SiO_2_N2, the Na^+ ions migrate to towards the model negatively charged silica surface whilst the Cl^- migrate to the image surface, creating ion layers ~6 Å away from the surfaces with thickness ~4 Å. The layers are not very dense and do not greatly disrupt the surface water layers. The protein also translates towards the surface, reducing the Arg128 – surface distance to 17 Å.

During the production trajectory of SiO_2_N2 (see Movie SiO_2_N2.avi), the initial configuration is maintained for ~5.2 ns after which the protein then starts to move towards the surface; the Arg128 and Arg14 side chains are noticeably oriented towards the surface. After a further 0.8 ns (*e.g.* 6 ns of the trajectory) the Arg128 – surface distance reaches the value ~9 Å (*e.g.* top of the ion layer) and it remains here for another 2 ns. At ~8 ns, Arg128 starts to penetrate through the ion layer and at ~8.5 ns reaches the bottom of the ion layer with a distance to the surface of 6 Å. Subsequently, the entire protein is attracted to the surface, and by ~9 ns the protein can be considered to be in its initial adsorption stage. Then, without desorbing, the Arg128 side chain changes its orientation from perpendicular to parallel with respect to the surface plane, and the entire protein moves towards the surface. This movement appears to be easier because the ion layer (and the electric field) is already perturbed. The next residues which almost pass the ion layer, without success, at ~10.4 ns are Lys1 and Glu7. However at ~12.6 ns Arg125 does adsorb with its side chain oriented parallel to the surface. A third anchor adsorption (Arg5) at 18.5 ns does not yet complete the initial adsorption stage; the protein slowly rotates on the surface to facilitate Lys33 and Arg114 adsorption (both at 23.7 ns and with side chains initially perpendicular to the surface). The HEWL reaches its stable adsorption stage at 24 ns. The protein orientation on the surface is "between" (the long protein axis angle is 30° to the surface plane while the dipole moment angle is 60°) and this does not change in the remainder of the trajectory. The only notable events after this time are the side chain reorientations to be parallel with the surface, which are completed by ~97 ns.

During the preparation stage of the highest ionic strength trajectory SiO_2_N3, we again see the creation of the 4 Å thick ionic layers close to the model silica surface and the image. However, as is apparent in Fig. 2, in this case there are also many ions in the bulk water/protein space. This impacts the screening of the electric field, allowing ion exchanges into and out of the ion layers at a rate of ~75 ions per ns in this trajectory. The ion exchanges do not disrupt the surface water layers, but provide fluctuations in the screening of the electric field across the simulation cell.

During the production trajectory (see Movie SiO_2_N3.avi), the protein does not feel the surface at first and so diffuses freely in the bulk, reaching a "side-on" orientation with protein long axis and dipole moment parallel to the surface plane. However, due to the local field fluctuations caused by the ionic motion, at ~7.8 ns the protein moves towards the surface and the minimal distance to the surface starts to fluctuate at ~20 Å.

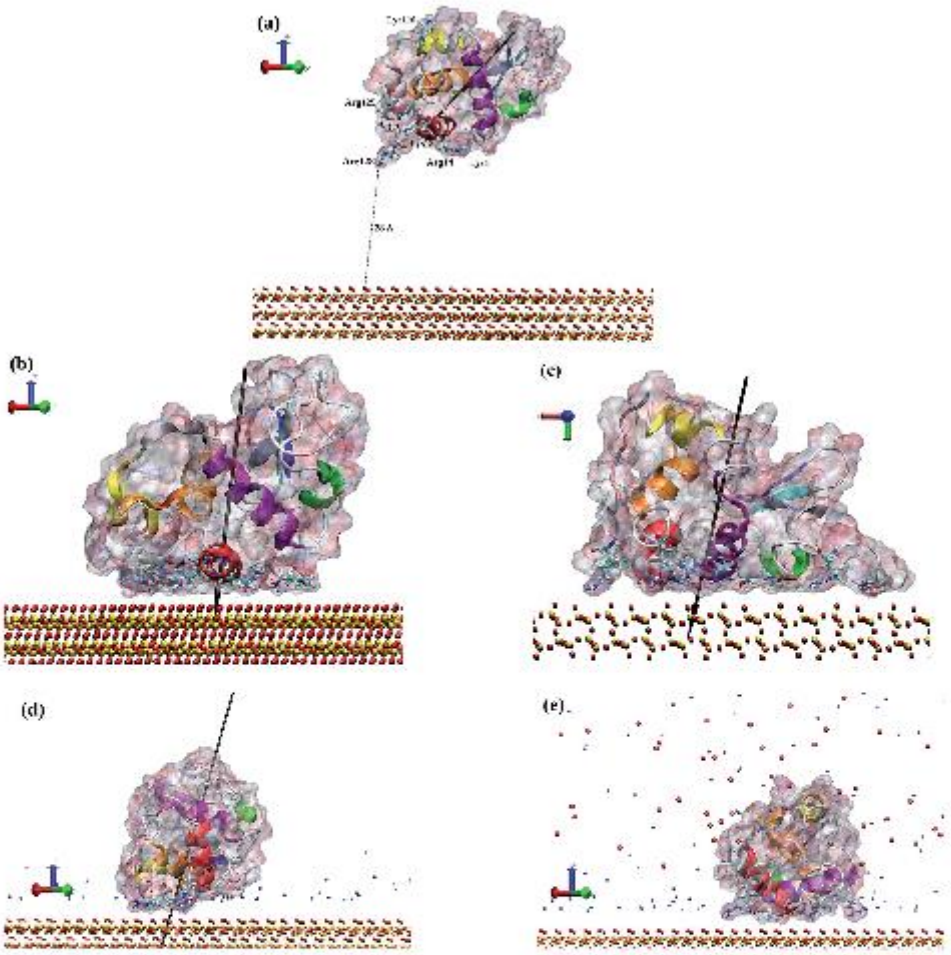

Fig. 2 Adsorption simulations of HEWL onto model silica: (a) starting configuration; (b) "between" without screening ions (SiO_2_N1a); (c) "side-on" without screening ions (SiO_2_N1b); (d) "between" at lower ionic screening (SiO_2_N2); (e) "side-on" at highest ionic screening (SiO_2_N3). The needle in each figure shows the dipole moment of the protein.

From ~14 ns the Arg128 side chain is exposed to the solvent and oriented towards the surface. At ~24 ns the minimal distance between protein and surface is 15 Å and Arg128 clearly starts to act as an anchor, and 2 ns later its side chain reaches the top of the ion layer (distance to the surface 10 Å) for the first time. However, due to its adverse orientation, the electric field repels the protein away from the surface at this stage.

Further local fluctuations again facilitate protein translation and at ~30.9 ns the Arg128 side chain again reaches the top of the ion layer, this time starting to pass through it. Simultaneously the entire protein is attracted to the surface and it also rotates and by 31 ns the dipole moment is directed towards the surface. At ~34.1 ns the Arg128 successfully adsorbs with its side chain perpendicular to the surface. The protein body continues to move closer to the surface and to rotate, resulting in a "side-on" orientation (the long protein axis parallel to the silica surface) by ~70 ns with further residue adsorption completing the adsorption by ~75 ns.

In comparison with the adsorption trajectories SiO_2_N1a and SiO_2_N1b, where adsorption is complete by ~4 ns, we see that the higher ionic concentration slows down the adsorption process without substantially changing the key aspects of the process, namely the preferred orientations of "between" and "side-on" (rather than "end-on") and the key role played by

Arg128 in dictating the adsorption process. In the following we will quantify this slower kinetics whilst considering in more detail the behaviour of the screening ions.

Protein mobility

We monitor the protein mobility on the surface through its centre-of-mass (COM) position over time. Fig. 3 shows the COM motion in the low-screening adsorption trajectories SiO_2_N1a and SiO_2_N1b at the model negatively charged silica surface together with trajectories SiO_2_N2 and SiO_2_N3 in higher ionic strength. In these plots, the red lines indicate the period where the protein moves through the solution without contacting the surface. It is clear that the duration of this motion is extended in higher ionic strength screening, lasting 10–30 times longer than the cases without substantial screening of the surface electric field. This means that the protein diffuses more freely in a bulk-solvent environment in these latter simulations, and the longer adsorption timescale provides more opportunity for the protein to find a favourable orientation as it approaches the surface. Nevertheless, the rotation of the protein in the stronger, unscreened electric fields is rapid enough so that adsorption simulations can still be representative of the adsorption process, provided the protein starts far enough above the surface to allow the rotation to be completed before making contact with the surface.

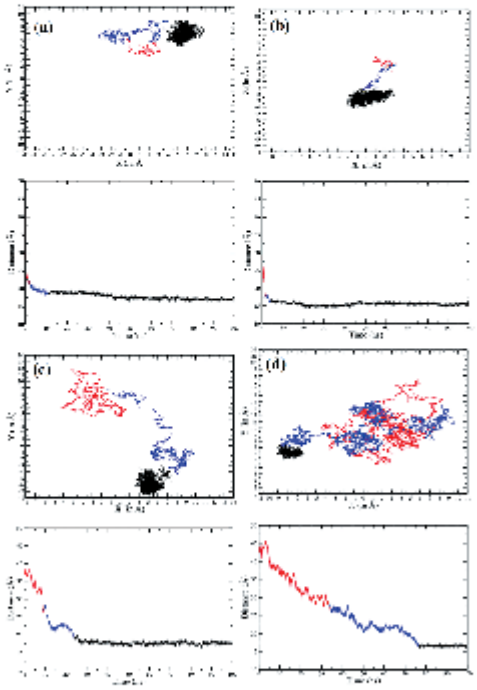

Fig. 3 HEWL centre of mass (COM) diffusion. (a) Low ionicity "between" (SiO_2_N1a) and (b) low ionicity "side-on" (SiO_2_N1b); (c) low (SiO_2_N2) and (d) high ionic screening (SiO_2_N3) adsorption trajectories. The top plots show plan views of the diffusion across the plane of the surface and the bottom plots show changes in time of the COM distance perpendicular to the surface. The red part of the plot indicates diffusion before adsorption (stage 1), the blue part indicates diffusion during the initial adsorption state (stage 2) and the black part indicates the diffusion during the stable adsorption state (stage 3).

The blue sections of the plots in Fig. 3 show the COM motion when residues are interacting with the surface through extended side-chains. In this phase, the COM continues to move towards the model siloxide surface whilst diffusing across the surface; this motion is due (in part) to the flexibility of the extended side-chains of the anchoring residues. Again it is clear that the higher ionic screening extends the duration of this phase of the adsorption, and a wider exploration of the configuration space is achieved.

The final adsorption stage is shown as the black traces in Fig. 3. In all cases, we see that the protein COM becomes well adhered to the surface, maintaining a fairly consistent separation from it ~25 Å due to the protein's size. This shows that the protein retains its hardness, so that whilst structural changes do occur at the interface between the siloxide surface and the protein, these are localised in extent and the adsorbed protein retains most of its secondary and tertiary structure. This will be examined further below. Once the adsorption is complete, we do not observe any long-range diffusion of the protein across the surface in our trajectories; this motion requires much longer timescales due to the size of the energy barriers that need to be overcome for surface diffusion.[22]

Ion concentration fluctuations and the protein response

In Fig. 4 plots of the cumulative number of Na^+ ions (*i.e.* the number within a distance z of the surface) in the higher ionic strength trajectories are shown. Here z is the perpendicular distance above the negative silica surface which is located at $z = 0$. The curves are displayed at different times into the production simulations which started at $t = 0$. The results are taken from the adsorption simulations, and no systematic influence of the protein adsorption on the cumulative ion numbers is apparent. Indeed, as can be seen in the movies, there does not seem to be any synergistic interaction between the protein, the surface and the ions.

The highest ionic strength solution trajectory (SiO_2_N3) results are displayed in the upper plot, which also shows the number of ions (88) for which the electric field due to the charged surface is completely screened. As can be seen, the height above the surface at which complete screening occurs fluctuates between $z \approx 25$ Å and $z \approx 40$ Å, due to the thermal motion of the screening ions. For $z > 40$ Å, the cumulative ion number follows a straight line trend as expected, producing a bulk-solution environment in the middle of the simulation cell with a Na^+ concentration ~0.27 M (note that the Debye screening length for this concentration is ~6 Å). This means that if the protein is greater than ~40 Å above the surface it feels no electric field and, as discussed above, it indeed appears that the HEWL diffuses freely when a long way from the surface.

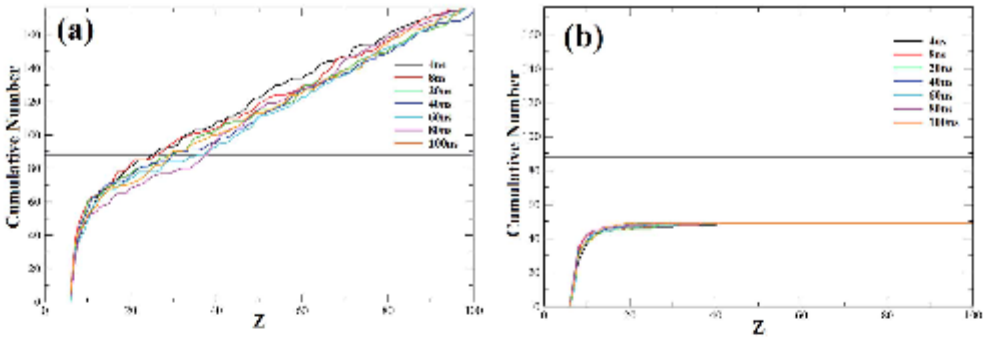

Fig. 4 The cumulative distribution of Na^+ ions above the negative silica surfaces at different times during the trajectories for (a) high (SiO_2_N3) and (b) low (SiO_2_N2) ionic screening.

However, when the protein approaches closer than ~40 Å to the surface, the protein starts to be influenced by the fluctuating electric field. Closer still (z < 25 Å), and the protein feels a consistent electric field and starts to align its dipole with it. An alternative view on the strength of the electric field could be obtained from the electrostatic potential,[25] although again the fluctuating nature of screening is well presented by these cumulative ion distributions.

In contrast, the Na^+ cumulative plots for the lower ionic strength trajectory SiO_2_N2 show that the screening is incomplete and that the electric field felt by the protein is more stable, with a lower degree of fluctuation and a more tightly-bound layer of ions at the surface. This contrast is apparent in Fig. 2d and e, as well as in the movies provided in the ESI.†

In Fig. 5 the z-coordinate of the Arg128 Cz atom is plotted as a function of time for the highest ionic strength trajectory, SiO_2_N3. Contrasting this to the centre-of-mass plot shown in Fig. 3d, we see that the side-chain of Arg128 fluctuates in position a lot more than the protein as a whole. Since the guanidinium end-group is positively charged, it responds to fluctuations in the electric field above the negatively charged silica surface as the screening ion density fluctuates. In the SiO_2_N3 trajectory, the Arg128 side-chain extends from the HEWL surface towards the silica, and then retracts as the screening becomes more efficient and the electric field diminishes. This extension and contraction occurs several times in the trajectory. Once the HEWL is closer to the silica surface and exposed to a more consistent electric field, the Arg128 side chain retains its extended conformation and moves steadily towards the silica surface. In this conformation, it is able to penetrate the water layer above the surface to interact directly with the silica species at ~36 ns. Thereafter, Arg128 retains a strong interaction with the silica, even while the rest of the HEWL rotates to increase the number of contacts, and eventually helps to anchor the protein as described above. This understanding of the crucial role Arg128 plays in the HEWL adsorption process has been described elsewhere,[19,21,22] however we can now add to this picture the role that the electric field fluctuations, caused by the diffusing screening ions, plays in guiding the interactions with the surface and slowing the whole adsorption process.

HEWL structural changes upon adsorption

Structural changes in the adsorption trajectories can be analysed with the RMSD and RMSF plots shown in Fig. 6. The range of conformational changes strongly depends on the trajectory. As Fig. 6a shows, the trajectories with higher ionic strength, and hence partial or complete screening of the surface, show much lower RMSD values than those at low ionic strength. Structural changes in the higher ionic strength trajectories tend to be limited to the loop regions, as shown in the RMSF plots in Fig. 6b. Key secondary structural elements, including the long α-helices A, B, C and D, show much lower levels of fluctuation in their adsorbed state in the higher ionic strength solutions than they do in the absence of the surface screening ions (see previous papers for more discussion of the fluctuation behaviour in these systems[20,22]). This suggests that the ions above the

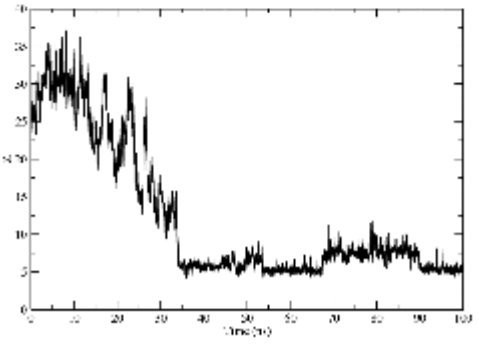

Fig. 5 The z-coordinate in Å of the Arg128 Cz atom as a function of time in the high ionic screening (SiO_2_N3) trajectory.

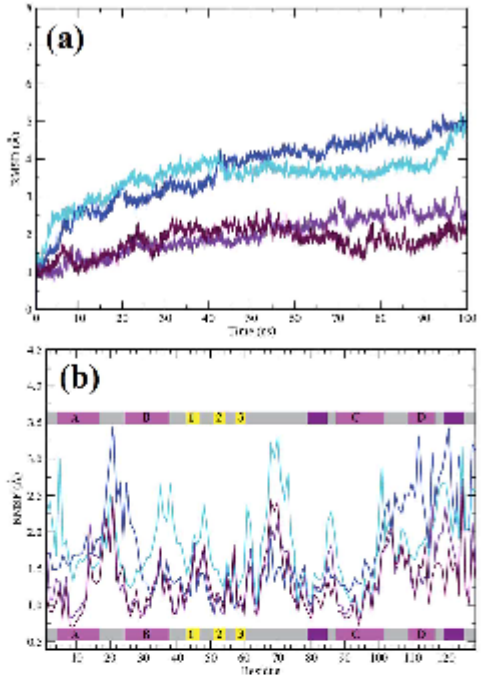

Fig. 6 RMSD (a) and RMSF (b) plots calculated with respect to the initial HEWL structure during trajectories SiO_2_N1a (blue) and SiO_2_N1b (cyan) without screening ions, and SiO_2_N2 (purple) and SiO_2_N3 (brown) with screening ions. The colour ribbon at the RMSF indicates secondary structure in the initial HEWL: loops are shown in grey, β structures in yellow, α-helices in pink and α-helices 3_{10} in purple. For clarity β bridges and turns in loops regions are not shown. The main secondary structure elements are annotated. The preparation period (minimisation, heating and equilibration) is omitted.

charged surface are playing a role in stabilising the adsorbed protein, in the sense of keeping its structural elements intact.[43]

This structural stabilisation indicates that the protein might well retain its biological activity when adsorbed to the surface, the active site is exposed to the solvent, although further work is required to confirm this suggestion. Real surfaces will have screening ions present, so it is certainly worth noting that the adsorption trajectories without substantial ionic screening appear to over-estimate structural changes upon adsorption.

4 Conclusions

We have developed a methodology to include electric fields caused by surface ions, and ionic screening effects above the charged surfaces, in typical protein adsorption simulations. Using the adsorption of HEWL onto a negatively charged model silica surface as an exemplar, we have shown that the screening ions slow down the adsorption process, but fundamentally do not change the broad conclusions we draw from these simulations. The orientation of the adsorbed protein is determined by the alignment of its dipole moment with the electric field above the surface. Provided the protein has adequate time to rotate, the adsorption results in the HEWL orientation previously labelled "side-on" or "between".[13,28,30,31] The screening ions help provide the necessary time for the protein to explore the surface energy landscape, so the adsorption is more controlled. The adsorption process is driven by fluctuations in the electric field above the surface caused by the thermal motion of the screening ions. Furthermore, the ions also help to stabilise the protein once adsorbed, suggesting that the HEWL will retain its biological function with its active cleft exposed to solution and therefore available for interactions with other species.

More broadly, we have shown the importance of correctly including the effects of electric fields and ionic screening to protein adsorption at charged material surfaces. Our methodology can be applied using freely available simulation tools, and is therefore applicable to a range of technologically important systems where bio-compatibility or surface functionalisation is crucial. It is becoming widely accepted that not only protein orientation at the surface, but also the extent to which proteins retain their secondary and tertiary structures,[32] is key to the protein functionality once adsorbed. The steering effects of electric fields,[14–16] coupled with the stabilisation provided by the screening ions,[43] may prove to be crucial aspects in the future development of functional devices.

Acknowledgements

The simulations were performed on the EPSRC funded ARCHIE-WeSt High Performance Computer (http://www.archie-west.ac.uk); EPSRC grant no. EP/K000586/1. DJC was supported by a University of Strathclyde studentship.

Notes and references

1 N. Huebsch and D. Mooney, *Nature*, 2009, **462**, 426–432.
2 W. Norde and A. C. I. Anusiem, *Colloids Surf.*, 1992, **66**, 73–80.
3 M. van der Veen, M. C. Stuart and W. Norde, *Colloids Surf.*, 2007, **54**, 136–142.
4 F. Evers, K. Sholuie, M. Paulus, C. Sternemann, C. Czeslik and M. Tolan, *Langmuir*, 2008, **24**, 10216–10221.
5 K. P. Fears, B. Sivaraman, G. L. Powell, Y. Wu and R. A. Latour, *Langmuir*, 2009, **25**, 9319–9327.
6 H. Hahl, F. Evers, S. Grandthyll, M. Paulus, C. Sternemann, P. Loskill, M. Lessel, A. K. Huseken, T. Brenner, M. Tolan and K. Jacobs, *Langmuir*, 2012, **28**, 7747–7756.
7 B. Jachimska and A. Pajor, *Bioelectrochemistry*, 2012, **87**, 138–146.
8 A. G. Richter and I. Kuzmenko, *Langmuir*, 2013, **29**, 5167–5180.
9 B. Bharti, J. Meissner, S. H. L. Klapp and G. H. Findenegg, *Soft Matter*, 2014, **10**, 718–728.
10 K. Xu, M. M. Ouberai and M. E. Welland, *Biomaterials*, 2013, **34**, 1461–1470.

11 M. Kastantin, B. B. Langdon and D. K. Schwartz, *Adv. Colloid Interface Sci.*, 2014, **207**, 240–252.
12 A. A. Thyparambil, Y. Wei and R. A. Latour, *Biointerphases*, 2015, **10**, 019002.
13 N. Hildebrand, S. Koppen, L. Derr, K. Li, M. Koleini, K. Rezwan and L. C. Ciacchi, *J. Phys. Chem. C*, 2015, **119**, 7295–7307.
14 Y. Xie, C. Liao and J. Zhou, *Biophys. Chem.*, 2013, **179**, 26–34.
15 K. Kubiak-Ossowska, M. Cwieka, A. Kaczynska, B. Jachimska and P. A. Mulheran, *Phys. Chem. Chem. Phys.*, 2015, **17**, 24070–24077.
16 K. Kubiak-Ossowska, P. A. Mulheran and W. Nowak, *J. Phys. Chem. B*, 2014, **118**, 9900–9908.
17 P. A. Mulheran, D. Pellenc, R. A. Bennett, R. J. Green and M. Sperrin, *Phys. Rev. Lett.*, 2008, **100**, 068102.
18 D. Pellenc, R. A. Bennett, R. J. Green, M. Sperrin and P. A. Mulheran, *Langmuir*, 2008, **24**, 9648–9655.
19 T. J. Su, J. R. Lu, R. K. Thomas, Z. F. Cui and J. Penfold, *J. Colloid Interface Sci.*, 1998, **203**, 419–429.
20 S. M. Daly, T. M. Przybycien and R. D. Tilton, *Langmuir*, 2003, **19**, 3848–3857.
21 J. R. Lu, M. J. Swann, L. L. Peel and N. J. Freeman, *Langmuir*, 2004, **20**, 1827–1832.
22 M. van der Veen, W. Norde and M. C. Stuart, *Colloids Surf.*, 2004, **35**, 33–40.
23 S. Z. Qiao, H. Djojoputro, Q. Hu and G. Q. Lu, *Prog. Solid State Chem.*, 2006, **34**, 249–256.
24 S. M. Daly, T. M. Przybycien and R. D. Tilton, *Colloids Surf., B*, 2007, **57**, 81–88.
25 F. Dismer and J. A. Hubbuch, *J. Chromatogr. A*, 2007, **1149**, 312–320.
26 F. Felsovalyi, P. Mangiagalli, Ch. Bureau, S. K. Kumar and S. Banta, *Langmuir*, 2011, **27**, 11873–11882.
27 P. A. Mulheran and K. Kubiak, *Mol. Simul.*, 2009, **35**, 561–566.
28 K. Kubiak and P. A. Mulheran, *J. Phys. Chem. B*, 2009, **113**, 12189–12200.
29 K. Kubiak-Ossowska and P. A. Mulheran, *Langmuir*, 2010, **26**, 7690–7694.
30 K. Kubiak-Ossowska and P. A. Mulheran, *Langmuir*, 2010, **26**, 15954–15965.
31 K. Kubiak-Ossowska and P. A. Mulheran, *J. Phys. Chem. B*, 2011, **115**, 8891–8900.
32 K. Kubiak-Ossowska and P. A. Mulheran, *Langmuir*, 2012, **28**, 15577–15585.
33 A. Steudle and J. Pleiss, *Biophys. J.*, 2011, **100**, 3016–3024.
34 C. Mathe, S. Devineau, J. C. Aude, G. Lagniel, S. Chedin, V. Legros, M. H. Mathon, J. P. Renault, S. Pin, Y. Boulard and J. Labarre, *PLoS One*, 2014, **8**, e81346.
35 K. Kubiak-Ossowska, G. Burley, S. V. Patwardhan and P. A. Mulheran, *J. Phys. Chem. B*, 2013, **117**, 14666–14675.
36 S. V. Patwardhan, F. S. Emami, R. J. Berry, S. E. Jones, R. R. Naik, O. Deschaume, H. Heinz and C. C. Perry, *J. Am. Chem. Soc.*, 2012, **134**, 6244–6256.
37 W. Friedrichs, S. Koppen and W. Langel, *Surf. Sci.*, 2013, **617**, 42–52.
38 J. C. Phillips, R. Braun, W. Wang, J. Gumbart, E. Tajkhorshid, E. Villa, Ch. Chipot, R. D. Skeel, L. Kale and K. Schulten, *J. Comput. Chem.*, 2005, **26**, 1781–1802.
39 U. Essmann, L. Perera, M. L. Berkowitz, T. Darden, H. Lee and L. A. Pederson, *J. Chem. Phys.*, 1995, **103**, 8577–8593.
40 A. A. Skelton, P. Fenter, J. D. Kubicki, D. J. Wesolowski and P. T. Cummings, *J. Phys. Chem. C*, 2011, **115**, 2076–2088.
41 W. Humphrey, A. Dalke and K. Schulten, *J. Mol. Graphics*, 1996, **14**, 33–38.
42 C. Sauter, F. Otalora, J. A. Gavira, O. Vidal, R. Giege and J. M. Garcia-Ruiz, *Acta Crystallogr., Sect. D: Biol. Crystallogr.*, 2001, **57**, 1119–1126.
43 A. S. Parmar and M. Muschol, *Biophys. J.*, 2009, **97**, 590–598.